On numerical solutions of topology optimization problems

Andrés Felipe Ortegon Villacorte

Universidad Nacional de Colombia
Facultad de Ciencias, Departamento de Matemáticas
Bogotá, Colombia
2023

On numerical solutions of topology optimization problems

Andrés Felipe Ortegon Villacorte

Tesis o trabajo de grado presentado como requisito parcial para optar al título de:
Magister en Matematica Aplicada

Directores:
PhD. Juan Galvis, PhD. Julián Norato

Línea de investigación:
Optimización Topológica
Universidad Nacional de Colombia
Facultad de Ciencias, Departamento de Matemáticas
Bogotá, Colombia
2023

Agradecimientos

Agradezco al profesor Juan Galvis por el acompañamiento durante todo el programa de maestria y el conocimiento compartido. También al profesor Julian Norato por sus comentarios y correcciones durante la investigación. A mi familia por su apoyo continuo durante todas las etapas de mis estudios.

Resumen

Sobre soluciones numéricas a problemas de optimización topológica

Este trabajo de investigación estudia las técnicas de optimización topológica aplicadas al problema clásico del calor y al problema de la elasticidad. El estudio destaca varios aspectos clave encontrados durante el proceso de búsqueda de soluciones para problemas específicos, incluida la influencia de las condiciones iniciales y los parámetros del optimizador. Además, el documento explora enfoques novedosos y variaciones de métodos fundamentales encaminados a lograr soluciones finales mejoradas para cada problema. Estas adaptaciones abarcan ajustes del funcional minimizado, la representación del espacio de densidad y la aplicación de métodos de regularización.

Palabras clave: Optimización Topológica, Optimización Estructural, Ecuaciones Diferenciales Parciales, Elementos Finitos, Análisis Numérico, Regularización.

Abstract

On numerical solutions of topology optimization problems

This work studies topological optimization techniques applied to the classical heat problem and the elasticity problem. The study highlights various key aspects encountered during the solution search process for specific problems, including the influence of initial conditions and optimizer parameters. Moreover, the paper explores novel approaches and variations of fundamental methods aimed at achieving improved final solutions for each problem. These adaptations encompass adjustments to the minimized functional, the representation of density space, and the application of regularization methods.

Palabras clave: Topology Optimization, Structural Optimization, Partial Diferential Equations, Finite Elements, Numerical Analysis, Regularization.

Contents

List of Figures

List of Tables

1 Introduction

Modern industry makes it possible to find a wide variety of solutions to engineering problems using a variety of manufacturing processes and design techniques. Given certain criteria and defined constraints, we can search for the optimal solution among these solutions. To obtain such a solution, numerous approaches have been developed. Among them, we find the framework of topology optimization, which approximates an optimal distribution of material in the domain satisfying the physical requirements, see [Bendsøe and Sigmund, 2004]. This area of development and research is mature in problems of stress and deformation of solids, thermal conductivity and cooling of systems, fluid dynamics, electrodynamics, and multiphase interactions, among others [Deaton and Grandhi, 2014]. An optimal solution can improve material usage, system performance, usability, and manufacturability. The influence of optimization on physical problems can be seen in many industries such as transportation, construction, manufacturing, and many others. See for example [Cavazzuti et al., 2011, Matsimbi et al., 2021, Beghini et al., 2014, Donofrio, 2016, Zhu et al., 2016, Orme et al., 2017].

There are families of methods in topology optimization, for example, there are evolutionary methods that optimize on a discrete but extremely large feasible set of possible designs. Others use a relaxation of the problem to implement a search in a continuous set of finite dimension. In between we find the density method with numerous variations and three-phase methods that implement a third field to improve the convergence to 0-1 designs, see [Sigmund and Maute, 2013]. The relaxation methods use efficient and robust optimization techniques to deliver the design found in a reasonable time and with sufficient accuracy or performance gain, see for example [Sigmund and Maute, 2013]. However, the problem is complex, even when relaxed, and additional corrections and post-processing may be required to produce a practical design. Also, it is very common to find numerous solutions within small variations (or perturbations) in the parameters of the simulation. Therefore, designers often implement a sub-optimal design or use the best optimum to inspire a solution rather than looking for a global optimum [Sigmund and Maute, 2013, Beghini et al., 2014, Papadopoulos et al., 2021].

In the geometry projection method studied in this work, which is based on the method of densities, see [Smith and Norato, 2020], the issues caused by the numerous local minima and non-convexity of the performance functional are still present in a way to be explored in Chapter 5. As the description of material is based on a fewer number of variables the number of local minima is reduced but, the solutions found have overall a poorer performance

than the minima in the method of the densities, see [Wein et al., 2020]. The motivation for this work comes from the interest in improving the performance of the minima found by the optimizer. We have decided to review and explore several aspects related to numerical local solutions of topology optimization problems in the general density formulation and GPTO. The objective of this thesis is to examine issues related to the appearance of different locally optimal solutions depending on different conditions in the process, such as relaxation approach, initial guess, computational mesh, and accuracy of linear solvers, among others.

The rest of the manuscript is organized as follows. In Chapter 2 we present the theory for the numerical approximation of the physical problems we deal with in this thesis. In Chapter 3 we present two topology optimization frameworks, the classical method of densities and the geometry projection method. In Chapter 4 we present the optimization strategy used to solve the problem and we analyze the results of numerical simulations, with different modifications to the method. In Chapter 5 we test some regularization methods to further improve solutions to TO problems.

2 Theoretical background

Our study of topology optimization begins with the presentation of the tools for representing certain physical phenomena. This chapter examines the systems of partial differential equations (PDEs) that model such phenomena, and the numerical methods that approximate the solutions to these equations

2.1 Physical models

This section describes the systems of equations for the heat transfer problem and the linear elasticity problem. Excerpts from [Gockenbach, 2006, Yan et al., 2018, Andreassen et al., 2010, Gelfand and Fomin, 2012] are used to explain the background theory used in this work.

2.1.1 Heat transfer

A simple problem we can study in topology optimization consists of the evacuation of heat outside a domain, see [Bendsøe and Sigmund, 2004]. To pose this problem we assume there is a material capable of transporting heat by *conduction* in a domain Ω with two or three dimensions. Fourier's law tells us that the heat flux is proportional to the temperature gradient. In a two-dimensional domain, we can understand this problem as a thin plate of conductive material where the out-of-plane direction has no heat transfer. Assuming initially that we have a homogeneous isotropic material in the plate, the equation reads

$$\theta\,\Delta u(x) + f(x) = 0\,. \tag{2-1}$$

We call this equation the *stationary diffusion equation* or *Poisson equation*. Here $\theta > 0$ is a proportionality constant of Fourier's law called *thermal conductivity*, u is the value of the temperature at the point x, $f(x)$ is a rate at which heat is added to the domain and Δ is the *Laplace* operator applied to u and defined as

$$\Delta u(x) = \frac{\partial^2 u}{\partial x^2} + \frac{\partial^2 u}{\partial y^2}.$$

If the thermal conductivity is not constant in the domain, that is, the material is not homogeneous, then the model is better described by the equation

$$\nabla \cdot (\theta(x)\,\nabla u(x)) + f(x) = 0\,. \tag{2-2}$$

Here, the dependence of θ on the position in the domain becomes explicit. Finally, if the material is not isotropic, the thermal conductivity depends on the direction and instead of a constant θ it is better to introduce a material conductivity tensor $\boldsymbol{\Theta}(x, y)$. We have

$$\nabla \cdot (\boldsymbol{\Theta}(x)\, \nabla u) + f(x) = 0 \,. \tag{2-3}$$

The tensor $\boldsymbol{\Theta}(x)$ can be represented by the parameters $\lambda_1(x)$ and $\lambda_2(x)$ calculated as

$$\boldsymbol{\Theta}(x) = \sum_{i=1}^{d} \lambda_i(x)\, \mathbf{e}_i \mathbf{e}_i^T \,.$$

Here $\mathbf{e}_i$ represents the principal directions of conductivity and d the number of dimensions. It can be seen that (2-1) and (2-2) are particular cases of (2-3). The heat generation rate $f(x)$ is treated in this work as independent of the material properties. In order to have a well-posed problem, equation (2-3) must be supplemented with boundary conditions (BC). The BC describes a piece of known information in the boundary $\partial\Omega$ of the domain Ω. In this work, we deal only Dirichlet BC in a subset $\Gamma_1 \subseteq \partial\Omega$ and Neumann BC in a subset $\Gamma_2 \subseteq \partial\Omega$. These two subsets of the boundary must satisfy

$$\Gamma_1 \cup \Gamma_2 = \partial\Omega,$$
$$\Gamma_1 \cap \Gamma_2 = \emptyset.$$

The Dirichlet BC are described by the equation

$$u(x) = g(x) \,, \qquad \text{for all } x \text{ in } \Gamma_1 \,. \tag{2-4}$$

Here $g(x)$ is a function that determines the value of the temperature in the boundary. For instance, if the value of the temperature in Γ_1 is always lower than the temperature inside the domain, we can interpret the Dirichlet boundary as a *heat sink*, if it has a higher temperature then it can be understood as a *heat source*. The Neumann BC is described by

$$(\boldsymbol{\Theta}(x)\, \nabla u(x)) \cdot \mathbf{n} = h(x) \,, \qquad \text{for all } x \text{ in } \Gamma_2 \,. \tag{2-5}$$

The function $h(x)$ sets the heat flux, the rate at which heat is evacuated, through the boundary Γ_2 outside the domain. For instance, if $h(x) = 0$ the boundary does not transfer heat outside the domain. This is known in the context of heat transfer as *adiabatic conditions*. In a more general context, the boundary conditions $h(x) = 0$ are called *natural conditions*, as they appear naturally in the integration by parts when deriving the weak or variational of the equation. In this work, we assume natural boundary conditions always that a Dirichlet BC is not specified. The problem of finding a solution to a PDE with boundary conditions is called a *boundary value problem* (BVP). The BVP for the heat equation treated in this work is given below.

Problem 1 *Find $u(x)$ such that*

$$\begin{aligned} &\nabla \cdot (\boldsymbol{\Theta}(x)\, \nabla u(x)) + f(x) = 0 \,, \\ &u(x) = g(x) \,, && \text{for all } x \text{ in } \Gamma_1 \,, \\ &(\boldsymbol{\Theta}(x)\, \nabla u(x)) \cdot \mathbf{n} = 0 \,, && \text{for all } x \text{ in } \Gamma_2 \,. \end{aligned}$$

In topology optimization, as will be seen in Chapter 3, we are interested in filling Ω with a certain amount of conductive material and leaving the rest of the domain without material. This distribution is understood as a domain with two materials with different thermal conductivity as described by (2-2), for example

$$\boldsymbol{\Theta}(x) = \begin{cases} 1, & \text{In the domain with material} \\ \varepsilon, & \text{In the domain with no material} \end{cases}$$

Ideally, $\varepsilon = 0$, however, this would lead to non-uniqueness of the solution of the BVP, see [Bendsøe and Sigmund, 2004]. Therefore, to ensure a unique solution it is customary in the method of densities described in Chapter 3 to choose $0 < \varepsilon << 1$.

2.1.2 The linear elasticity equations

The linear elasticity problem is probably the best-known application of the topology optimization framework, see [Bendsøe and Sigmund, 2004]. Although it shares similarities with the heat equation presented earlier, the system of PDEs governing the relations of an isotropic linearly elastic material are vector equations, since the deformation $\mathbf{u}$ is a vector quantity. This is the system of PDEs

$$-\nabla \cdot \sigma = \mathbf{f} \,, \tag{2-6}$$

$$\sigma = \lambda \operatorname{tr}(\nabla_s \mathbf{u})\, I + 2\mu\, \nabla_s \mathbf{u} \quad \text{and} \tag{2-7}$$

$$\nabla_s \mathbf{u} = \frac{1}{2}(\nabla \mathbf{u} + \nabla \mathbf{u}^T) \,. \tag{2-8}$$

Here σ is the stress, $\mathbf{f}$ represents a body force per unit of area or volume depending on the dimensions of the problem, λ and μ are the Lamé parameters and I is the identity matrix of appropriate dimension. For an isotropic material in a bidimensional domain, this system is equivalent to a pair of second-order equations. However, this form of representation is more convenient as it makes explicit the balance equation (2-6), which indicates that the divergence of the stress tensor σ is in static equilibrium with the external forces $\mathbf{f}$ (forces on the boundary), and the constitutive equation (2-7), which is an assumption related to the behavior of the material. Equation (2-8) helps simplify the notation of the constitutive equation and can be understood as the symmetric part of the gradient of the displacement $\nabla \mathbf{u}(x)$. The boundary conditions, can be Dirichlet conditions:

$$\mathbf{u}(x) = \mathbf{g}(x) \,, \qquad \text{for all } x \text{ in } \Gamma_1 \,. \tag{2-9}$$

As in the previous section, this equation indicates that the field has a determined value in the boundary, that is, the deformation has a specific value in the subset Γ_1. Similarly,

$$\sigma(x) = \mathbf{h}(x) \,, \qquad \text{for all } x \text{ in } \Gamma_2 \,. \tag{2-10}$$

The function $\mathbf{h}$ represents traction applied in the boundary subset Γ_2 of the domain. In this work, we assume that there is no traction on the boundary, as we did with the heat flux in the boundary in the heat equation BVP.

2.1.3 Weak form of the equations

In Problem 1, if $f \in C^k(\Omega)$, then a solution u would have two orders of regularity more than f, that is, $u(x) \in C^{k+2}(\Omega)$. More generally, a function $u(x) \in C^{k+2}(\Omega) \cap C^k(\bar{\Omega})$ satisfying the BVP 1 is called a *classical solution*. In the finite element method, we are interested in weakening this requirement to approximate our solution using a space with minimal smoothness. To do this we can use the fundamental lemma of the calculus of variations, [Gelfand and Fomin, 2012].

Lemma 1 *If $\beta(x)$ is a function which is continuous in a closed domain Ω, the integral*

$$\int_\Omega \beta(x) v(x) d\Omega \tag{2-11}$$

vanishes for every function $v \in C^2(\Omega)$ and β equals 0 in the boundary $\partial\Omega$, then $\beta(x) = 0$, for all $x \in \Omega$.

A function v is called a test function and to highlight the vanishing value in the boundary the vector space to which v belongs is usually written as

$$C_0^2(\Omega) = \{v : \Omega \mapsto \mathbb{R} : v|_{\Gamma_1} = 0\} \,. \tag{2-12}$$

In problem (1) we multiply and integrate to obtain

$$\int_\Omega \left(\nabla \cdot (\mathbf{\Theta}(x)\, \nabla u(x)) + f(x)\right) v(x) = 0 \,, \qquad v \in C_0^2(\Omega) \,. \tag{2-13}$$

Here the Green identity is applied

$$\int_\Omega \mathbf{\Theta}(x)\, \nabla u(x) \nabla v(x) = \int_\Omega f(x) v(x) + \int_{\Gamma_2} h(x) v(x) \,, \qquad v(x) \in C_0^1(\Omega) \,. \tag{2-14}$$

The boundary term due to the Green identity on the right-hand side of the equation cancels out since there are natural boundary conditions ($h(x) = 0$ in Γ_1). A similar deduction allows us to obtain the weak form (2-15) for the elasticity problem in Equations (2-6) and (2-7). See [Gockenbach, 2006] for details.

$$\int_\Omega 2\mu\, \nabla_s u(x) \nabla_v(x) + \lambda \mathrm{tr}\left(\nabla_s u(x)\right) \mathrm{tr}\left(\nabla_s v(x)\right) = \int_\Omega f(x) v(x) + \int_{\Gamma_2} h(x) v(x) \,, \qquad v(x) \in C_0^1(\Omega) \,. \tag{2-15}$$

We can see that the regularity of the space in this *weak form* is lower, then we could obtain a solution to the original problem in a space with fewer derivatives, more on this in the next section.

2.1.4 Existence of solutions

The space of representation of solutions to the previous weak problem lacks completeness. See [Kreyszig, 2007].

Definition 1 *Let $\{v_n\}$ be a sequence of vectors in a normed space H. The sequence is called Cauchy if given any $\varepsilon > 0$ there exists a positive integer N such that*

$$n, m > N\,, \ \textit{implies} \qquad \|v_m - v_n\|_H < \varepsilon\,. \tag{2-16}$$

Here $\|\cdot\|_H$ is the norm of the space. The space H is said to be complete if every Cauchy sequence in H converges to an element in H.

For example, to complete the space $C(\Omega)$ we need to define a norm and find a closure in it [Kreyszig, 2007]. This can be accomplished for instance in the following way.

Definition 2 *A function v is said to be square-integrable on an open bounded domain Ω if*

$$\int_\Omega |v|^2 < \infty\,. \tag{2-17}$$

That is, the value of the integral over the domain has a finite value for every element v. The set of all functions satisfying the previous inequality forms a complete vector space

$$\mathcal{L}_2 = \mathcal{L}_2(\Omega) = \left\{ v : \int_\Omega |v|^2 < \infty \right\}\,, \tag{2-18}$$

with norm

$$\|v\|^2_{\mathcal{L}_2} = \int_\Omega |v|^2\,. \tag{2-19}$$

We can extend this space $\mathcal{L}_2(\Omega)$ by including a similar bound for the derivative of the functions in a space of higher regularity. To accomplish this we need integrable derivatives, then we define the weak derivative.

Definition 3 *A function $g \in \mathcal{L}_2(\Omega)$ is called the weak partial derivative of $u \in \mathcal{L}_2(\Omega)$ with respect to the variable x_i, a component of $x \in \Omega$, if the following equation holds*

$$\int_\Omega u \frac{\partial v}{\partial x_i} = \int_\Omega g v\,, \qquad \textit{for all } v \in C_0^\infty(\Omega)\,. \tag{2-20}$$

Functions with integrable weak derivatives are differentiable in almost every point of their domain, except for a set of null size, see [Johnson, 2012]. We can now define also a special Hilbert space with a higher degree of smoothness. Define

$$\begin{aligned} \mathcal{H}^1(\Omega) &= \left\{ u \in \mathcal{L}_2, \frac{\partial u}{\partial x_i} \in \mathcal{L}_2, i = 1, ..., n \right\} \text{ , with norm} \\ \|u\|^2_{\mathcal{H}^1} &= \|u\|^2_{\mathcal{L}_2} + \sum_i \left\| \frac{\partial u}{\partial x_i} \right\|^2_{\mathcal{L}_2} , \qquad i = 1, ..., n \, . \end{aligned} \tag{2-21}$$

This new space is appropriate to find solutions to Problem 1 thanks to the regularity and the properties obtained by adding a norm to the space. We can now define the following mappings.

Definition 4 *A linear form in the Hilbert space $\mathcal{H}^1(\Omega)$ is a mapping $L : \mathcal{H}^1(\Omega) \to \mathbb{R}$. The linear form of the problem* (2-14) *is the right-hand side (RHS) of the equation, that is,*

$$L(v) = \int_\Omega f v \, , \qquad \text{for all } v \in \mathcal{H}^1(\Omega) \, .$$

Similarly, a bilinear form is a mapping $a : \mathcal{H}^1(\Omega) \times \mathcal{H}^1(\Omega) \to \mathbb{R}$ and in the case mentioned before is the left-hand side (LHS), that is,

$$a(u, v) = \int_\Omega \mathbf{\Theta}(x, y) \, \nabla u \nabla v \, , \qquad \text{for all } u \in \mathcal{H}^1(\Omega) \text{ and } v \in \mathcal{H}^1_0(\Omega) \, .$$

We can write then Problem (2-14) as

$$a(u, v) = L(v) \, , \quad \text{for all } v \in \mathcal{H} \, . \tag{2-22}$$

To guarantee the existence and uniqueness of the solution to Problem 1 we use the Lax-Milgram theorem, see [Gockenbach, 2006].

Theorem 1 *Let H be a Hilbert space with inner product $(\cdot, \cdot)$ and norm $||\cdot||$. Let $a(u, v)$ be a bilinear form in H. If*

- *a is continuous, that is, exists a constant M such that*

$$|a(u, v)| \leq M \|u\| \|v\|, \qquad \text{for all } u, v \in H \, .$$

- *a is coercive. This is, exists a constant $\alpha > 0$ such that*

$$\alpha \|u\|^2 \leq a(u, u), \qquad \text{for all } u \in H \, .$$

Then there exists a unique solution $\bar{u} \in H$ for the equation (2-22).

In this work $V = H^1(\Omega)$. The following Lemma derived from the Lax-Milgram theorem give us the properties of matrix $\mathbf{\Theta}$ to satisfy the theorem, see [Marheineke, 2020].

Lemma 2 *Let $\mathbf{\Theta}(x) = a_{ij}(x)$ a symmetric, bounded, positive definite matrix such that there exists α*

$$\alpha\|\zeta\|^2 \leq \zeta^T \mathbf{\Theta}(\mathbf{x})\zeta \,, \qquad \textit{for all } \zeta \in \mathbb{R}^d \,.$$

Then the bilinear form $a : \mathcal{H}^1 \times \mathcal{H}^1 \to \mathbb{R}$ given by

$$\int_\Omega \mathbf{\Theta}(x)\nabla u(x)\nabla(v)$$

is symmetric, continuous and coercive.

2.2 The finite element method

The finite element method is a strategy for numerical approximation of solutions to partial differential equations. Here we explain the most common form of the method, the Galerkin method. See [Gockenbach, 2006].

2.2.1 Galerkin method and discretization

We look for an approximation of the solution u. This approximation will be represented in a subspace H_h of (finite dimension $dim(H_h) = n < \infty$) of the Hilbert space H of infinite dimension. In this subspace, the bilinear form and the linear form are still defined. We use the same subspace for the approximate solution and the test functions in the Galerkin method. Equation (2-22) becomes

$$a(u_h, v_h) = L(v_h) \,, \qquad \text{for all } u_h, v_h \in H_h \subset H \,. \tag{2-23}$$

As this new subspace H_h has finite dimension, then we can find a basis of H_h, say

$$\Phi = \{\phi_1, \phi_2, ..., \phi_n\} \,.$$

And we can represent our solution as a linear combination of this basis with coefficients u_i. That is,

$$u_h = \sum_i u_j \phi_j \,. \tag{2-24}$$

In the same way, each test function ϕ_i can be taken to be one function of the chosen basis for H_h. Replacing in equation (2-25) and then using the linearity of $a(u, v)$ we get

$$\begin{aligned} a\left(\sum_j u_j\phi_j, \phi_i\right) &= L(\phi_i) \,, \qquad i = 1, ..., n \,. \\ \sum_j u_j a\left(\phi_j, \phi_i\right) &= L(\phi_i) \,, \qquad i = 1, ..., n \,. \end{aligned} \tag{2-25}$$

This is a system of linear equations $\mathbf{Au} = \mathbf{f}$ with

$$\begin{aligned} \mathbf{A} &= a_{ij} = a\left(\phi_j, \phi_i\right) , \\ \mathbf{u} &= u_j , \\ \mathbf{f} &= f_i = L\left(\phi_i\right) . \end{aligned}$$

Here we use the notation a for the bilinear form and $\mathbf{A}$ for the *stiffness matrix*. However, it is common in topology optimization to note the matrix with the letter $\mathbf{K}$. The approximation u_h is the best approximation to the solution u in the subspace $H_h \subseteq H$. For this, we have the lemma of Ceà, see [Johnson, 2012].

Lemma 3 *Let a be a bilinear form in the Hilbert space H with continuity constant M and coercivity constant α. The solutions u to the equation* (2-22) *and u_h to the equation* (2-25) *satisfy*

$$\|u - u_h\|_H \leq \frac{M}{\alpha} \inf_{v_h \in H_h} \|u - v_h\| . \tag{2-26}$$

In this work, the Hilbert space H is the space $\mathcal{H}^1(\Omega)$ mentioned in the previous section. Basis functions ϕ_i can be chosen to have compact support, then before choosing such functions, we divide the domain Ω into a finite set of subdomains. This partition of the domain can be denoted $\mathcal{K}$. Each element Ω_e of this partition is called a finite element (FE) and the collection of elements is called a *mesh*. In this partition, we select our basis functions, for example of polynomial form.

The FE can be as complex as desired, but they are usually chosen as simple polygonal subdomains to simplify the basis functions and the quadrature used to compute the required integrals. The most commonly used discretization is made of triangles. In topology optimization, any mesh can be used, but to keep the code simple and use little memory, it is common to use elements of the same shape, for example, use squared elements of the same size, see [Andreassen et al., 2010] In this work, we follow this approach.

2.2.2 Finite element spaces used in this work

We use square elements in our partition and we also restrict ourselves to rectangular domains. These conditions ensure that in general, the mesh is *conforming*, see [Gockenbach, 2006]. We define additionally a constant h as the *element width*. An example of a mesh with square elements is presented in Figure **2-1**. In this figure, we can see that we use two different enumerations, both useful in this work. In Figure **2-1**a, the first coordinate increases downwards and the second coordinate increases to the right. The second enumeration of nodes in **2-1**b has an index that increases downwards and then continues up on the next column to the right.

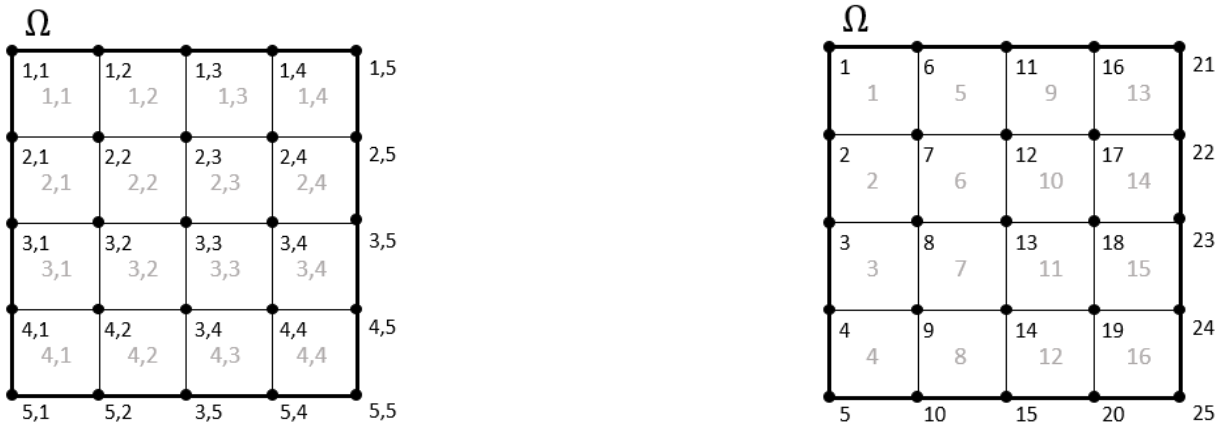

(a) Double index i, j (b) Single index k

Figure 2-1: Example of a mesh with squared elements. The mesh has a size of 4×4 elements and we represent two different enumerations of the nodes and the elements

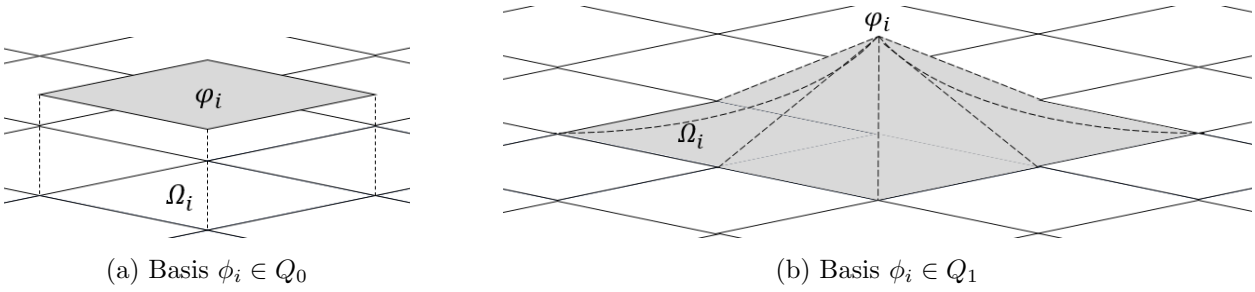

(a) Basis $\phi_i \in Q_0$ (b) Basis $\phi_i \in Q_1$

Figure 2-2: Basis functions for the Q_0 and Q_1 spaces.

In this document, we work mainly with Q_0 (Figure **2-2**a) and Q_1 (Figure **2-2**b) finite elements. The Q_0 elements represent a discontinuous function that in each subdomain is constant. The weak formulation would allow us to work with this type of element depending on the discretization. However, our interest in this sort of element is only to represent the distribution of the material in each subdomain and not the physical field. Define

$$Q_0 = \{\phi_i : \phi_i|_{\Omega_i} \in P_0\} \ . \tag{2-27}$$

Here P_0 represent the space of polynomials of degree 0 or constant functions. The space Q_1 is more suitable to work if we want to solve a system of PDE using a Galerkin (conforming) approximation. With this type of element, we represent *bilinear* functions in each element. Polynomials of the form

$$p(x) = (\gamma_0 + \gamma_1 x_1)(\delta_0 + \delta_1 x_2) = a_0 + a_1 x_1 + a_2 x_2 + a_3 x_1 x_2 \ .$$

In this representation, the value of the approximation $u_h = \sum_j u_j \phi_j$ in the nodes of the mesh is defined by the nodal value $u_j = u_h(x_j)$. For example, consider the nodes $x_{i,j}$, $x_{i+1,j}$,

$x_{i,j+1}$ and $x_{i+1,j+1}$, then there is a unique polynomial $p(x)$ satisfying

$$\begin{aligned} u_{i,j} &= a_0 + a_1 x_{i,j}^{(1)} + a_2 x_{i,j}^{(2)} + a_3 x_{i,j}^{(1)} x_{i,j}^{(2)} \,, \\ u_{i+1,j} &= a_0 + a_1 x_{i+1,j}^{(1)} + a_2 x_{i+1,j}^{(2)} + a_3 x_{i+1,j}^{(1)} x_{i+1,j}^{(2)} \,, \\ u_{i,j+1} &= a_0 + a_1 x_{i,j+1}^{(1)} + a_2 x_{i,j+1}^{(2)} + a_3 x_{i,j+1}^{(1)} x_{i,j+1}^{(2)} \,, \\ u_{i+1,j+1} &= a_0 + a_1 x_{i+1,j+1}^{(1)} + a_2 x_{i+1,j+1}^{(2)} + a_3 x_{i+1,j+1}^{(1)} x_{i+1,j+1}^{(2)} \,. \end{aligned}$$

An additional property of this representation is that for each rectangle, the function is linear on the edges. Finally, we define the following space

$$Q_1 = \left\{ \phi_i \in C^0(\Omega) : \phi_i|_{\Omega_e} \text{ is a degree-one polynomial} \right\} \,. \tag{2-28}$$

When we compute the stiffness matrix for the studied field, temperature or deformation, we combine the representation of the material with the basis functions of the main field. For example, we consider the set of equations for the heat problem

$$\mathbf{K}_i \mathbf{u} = \int_\Omega \mathbf{\Theta}(x) \nabla \mathbf{u} \nabla \phi_i = \sum_j u_j \int_\Omega \mathbf{\Theta}(x) \nabla \phi_j \nabla \phi_i \,, \qquad i = 1, 2, ..., N \,.$$

Here the thermal conductivity $\mathbf{\Theta}(x)$ depends on the position in the mesh and $\mathbf{K_i}$ is the i-th row of the stiffness matrix $\mathbf{K}$. If the thermal conductivity is represented by a linear combination of a set of basis functions

$$\mathbf{\Theta}(x) \approx \sum_k \theta_k \psi_k \,, \qquad \psi_k \in Q_0 \text{ or } Q_1$$

Then we compute the i, j term of the global rigidity matrix as the integral over the intersection of supports $\text{supp}(\phi_i) \cap \text{supp}(\phi_j)$

$$\mathbf{K}_{i,j} = \int_\Omega \sum_k \theta_k \psi_k \nabla \phi_j \nabla \phi_i \,, \qquad i, j = 1, 2, ..., N \,. \tag{2-29}$$

Here the sum k is in the elements such that $x_k \in \text{supp}(\phi_i) \cap \text{supp}(\phi_j)$.

Material properties represented by the Q_0 space

Consider the specific case when the meshes for the material properties and main field match and $\psi \in Q_0$. Each basis function $\phi_h \in Q_1$ is composed of 4 bilinear segments in different elements Ω_e sharing the node i. Similarly, there are 4 different test and trial basis functions acting in a single element Ω_e with a single quadrature point of material, then we compute a stiffness matrix for a single element in the following way

$$\mathbf{K}_e = \theta_e \int_{\Omega_e} \nabla \phi_j \nabla \phi_i \,, \qquad i, j \text{ such that } x_i, x_j \in \Omega_e \,. \tag{2-30}$$

Here $\mathbf{K}_e$ is the stiffness matrix of the element Ω_e. We can easily construct a complete stiffness matrix $\mathbf{K}$ by computing the integrals $k_{i,j}$ for each element and adding them together with all the DOFs in the domain. Since the basis functions are bilinear, the gradients are linear in the orthogonal direction to the derivation. Then, (2-30) is the integral of a second-degree polynomial that we compute directly. The local stiffness matrix of an element Ω_e is

$$\mathbf{K}_e = \frac{\theta_e}{6h^2}\begin{bmatrix} 4 & -1 & -2 & -1 \\ -1 & 4 & -1 & -2 \\ -2 & -1 & 4 & -1 \\ -1 & -2 & -1 & 4 \end{bmatrix} . \tag{2-31}$$

This is a diagonally dominant matrix for $0 < \theta_e$, then it is positive semidefinite.

Material properties represented by the Q_1 space

We consider also the case when the material property is represented by basis functions $\psi_k \in Q_1$. In this case, the basis functions for the material properties in a single square element are 4. Then we can compute the element local stiffness matrix as the sum of the contributions of each basis function for material properties ψ_k

$$\mathbf{K}_e = \sum_k \theta_k \int_{\Omega_e} \psi_k \nabla\phi_j \nabla\phi_i \, , \qquad i,j,k \text{ such that } x_i, x_j, x_k \in \Omega_e \, . \tag{2-32}$$

As ψ_k is bilinear and $\nabla\phi_i$, $\nabla\phi_j$ are linear, we obtain a third-degree polynomial in one variable times a first-degree in the other one. The partial local stiffness matrix for one of the nodal variables θ_k is given by

$$\mathbf{K}_{e,k} = \frac{\theta_e}{6h^2}\begin{bmatrix} 3 & -1 & -1 & -1 \\ -1 & 2 & & -2 \\ -1 & & 1 & \\ -1 & -1 & & 2 \end{bmatrix} . \tag{2-33}$$

Here the first degree of freedom (DOF) corresponds to the node of the material basis function. The second and fourth degrees of freedom are related to the neighboring nodes in the same cell, while the third one is related to the opposite corner. The stiffness matrices for the other nodes are permutations of the DOF of (2-33). Mixing (2-32) and (2-33) we obtain

$$\mathbf{K}_e = \sum_k \mathbf{K}_{e,k} \, .$$

A complete matrix for a $\psi_k \in Q_1$ basis function of material includes the relations with the eight nodes around selected the node (for a non-boundary node), this means a 9×9 matrix.

Using the numeration in **2-1**b, this matrix is

$$\mathbf{K}_k = \sum_e \mathbf{K}_{e,k} = \frac{\theta_k}{6h^2} \begin{bmatrix} 1 & & & & -1 & & & & \\ & 2 & & -1 & -1 & -1 & & -1 & \\ & & 1 & & -1 & & & & \\ & -1 & & 2 & -1 & -1 & & -1 & \\ -1 & -1 & -1 & -1 & -3 & -1 & -1 & -1 & -1 \\ & -1 & & -1 & -1 & 2 & & -1 & \\ & & & & -1 & & 1 & & \\ & -1 & & -1 & -1 & -1 & & 2 & \\ & & & & -1 & & & & 1 \end{bmatrix} . \tag{2-34}$$

Here the sum over the index e is in the support of ψ_k. Matrices (2-31) and (2-34) are used to assemble Q_0 and Q_1 density representation schemes respectively for the optimization of material, as we see in Chapter 3. Similar integration procedures are performed with equations (2-6), (2-7) and (2-8) to obtain the rigidity matrix for the elasticity problem.

Change of representation

Suppose that we have the information of the conductivity (or any other material property) of a domain Ω represented by the linear combination

$$\boldsymbol{\Theta}^{(1)}(x) = \sum_{j=1}^{N_1} \theta_j^{(1)} \psi_j^{(1)}(x) \,, \qquad \psi_j^{(1)} \in V^{(1)} \,, \qquad N_1 = \dim\left(V^{(1)}\right) .$$

And we want to represent the information in another space $V^{(2)}$

$$\boldsymbol{\Theta}^{(2)}(x) = \sum_{i=1}^{N_2} \theta_i^{(2)} \psi_i^{(2)}(x) \,, \qquad \psi_i^{(2)} \in V^{(2)} \,, \qquad N_2 = \dim\left(V^{(2)}\right) .$$

We can use then the $\mathcal{L}_2$-*projection* between spaces. In this projection, we compute every coefficient of the $V^{(2)}$ representation in the following way

$$\theta_i^{(2)} = \sum_{j=1}^{N_1} \theta_i^{(1)} \int_\Omega \psi_j^{(1)} \psi_i^{(2)} \,, \qquad i = 1, ..., N_2 \,. \tag{2-35}$$

Notice that (2-35) is a system of linear equations, that can be represented as

$$\boldsymbol{\Theta}^{(2)} = \mathbf{T}^{(1,2)} \boldsymbol{\Theta}^{(1)} \,. \tag{2-36}$$

Here $\mathbf{T}^{(1,2)}$ is a matrix of coefficients $T_{ij} = \int_\Omega \psi_j^{(1)} \psi_i^{(2)}$. In a similar way

$$\boldsymbol{\Theta}^{(1)} = \mathbf{T}^{(2,1)} \boldsymbol{\Theta}^{(2)} \,. \tag{2-37}$$

Spaces $V^{(1)}$ and $V^{(2)}$ can be any of the finite subspaces of $\mathcal{L}_2(\Omega)$ presented before, like the spaces $Q_0(\Omega)$ and $Q_1(\Omega)$. These spaces can be of the same type but different mesh too, for example, two Q_0 spaces, one with a coarse and one with a fine mesh. We will use these projections in Chapter 5 to analyze some properties of the solutions to the topology optimization problems in this work.

3 Topology optimization

Optimizing material distribution is a problem that depends on the representation we use for the material field. This representation, in turn, depends on the mathematical tools available to solve the physical problem. After the successful development of the solid isotropic material penalization (SIMP) method to improve material distribution in applied problems, see [Bendsøe and Sigmund, 2004], many new approaches to the problem have been developed, see [Rozvany, 2009, Sigmund and Maute, 2013]. To study the problem, we choose a set of methods we believe could improve our understanding of the broad problem. In this chapter we draw from several sources, mainly [Bendsøe and Sigmund, 2004, Smith and Norato, 2020, Wein et al., 2020].

3.1 Introduction

A comprehensive introduction to topology optimization is given in [Bendsøe and Sigmund, 2004]. Here a rather straightforward description of topology optimization is given. In a domain $\Omega \subset \mathbb{R}^n$, with $n = 2$ or $n = 3$, the main problem is to find an optimal material disposition for a mathematical model of some physical phenomenon that depends on that disposition. The material distribution can be given in terms of a variable ρ describing, for example, the density distribution or a parameterization of a material boundary [Wein et al., 2020]. The performance of a particular material distribution is measured by a functional F, which is the description of a set of requirements. Mathematically, we need to solve

$$\min_{\rho} F(u(\rho), \rho) \ . \tag{3-1}$$

The functional F is given in terms of u, a quantity that depends on ρ through a physical model equation. The quantity u can be a displacement field or a temperature and often the relation with ρ is given by a system of partial differential equations (PDE). In this case, in order to solve the minimization problem, the numerical approximation of the physical model must be computed in each iteration of the optimization procedure. The most common formulation of this problem is the optimization of the energy in the system, also known as the minimum compliance problem. This problem depends on the cost functional

$$c(u(\rho)) = \int_{\Gamma_f} u(\rho) \cdot f \ d\Omega. \tag{3-2}$$

Here c is the compliance of the system and f is the load over the boundary Γ_f. It is also possible to minimize the overall magnitude of the field, computed in terms of a q-norm:

$$m(u(\rho)) = \left(\int_\Omega |u(\rho)|^q \ d\Omega \right)^{1/q} . \tag{3-3}$$

As q increases, (3-1) with (3-3) becomes a minmax problem, see [Yan et al., 2018]. The problem can be constrained in an arbitrary way, but commonly a volume constraint V_f^* is used. Adding a restriction on the volume, the minimum compliance topology optimization problem is stated as follows.

Problem 2 *Find a distribution of material ρ such that the following functional in terms of the field u is optimized, that is,*

$$\begin{aligned} \textit{min} \quad & \int_{\Gamma_f} u(\rho) \cdot f \ d\Omega, \\ \textit{subject to} \quad & V_f(\rho) \leq V_f^* \quad , \\ & 0 \leq \rho_i \leq 1 \ . \end{aligned} \tag{3-4}$$

Here V_f is the volume of material over the domain

$$V_f(\rho) = \int_\Omega \rho \ d\Omega. \tag{3-5}$$

3.2 The density problem

Assume that we have a partition in squared FEs for the domain Ω in Problem 2, as described in Chapter 2. This partition is a mesh of size $n \times m$. One can assign full-density material or void in each finite element Ω_e, which means we are using a constant value of density inside each FE, see [Bendsøe and Sigmund, 2004]. It is important to note the meaning of this computation, that is, the stiffness corresponding to the Q_1 displacement field with a $\rho \in Q_0$ density representation. In the original problem, we are trying to find a vector of densities ρ of dimension $N = nm$ with

$$\rho_e \in \{\rho_{\min}, \rho_{mat}\} \ . \tag{3-6}$$

Here ρ_e is a component of the density vector ρ corresponding to the element Ω_e, ρ_{mat} is the material density, and we use a minimum density $\rho_{\min}$. As noted in the previous chapter, the density $\rho_{\min}$ is usually chosen as a small positive value to ensure a well-posed BVP. The main advantage of the density representation is that we can always use the same mesh and represent the void elements as elements with very low stiffness, see [Bendsøe and Sigmund, 2004]. This representation is known as an *Ersatz material*, and the constant value of density

allows us to compute a part of the stiffness matrix independently of the value of the density, see [Wein et al., 2020]. The main difficulty is that the search becomes proportional to the term 2^{nm} and classical methods for solving it perform poorly in terms of computation time. The most common approach consists in relaxing the feasible set of the variable ρ_i to be a continuous interval for each cell, that is

$$\rho_e \in [\rho_{\min}, \rho_{mat}] \, . \tag{3-7}$$

Allowing intermediate density values allows the use of gradient and Lagrange multipliers-based optimization methods, see [Deaton and Grandhi, 2014]. This approximation to the problem also allows for a better description of the resulting shape if the mesh remains static throughout the optimization, which leads to limitations in the description of boundaries between regions with and without material, see [van Dijk et al., 2010]. It is also convenient to bound away from zero the design variables, using instead

$$\rho_e \in [\rho_{\min}, 1] \, . \tag{3-8}$$

All information concerning the stiffness is wrapped in a local stiffness matrix $\boldsymbol{K_e}$ that is computed using the normalized density also known as the pseudo-density, that is,

$$\boldsymbol{K_e} = \rho_e \boldsymbol{K_{0,e}} \, . \tag{3-9}$$

Here $\boldsymbol{K_{0,e}}$ is a local stiffness matrix for element Ω_e computed with $\rho = 1$. In the discretized domain, the optimization problem is given as follows.

Problem 3 *Find an optimal distribution of material $\rho \in Q_0$, such that the following functional in terms of the vector of temperature (or displacement) $\boldsymbol{u}$ and the load vector $\boldsymbol{f}$ is minimized.*

$$\begin{aligned} \min_{\rho \in Q_0} \quad & \boldsymbol{u}^T(\rho)\boldsymbol{f} \, , \\ \textit{subject to} \quad & \frac{1}{N}\sum_{e=1}^{N} \rho_e \leq V_f^* \, , \\ & 0 < \rho_{min} \leq \rho_e \leq 1 \, , \qquad e = 1, ..., N \, . \end{aligned} \tag{3-10}$$

Here V_f^* is a maximum fraction of material in the domain. Vectors $\boldsymbol{u}$ and $\boldsymbol{f}$ must satisfy the additional restriction

$$\boldsymbol{K}(\rho)\boldsymbol{u} = \sum_{e=1}^{N_e} \rho_e \boldsymbol{K}_{0,e} \boldsymbol{u}_e = \boldsymbol{f} \, . \tag{3-11}$$

Here $\boldsymbol{K}$ is the global stiffness matrix, N is the number of elements, ρ_e is the density in the element Ω_e, $\boldsymbol{K}_{0,e}$ is a local stiffness matrix for the element and u_e is the nodal displacement

in the element Ω_e. In the case of same-size elements the local stiffness matrix is computed using the same stiffness matrix $\boldsymbol{K}_0$. The functional in (3) can be rewritten as

$$c(u) = \boldsymbol{u}^T \boldsymbol{K}(\rho)\boldsymbol{u} = \boldsymbol{f}^T \left(\sum_{e=1}^{N_e} \rho_e \boldsymbol{K}_{0,e} \right)^{-1} \boldsymbol{f} \ .$$

Problem 3 is convex, therefore it has a unique solution, see [Bendsøe and Sigmund, 2004]. A vector solution should have most (if not all) densities as described in equation (3-6). If this is not the case, the solutions could have significant portions with intermediate densities also known as gray zones which are very common when implementing this convex minimization problem.

To overcome the existence of gray areas in the solution, the effective density used to describe the domain is penalized or interpolated [Bendsøe and Sigmund, 1999]. In the eighties and nineties, the Solid Isotropic Material with Penalization (SIMP) method was proposed: a power law is applied homogeneously to every density. That is, we consider the penalized density

$$\rho_{pen} = \rho^p \ . \tag{3-12}$$

Here p is a penalization constant commonly set to the value of 3 as is it the minimum exponent satisfying the upper Hashin-Shtrikman bounds, see [Sigmund and Petersson, 1998] and Figure **3-1**. A simple implementation of this method is presented in [Andreassen et al., 2010]. When using the SIMP method is possible to find solutions without gray zones and with the help of post-processing algorithms we can also find a parametrized description of the boundary, see [Bendsøe and Sigmund, 2004]. There is a difficulty when applying such penalization directly: the power law applied to a small number $\rho_i = \rho_{\min}$ could transform it into a number even closer to 0, causing the singularity of the stiffness matrix. Then the element stiffness is computed using the following updated formula (the so-called modified SIMP scheme)

$$E_e(\rho_e) = E_{\min} + \rho_e^p (E_0 - E_{\min}) \ , \tag{3-13}$$

with E_e the stiffness of the element, $E_{\min}$ a small lower bound to prevent singularity in the global stiffness matrix, E_0 is the base stiffness and ρ_e is the density term. In a discretized domain, the optimization problem is posed as follows.

Problem 4 *Find an optimal distribution of material $\rho \in Q_0$, such that the following functional in terms of the vector of temperature (or displacement) $\boldsymbol{u}$ and the load vector $\boldsymbol{f}$ is minimized,*

$$\begin{aligned} \min_{\rho} \quad & \boldsymbol{u}^T(\rho)\boldsymbol{f} \ , \\ \textit{subject to} \quad & \frac{1}{N_e}\sum_{i=1}^{N_e} \rho_i \leq V_f^* \ , \\ & 0 < \rho_{min} \leq \rho_i \leq 1 \ . \end{aligned} \tag{3-14}$$

Here V_f^* is a maximum fraction of material in the domain. Vectors $\boldsymbol{u}$ and $\boldsymbol{f}$ must satisfy the additional restriction

$$\boldsymbol{K}(\rho)\boldsymbol{u} = \sum_{e=1}^{N} E_p\left(\rho_e\right) \boldsymbol{K}_{0,e}\boldsymbol{u} = \boldsymbol{f}\ . \tag{3-15}$$

The constant p is chosen in $[1, \infty)$ and $E_p(\rho)$ as in (3-13).

Choosing an appropriate value of p delivers $0-1$ designs for this problem, but it is no longer convex and usually presents mesh dependence problems, see [Sigmund and Petersson, 1998]. We see solutions to this problem in Chapter 4, which are generally formed by a connected composition of elongated zones of material transporting a flux of temperature or traction; we refer to these zones as *members* in this work.

3.2.1 Interpolation of material

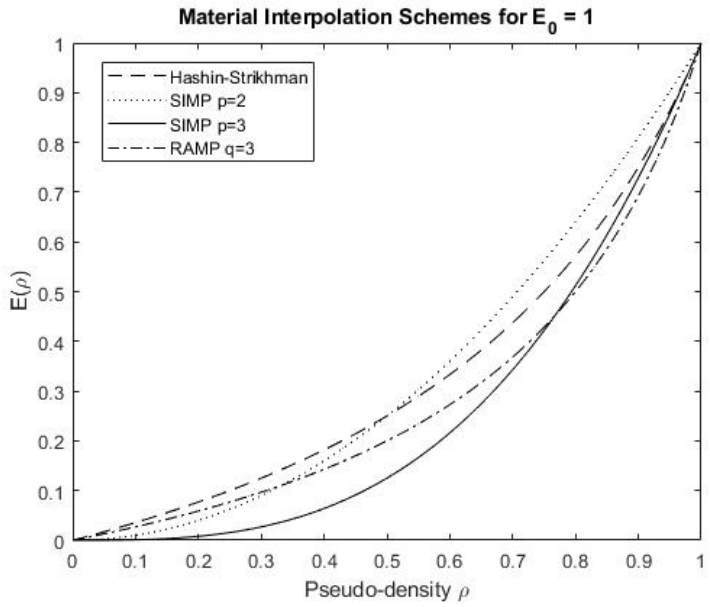

Figure 3-1: Material interpolation schemes for the stiffness constant as a function of the pseudo-density.

From an optimization point of view, penalizing variables is a numerical strategy to obtain 0-1 solutions. However, there is a physical interpretation to the penalization related to the homogenization method, [Bendsøe and Sigmund, 2004]. In the homogenization method, we suppose that we only have two types of material (full or void) in our domain with details in the material distribution smaller than the minimum scale of our design problem. In the mixed material zones, we have some micro-structure with some elasticity tensor that we in turn approximate as a simpler tensor in the macro-structure. This interpretation of the

material distribution gives us a physical justification for the relaxation of the design space, and in this sense, we can call the penalization used a *material interpolation scheme*. In this work, we assume that the material and the microstructure are isotropic (since we could also consider an anisotropic modeling of the material or the homogenization) and that the Poisson's ratio of the elastic material is independent of the pseudo-density of the design variables, see [Bendsøe and Sigmund, 1999]. Following the homogenization method, we can obtain bounds for the behavior of the isotropic composite two-phase material microstructure, known as Hashin-Strikhman bounds. We are generally interested in the upper Hashin-Strikhman bound, which for a material interpolation scheme $E(\rho)$ in two dimensions gives us the following (3-16), see [Bendsøe and Sigmund, 1999],

$$0 \leq E(\rho) \leq \frac{\rho E_0}{3 - 2\rho} \, . \tag{3-16}$$

The bound becomes for the SIMP method

$$\max \left\{ \frac{2}{1 - v_0}, \frac{4}{1 + v_0} \right\} \leq p \, . \tag{3-17}$$

Here the Poisson ratio of the full-density material is v_0 and p the penalization exponent in (3-12). For $v_0 = 13$ the minimum exponent satisfying the upper bound is $p = 3$. In [Bendsøe and Sigmund, 1999] the authors also explore the realization of the micro-structure of a SIMP interpolation. An alternative scheme for interpolation is the Rational Approximation of Material Properties (RAMP), given by

$$E(\rho) = \frac{\rho}{1 + q(1 - \rho)} E_0 \, . \tag{3-18}$$

Here q is a parameter we can increase to increase the penalization of intermediate densities. Notice that for $q = 2$, equation (3-18) equals (3-16). See [Bendsøe and Sigmund, 2004]. In this work we focus mainly on the SIMP interpolation in the simulations presented in the following chapters.

3.2.2 Checkerboard patterns and mesh dependency

These algorithms often deal with mesh dependency problems (the computation and results depend on the mesh and the discretization) and very commonly also deal with the existence of *checkerboard patterns*, a problem related to the overestimation of stiffness values cell corners, [Sigmund and Petersson, 1998]. The checkerboard patterns consist of artificially high-stiffness regions in the form of alternating 0-1 meshes as illustrated in Figure **3-2**.
Consider the domain in Figure **3-2**a and the distributions of material in Figure **3-2**b and Figure **3-2**c. If the stiffness matrix for the heat problem is computed and the submatrix consisting of the red nodes is extracted, then one can see that the matrices have important

(a) Domain (b) Homogeneous (c) Checkerboard

Figure 3-2: Distributions of material in a squared domain of 4×4 elements and size 4×4. Although the distributions are quite different, in the nodes signaled with $\cdot$ in red in (a) the stiffness matrix entries are similar.

similarities. We have for distribution in Figure **3-2**b

$$K_b = \frac{1}{6}\begin{bmatrix} 8 & -1 & & -1 & -1 & & & & \\ -1 & 8 & -1 & -1 & -1 & -1 & & & \\ & -1 & 8 & & -1 & -1 & & & \\ -1 & -1 & & 8 & -1 & & -1 & -1 & \\ -1 & -1 & -1 & -1 & 8 & -1 & -1 & -1 & -1 \\ & -1 & -1 & & -1 & 8 & & -1 & -1 \\ & & & -1 & -1 & & 8 & -1 & \\ & & & -1 & -1 & -1 & -1 & 8 & -1 \\ & & & & -1 & -1 & & -1 & 8 \end{bmatrix}. \tag{3-19}$$

And for the distribution in Figure **3-2**c

$$K_c = \frac{1}{6}\begin{bmatrix} 8 & -1 & & -1 & \mathbf{-2} & & & & \\ -1 & 8 & -1 & \mathbf{-2} & -1 & -- & & & \\ & -1 & 8 & & -- & -1 & & & \\ -1 & \mathbf{-2} & & 8 & -1 & & -1 & -- & \\ \mathbf{-2} & -1 & -- & -1 & 8 & -1 & -- & -1 & \mathbf{-2} \\ & -- & -1 & & -1 & 8 & & \mathbf{-2} & -1 \\ & & & -1 & -- & & 8 & -1 & \\ & & & -- & -1 & \mathbf{-2} & -1 & 8 & -1 \\ & & & & \mathbf{-2} & -1 & & -1 & 8 \end{bmatrix}. \tag{3-20}$$

Comparing these two matrices we see that,

$$\|K_b\|_\infty = 2.67\ , \|K_c\|_\infty = 2.67\ ,\ \text{and}\ \|K_b - K_c\|_\infty = 0.67\ .$$

These regions have almost the same stiffness as a gray region, but satisfy the requirement to provide 0-1 designs. This problem introduces small holes of material into the discretized domain as small as the mesh, and in turn causes a high dependence on the solution: the finer the mesh the more holes with artificial stiffness are introduced, and a material with microscopic holes does not behave as predicted by the FEM method with these patterns, as the real effect in the stiffness of a porous material is worse [Bendsøe and Sigmund, 2004]. If a region in the solution of the non-penalized problem is gray (has partial pseudo-density), then the penalized solution could have a zone with checkerboard patterns. Solutions to this problem vary, the simplest being to introduce an image filter [Sigmund and Petersson, 1998]. More on this in the following section.

3.2.3 Filtering

A linear image filter is a linear mapping, defined over the space of densities R

$$\begin{aligned} H :& R \to R \\ & \rho \mapsto \tilde{\rho} = H\rho \end{aligned} \tag{3-21}$$

Depending on the definition of the problem we have $R = Q_0$ or $R = Q_1$, see Section 3.2.

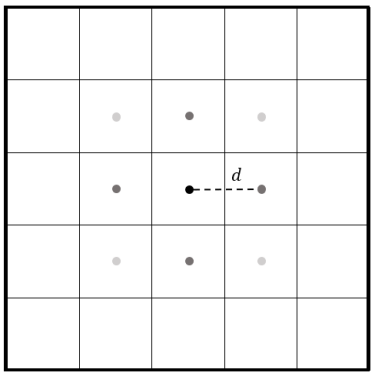

Figure 3-3: Elements used to compute the final filtered pseudo-density of the central element. The weight of each element in the average is represented in a gray scale and is dependent on the distance to the center of the element.

The action of the filter can be understood in terms of a kernel. For example, see Figure **3-3**, this image represents the local elements used to compute the final value of the pseudo-density of an element i, consisting of the neighboring elements. To compute the final value for the position i, a weighted average can be used. That is

$$\tilde{\rho_i} = \frac{\sum_{j=1}^{N} a_j \rho_j}{\sum_{j=1}^{N} a_j}\ . \tag{3-22}$$

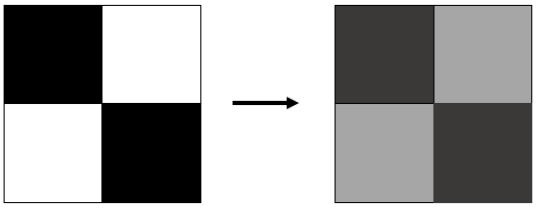

Figure 3-4: Representation of the effect of a linear filter on a checkerboard pattern. The blurring effect of the mapping transforms the patterns in grey designs, and in turn, the penalization makes them expensive. This way, the optimizer avoids these patterns and gives preference to wide regions of homogeneous material.

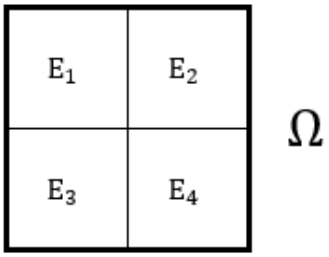

Figure 3-5: Example of a squared domain consisting of four elements. The application of a weighted average kernel changes the gain in different principal directions. Alternate patterns of material get blurred and optimization avoids them because of the penalization.

The coefficients can be computed with the formula

$$a_j = \max\{0, r - d_j\} \ .$$

Here r is a prescribed radius known as the filter width and d_j the Euclidean distance between the quadrature points ρ_i and its neighbor ρ_j. When using this average, the effect over an image is that of blurring it. In a very intuitive way, we could say that the blurring can make checkerboard patterns and other small details on the density distribution lose some contrast, making the penalization see them as gray areas, see Figure **3-4**. These filtered and penalized gray areas are then avoided by the optimizer. To understand a little better this effect, consider for example the simple and small domain in Figure **3-5**, consisting of only two neighboring elements. And consider a filter with the following kernel

$$H = \frac{1}{5}\begin{bmatrix} 3 & 1 & 1 & \\ 1 & 3 & & 1 \\ 1 & & 3 & 1 \\ & 1 & 1 & 3 \end{bmatrix} \ .$$

In this filter the main element is given three times the weight given to the neighboring elements. Now, using eigenvalue decomposition we see the eigenvectors and the eigenvalues

$$v_1 = \begin{bmatrix} 1/2 \\ -1/2 \\ -1/2 \\ 1/2 \end{bmatrix}, \; v_2 = \begin{bmatrix} -\sqrt{2}/2 \\ \\ \\ \sqrt{2}/2 \end{bmatrix}, \; v_3 = \begin{bmatrix} \\ \sqrt{2}/2 \\ -\sqrt{2}/2 \\ \end{bmatrix}, \; v_4 = \begin{bmatrix} 1/2 \\ 1/2 \\ 1/2 \\ 1/2 \end{bmatrix} .$$

$$\lambda_1 = 1/5, \; \lambda_2 = 3/5, \; \lambda_3 = 3/5, \; \lambda_4 = 1 \; .$$

In the direction v_4, the kernel matrix does not produce any effect. This is the direction where the densities are uniform, that is, every density has the same value. In the direction v_1 representing alternated tiles of material, the filter diminishes the gain to $1/5$. If the filter is embedded in the optimization process, then the optimizer cannot reach the corner values $[0, 1, 1, 0]$ and $[1, 0, 0, 1]$, but will have a preference to uniform points, and will try to avoid checkerboard patterns, see [Bendsøe and Sigmund, 2004]. This effect increases with the radius of the filter and can have local and non-local effects. More on this in Chapter 4.

3.3 Some variations of the method of densities

The element-uniform density representation is not the only one used in TO. In general, different combinations of representation spaces for the densities and the physical field have been explored and some have proven to have advantages over the previous method. In this section, we explore an alternative formulation found in the literature and a different formulation proposed in this work. See [Rahmatalla and Swan, 2004].

3.3.1 Continuous density representation

If we choose a density field represented by Q_1 basis functions the density field becomes a continuous function. The procedure is analogous to the method originally presented in Section 3.2, the difference is that each optimization variable is now the nodal value of the density, rather than the element value, see Figure **3-6**. In general, we can choose any density representation including higher degree-polynomials or quadrature points of density located in other points instead of the center or the nodes of the element, see for example [Paulino and Le, 2009]. Additionally, smooth spaces of polynomials of degree greater than five eliminate the need for a filter to prevent mesh-dependency problems, see [Sigmund and Petersson, 1998]. Keeping the assumption of a correspondence between material properties and pseudo-density, for instance, for the heat problem we can write,

$$\boldsymbol{\Theta}(x) = \sum_k \theta_k \psi_k = \sum_k \rho_k \psi_k \; .$$

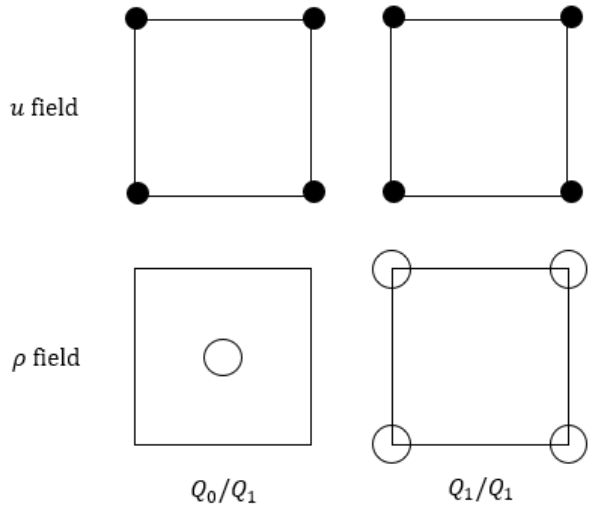

Figure 3-6: DOF of the fields in Q_0 and Q_1 density representations. Figure adapted from [Rahmatalla and Swan, 2004]

Here ψ_k are the basis functions of the space Q_1. The mapping from the density to the physical field is straightforward: each nodal density basis function ψ_k in the node k is integrated with the basis functions for the trial and test spaces

$$\mathbf{K}_{i,j} = \int_\Omega \mathbf{\Theta}(x)\nabla\phi_j\nabla\phi_i = \sum_k \rho_k \int_\Omega \psi_k \nabla\phi_j\nabla\phi_i\,, \qquad i,j = 1,2,...,N\,.$$

Here the sum on the index k is in k such that $x_k \in \text{supp}(\phi_i) \cap \text{supp}(\phi_j)$. The result of this integration for a single basis function ψ_k is presented in (2-34). When the interpolation is linear, we extract the optimization variables from the resulting stiffness matrix associated with the 9 nodes (or less in the boundaries and the corners of the domain) influenced by the Q_1 basis, see Figure **3-7**. We have now the following representation for the full rigidity matrix

$$\boldsymbol{K}(\rho)\boldsymbol{u} = \sum_{k=1}^{N_n} \rho_k \boldsymbol{K}_{0,k}\boldsymbol{u}_k = \boldsymbol{f}\,. \tag{3-23}$$

Here we have changed the sum index to represent the sum on every node k, and $\mathbf{K}_{0,k}$ represents a local stiffness matrix of 9 nodes in central elements, 6 in the boundaries and 4 in the corners. When we penalize the stiffness matrix we can assume that the penalization only will affect the density variable, see the *proportional* combination in Figure **3-7**,

$$\boldsymbol{K}_k = \rho_k^p \boldsymbol{K}_{0,k}\,, \tag{3-24}$$

or that it will affect the density value in every point of the domain, see *theoretical* in Figure **3-7**. When this happens, we cannot use (2-29), rather we compute the integrals of the

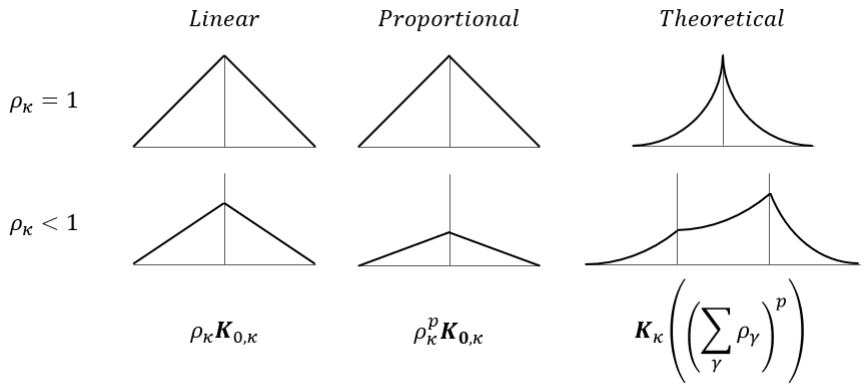

Figure 3-7: The penalization of the density variable can be interpreted in different ways. When the interpolation is linear (left) the height of the density segment is scaled proportionally to the density variable. When the interpolation implements penalization, it can affect the basis function linearly (center) or the whole basis function (right) and the combination over a single element, adding complexity to the computation.

components of the global stiffness matrix for each iteration of the optimization

$$\mathbf{K}_{i,j} = \int_\Omega \left(\sum_k \rho_k \psi_k\right)^p \sum_j \nabla\phi_j \nabla\phi_i \,, \qquad i,j = 1,2,...,N \,.$$

Here the sum on the index k is done in k such that $\text{supp}(\phi_i) \cap \text{supp}(\phi_j) \cap \text{supp}(\psi_k) \neq \emptyset$. This acts in practice like a filter of densities, provided that contiguous nodal variables interact directly in the optimization. In this work, we consider for simplicity the equation (3-24). The method presents an overestimation of the stiffness values in certain components $k_{i,j}$ and then presents solutions with structures similar to checkerboard patterns, called *layering* and *islanding*. Due to this situation, the method must also implement a filter of densities or perimeter control to yield useful results. In [Rahmatalla and Swan, 2004] the authors explore the stability of the method with perimeter control.

3.3.2 Discontinuous density representation

The previous two methods share most of the design calculation steps except for the representation of the density field. Due to the similitude, we studied the possibility of a density representation able to generalize the two methods. In this work, we explored a generalization based in the decomposition of the basis functions for the Q_0 and Q_1 spaces. In Figure **3-8** we can see how the Q_1 basis for densities is a composition of 4 bilinear functions $C^1(\Omega_e)$ in different elements Ω_e sharing a common nodal point. That is, the basis function $\phi_{i,j}$ for the

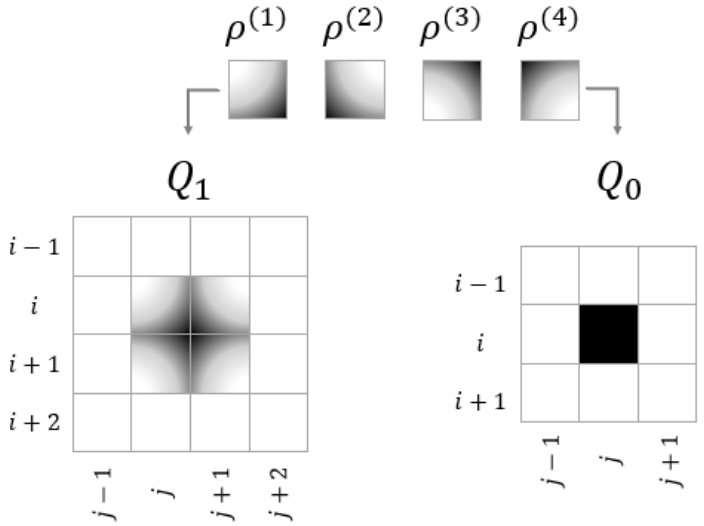

Figure 3-8: Representation of the construction of the Q_0 and Q_1 basis functions for density representation using bilinear functions $\rho^{(k)}$, this bilinear functions have 3 corners with 0 value and one corner with 1 value. Full density is represented in black and the absence of material is in white. In Q_1, the basis functions are constructed by gluing 4 segments ρ by the same node. In Q_0, the segments are added to the same element.

node i, j can be computed as

$$\phi_{i,j} = \rho^{(1)}_{i,j} + \rho^{(2)}_{i,j+1} + \rho^{(3)}_{i+1,j} + \rho^{(4)}_{i+1,j+1}$$

The indices in this sum indicate the element where the support of the bilinear segment lies. The point of this decomposition is that the Q_0 basis functions can be also represented by the sum of the same basis functions, but in the same element i, j

$$\phi_{i,j} = \rho^{(1)}_{i,j} + \rho^{(2)}_{i,j} + \rho^{(3)}_{i,j} + \rho^{(4)}_{i,j}$$

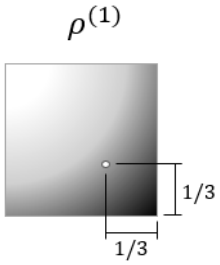

Figure 3-9: Centroid of a DQ_0 element with value $\phi(x) = 1$ in the bottom right corner.

We call this new space DQ_1 and note that $Q_0, Q_1 \subset DQ_1$, this is, the new representation contains the previous density representations. The direct implementation of an optimization process with these bilinear segments delivers solutions with a mixture of checkerboard patterns and islanding, problems of the Q_0 and Q_1 representations, respectively. Then it is necessary to apply filtering to obtain reasonable solutions. In general, it is possible to build a linear filter, similar to those implemented for Q_0 and Q_1 representations. Here we consider an approach based on the centroid of the $DQ0$ basis function.

In Fig. **3-9** we can observe that the centroid of the basis function is located at 1/3 of the height/width of the corner where the basis function is 1. Based on this we can build a linear filter H_{DQ0} based on distances as we did in Subsection 3.2.3. With this implementation, the coefficients of the linear combination of basis functions with a higher coefficient and influence in the filter applied on each density value would be those in the same element. We present results of this method for the heat problem in Chapter 4.

3.4 Geometry projection topology optimization (GPTO)

There is a set of methods referred to as *feature-mapping methods* [Wein et al., 2020], that use an explicit representation of geometric forms to place material in the domain. This method was introduced in [Bell et al., 2012] and [Norato et al., 2015] with bar primitives and an educational code library was made available in [Smith and Norato, 2020]. In this section, we follow the description of the method in [Smith and Norato, 2020].

3.4.1 Bar primitives

A set of geometric primitives is placed in the domain to represent the distribution of material, which is mapped or *projected* onto a density field. Each primitive b is described in the domain using a set of parameters hereafter denoted by z_b.
In [Smith and Norato, 2020], the authors consider bar-shaped primitives, as an example of this methodology. Each bar b has a pair of end points x_{1b} and x_{2b} and a radius r_b, see Figure **3-10**a. The radius represents an *offset* surface from the line formed by the endpoints. This is a straightforward and convenient parameterization as we will see in the following subsections. For the parameters z_b, the following constraints are included

$$\begin{aligned} x_{1b}, x_{2b} &\in \Omega \ , \\ r_{b-\min} \leq & r_b \leq r_{b-\max} \ . \end{aligned} \tag{3-25}$$

The first constraint tells us that the endpoints of the bars must always lie inside the design domain. The bounds on the radius $r_{b-\min}$ and $r_{b-\max}$ are modified to control the length scale of the members in the solution. If $r_{b-\min} = r_{b-\max}$, the radius of the bar is fixed in the optimization process. A parameter $\alpha_b \in [0, 1]$ is added to each bar as a design variable in the

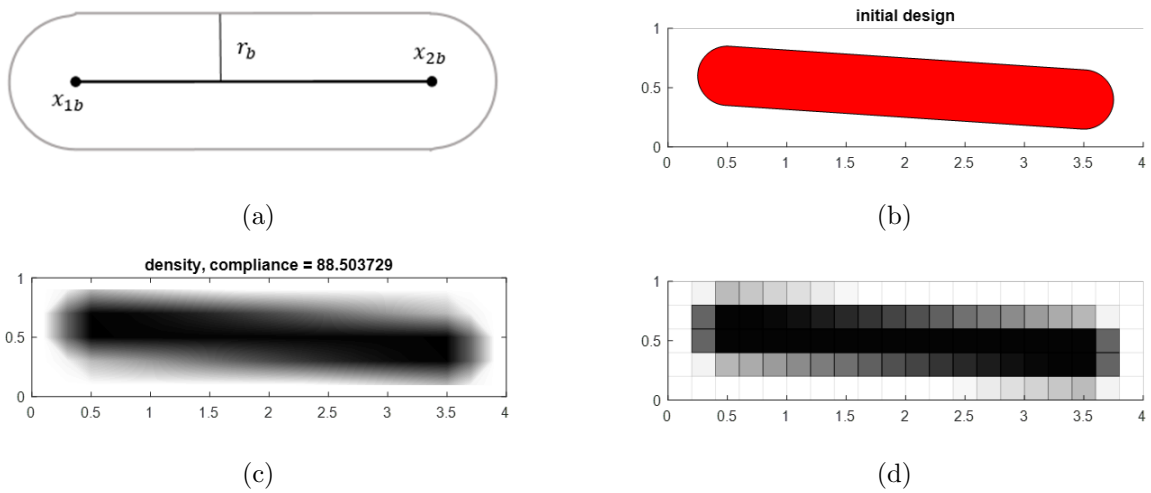

Figure 3-10: Geometry Projection Method with offset bars as primitives in a 2D domain. (a)The bar as an offset surface generated by a line. (b) Example bar in some domain and two possible representations in a density field (c) and (d)

optimization process, to describe the influence of the bar in the final design. This parameter is understood in [Smith and Norato, 2020] as a *size* of the bar and it can be thought of as the maximum pseudo-density that a primitive can *add* to a density variable in the density field, as detailed later.

3.4.2 Mapping of the primitives to a density field

To transform the geometric representation of the problem into a density representation in a Q_0 or a Q_1 space, we need a strategy to map the primitives to values of the coefficients of the linear combination $\sum_k \rho_k \psi_k(x)$. To do this, we take advantage of the compact support of the basis functions ψ_k. We assume initially that if there is a geometric primitive in the domain, it will add to the pseudo-density value ρ_k only if the primitive overlaps with the support of ψ_k. In [Smith and Norato, 2020], the Q_0 representation space is used. With this space, the support of a basis function ψ_k is just the element Ω_k. Then we search for a way to compute the intersection of the area Ω_b covered by a primitive b with each squared element Ω_k. This intersection would be represented in the following way

$$\rho_k = \frac{|\Omega_k \cap \Omega_b|}{|\Omega_k|} \, . \tag{3-26}$$

Here $|\cdot|$ is the value of the area. It is possible to generalize the method to any space and in the case of the Q_0 space is numerically possible to find the value of this intersection with an efficient implementation. However, in [Smith and Norato, 2020] the authors choose a different approach to compute the value of each ρ_k. They assume initially that each squared

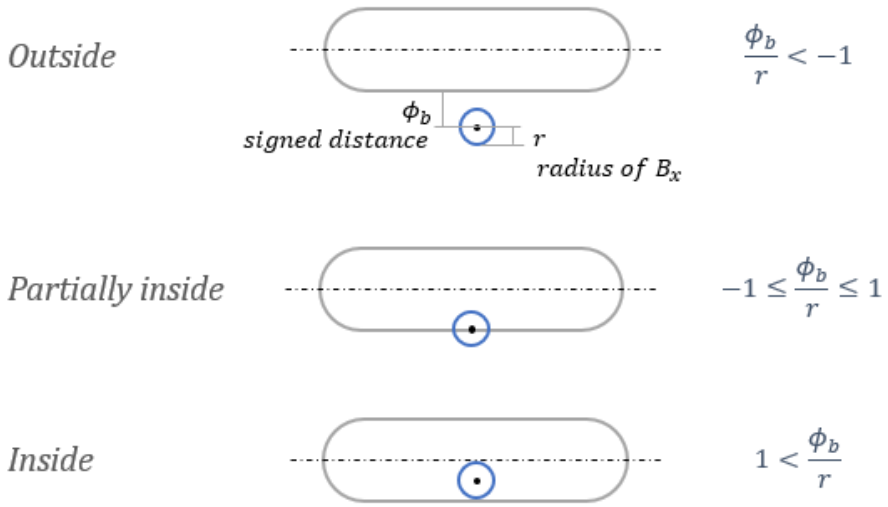

Figure 3-11: Signed distance computation.

(cubic in three dimensions) subdomain Ω_k can be represented by a ball B_x centered in the point x, matching the center of the FE Ω_k. The radius r_k of this ball can be chosen as the width of the element $h = r_k$, and can be computed to match the area $|\Omega_k| = \pi r_k^2$ (or any other criterion chosen by the designer of the method). This approach is convenient, since we have a simple description of the area covered by the bar and the area covered by a ball, and we can easily determine if a point is inside the bar or the ball, if the two of them intersect and we can even compute a distance between the surfaces of the primitive and the ball.

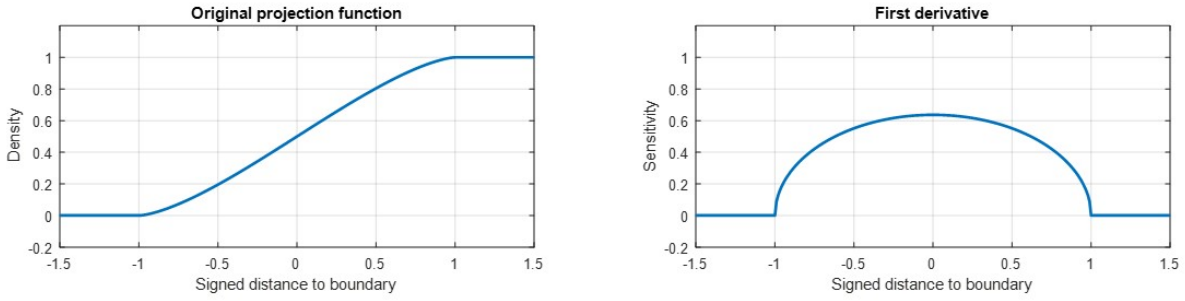

(a) Function h(x).

(b) Derivative h'(x).

Figure 3-12: Original projection function used in [Smith and Norato, 2020], based on the intersection of a ball with a straight boundary.

The signed distance ϕ_b is a distance that includes the case when there is an intersection, see Figure **3-11**. When there is no intersection, $\rho_k = 0$ and consequently $\phi_b \leq -r_k$. If the ball is fully inside the primitive, that is $\rho_k = 1$, then $r_k \leq \phi_b$. The partial intersection is represented by a value in the interval $\phi_b \in [-r_k, r_k]$, attaining $\phi_b = 0$ if the center of B_x is in the surface of the primitive. We can choose a function $h\left(\phi_b/r_k\right)$ mapping between the signed distance and a value of pseudo-density in $[0, 1]$. The exact details of the computation of ϕ_b are found in [Smith and Norato, 2020] and we limit ourselves to mention that this function is continuous and differentiable. In the same article the authors choose

$$h\left(\phi_b/r_k\right) = \begin{cases} 0\ , & \text{if } \phi_b/r_k < -1\ , \\ a(\phi_b/r)\ , & \text{if } -1 \leq \phi_b/r_k \leq 1\ , \\ 1\ , & \text{if } 1 < \phi_b/r_k\ . \end{cases} \tag{3-27}$$

Here ϕ_b/r is the distance from the boundary of the bar to the centroid of the element, and $a(\phi_b/r)$ depends on the problem treated. For example, in [Smith and Norato, 2020] the function for a 2D domain is described by an approximation to the area fraction of a circular segment described in (3-26), given by

$$a(x) = 1 - \frac{\arccos(x) + x\sqrt{1-x^2}}{\pi}\ .$$

Here, we refer to this function h in this work as *projection function*. In 3D, this formula corresponds to an approximation of the volume fraction of a spherical cap. Multiple primitives can overlap and their densities are combined using a differentiable max-norm, see [Wein et al., 2020], for example, the p-norm

$$\max(\rho) = \left(\sum_j \rho_j^p\right)^{(1/p)}\ . \tag{3-28}$$

Here, we combine the independent contributions of each primitive to the value of the density cell in the density variable, representing the superposing primitive densities by j. As we now have an analytical description of the densities ρ_k in terms of the parameters z_b for each bar b, the sensitivities of the compliance and volume with respect to the parameters described above can be computed using the chain rule. Since $h(x)$ is constant in empty and full elements the gradient is null for these elements. It is possible to see then that intermediate zones, elements on the boundary of the primitive, are the ones driving the optimization as $a'(x) \neq 0$, see [Wein et al., 2020].

3.4.3 Comments on other projection functions

Alternative functions to map primitives to the density representation could be beneficial for improving the solutions or obtaining different designs. For example, increasing the smoothness of h could help the optimization process. One way of doing this is using a fifth-degree

polynomial like the following

$$p(x) = 0.1875x^5 - 0.625x^3 + 0.9375x + 0.5\ . \tag{3-29}$$

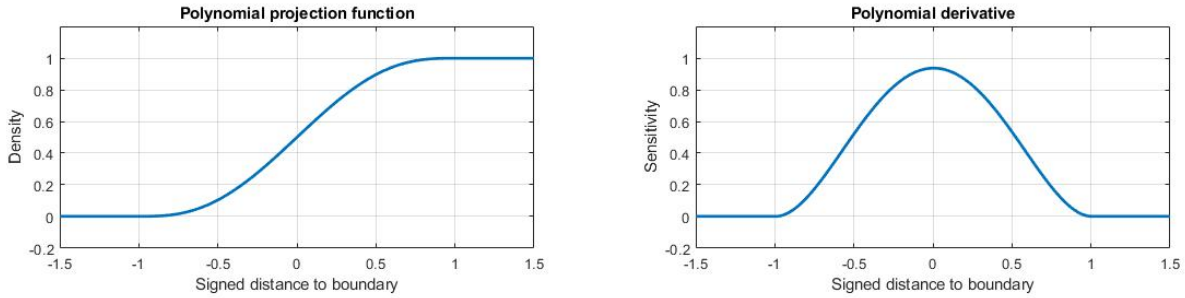

(a) Fifth degree polynomial $p(x)$.

(b) Derivative $p'(x)$.

Figure 3-13: Projection with polynomial function.

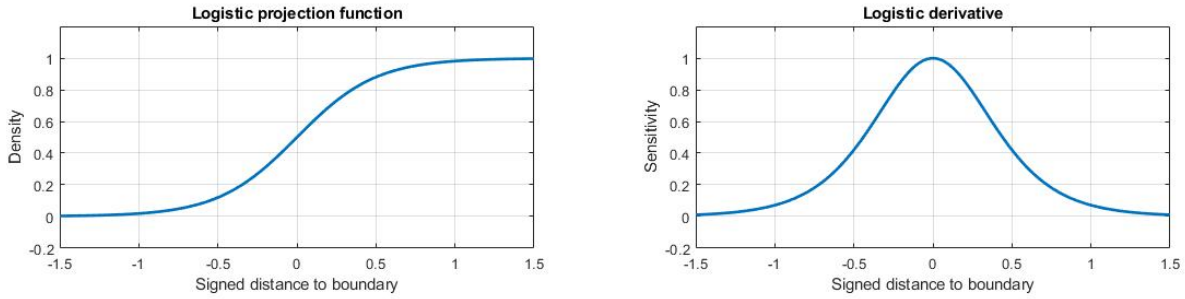

(a) Logistic function $l(x)$.

(b) Derivative $l'(x)$.

Figure 3-14: Projection with logistic function.

When inserted in Equation (3-27), $h \in C^2(\mathbb{R})$ and is used for example with the GPTO method in [Smith and Norato, 2022] to project fiber reinforced plate primitives, demonstrating a small improvement in performance without the significant computational overhead. The form of this polynomial is shown in Figure **3-13**a and its derivative in Figure **3-13**b. In [Wein et al., 2020], it is mentioned that with a spline parameterization the derivative of the element with respect to the parameters of a primitive cancels when the boundary of

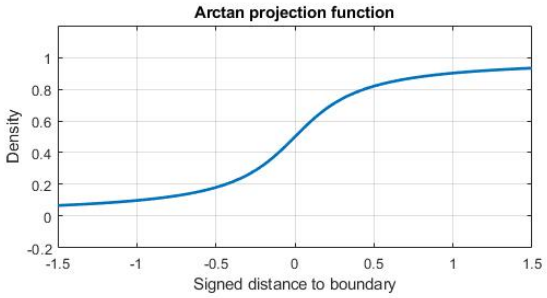

(a) Arctan function at(x).

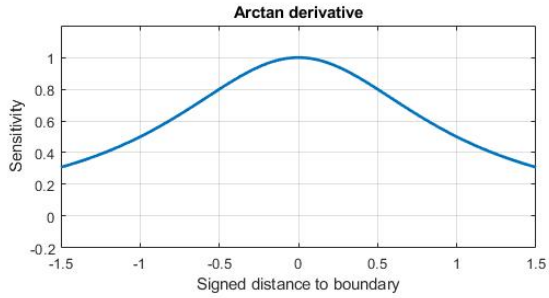

(b) Derivative at'(x).

Figure 3-15: Projection with arc-tangent function.

the primitive matches the mesh partition, this in turn causes the bar to remain fixed in a position. However, it is also true that this is a very specific phenomenon that hardly occurs in practice. Another function $h(x)$ to be considered could be the sigmoid logistic function, used also in [Wein and Stingl, 2018],

$$l(x) = \frac{1}{1 + \exp(-4x)} \ . \tag{3-30}$$

The graph of the sigmoid function is presented in Figure **3-14**a. This function is not of compact support, but converges rapidly to its asymptotes in $y = 0$ and $y = 1$. The derivative of the function in Figure **3-14**b shows that the derivative is not zero in the boundary of the element, but retains a small value away from the boundary of the primitive. The optimization could benefit from this small influence, provided that distant FE without density value, can add to the gradient in the boundary of the primitive closest to the element. This hypothesis is tested later. Finally, we consider the arc-tangent function

$$at(x) = \frac{\arctan(\pi x)}{\pi} + 0.5 \ . \tag{3-31}$$

This function is not of compact support and does not move towards the asymptote as fast as the logistic function, then we can expect primitives with a density less than one near the boundary and elements outside the primitives with a small density value. In both these senses, the use of the material would be less than ideal. The only apparent benefit from the use of this function is that the influence of distant elements on the primitive is stronger, then we could expect an improvement in the final bar disposition but not in the compliance.

4 Numerical solutions

Previously we have discussed the topology optimization framework using finite elements to numerically solve the physical problem. This chapter presents solutions to benchmark problems, introduces the analytical formula for the gradient of the objective function, the most commonly used optimizer, and explores these local solutions. Additionally, we review several modifications to the topology optimization framework aimed at improving local numerical solutions. The works cited in this chapter include [Bendsøe and Sigmund, 2004, Sigmund, 2022, Andreassen et al., 2010, Smith and Norato, 2020, Watada and Oshaki, 2009, Svanberg, 1998, Yan et al., 2018].

4.1 Benchmark problems

Several problems have become standard in the field of topology optimization. These methods are simple enough to analyze the effect of modifications or proposals to the base and long-established methods. Using these benchmarks to validate new concepts and methods is a common practice. This section introduces some of these benchmark problems. See [Sigmund, 2022] and [Bendsøe and Sigmund, 2004].

4.1.1 Benchmark heat conduction problems

The area-to-point problem is a well-known problem to test the heat topology optimization method. It is presented in [Bendsøe and Sigmund, 2004] and has been thoroughly examined both theoretically and numerically in [Yan et al., 2018], where they analyze the properties of a good solution given a specific set of simulation parameters. This problem is suggested in [Sigmund, 2022] to analyze the properties of the method in characteristics related to the minimum length scale. A variant of this problem is used in Chapter 5 to test some properties of the GPTO method, as indicated in Subsection 5.1.1. The definition of this variant problem is provided in the same chapter.

4.1.2 Benchmark elasticity problems

For the linear elasticity model, two classical problems are commonly used: the Michell bridge and the Messerschmitt–Bölkow–Blohm (MBB) beam. The work in [Watada and

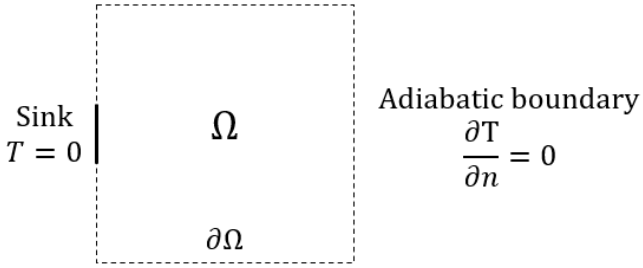

Figure 4-1: Area-to-point problem. Heat is constantly generated at a certain rate g in all the domains, the goal is to distribute certain conductive material of amount v_f^* such that the heat is dissipated to the sink. The size of the domain is 300×300.

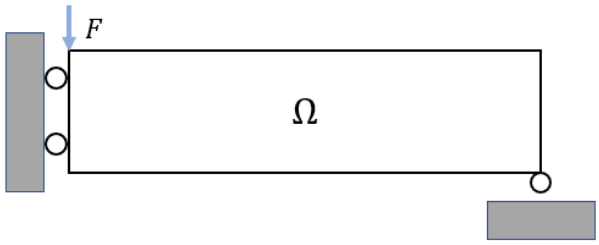

Figure 4-2: Half MBB-beam elasticity problem, a common benchmark problem for topology optimization methodologies. A force of magnitude 1 is applied to the upper left corner. The beam has a horizontal constraint in the left boundary of the domain and a vertical constraint in the bottom right corner. The size of the domain is 200×50. The traction in the subset Γ_2 of the boundary is $h(x) = 0$.

Oshaki, 2009] is also relevant to this document, an illustration of the domain and boundary conditions used is shown in Figure **4-4**.

4.1.3 Code used in this work

We studied the method of densities for topology optimization method with the 88-line code from [Andreassen et al., 2010]. In this code we used the method of moving asymptotes (MMA) algorithm for the optimization [Svanberg, 1998]. We adapted the code to work for the heat problem with the lines of code in [Bendsøe and Sigmund, 2004]. Further modifications used to test the code with alternative filters or density representation spaces were tested here. The repository for a short version of this code can be found in [Ortegón-Villacorte, 2023].

The GPTO method was studied with the code from [Smith and Norato, 2020] and modified

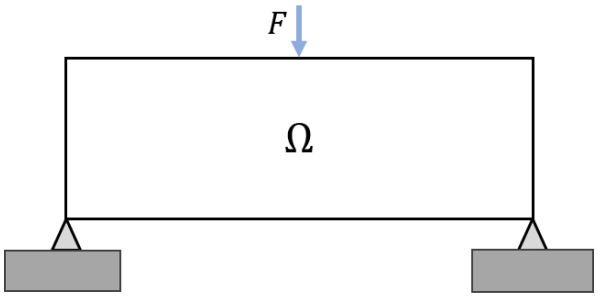

Figure 4-3: Michell bridge elasticity problem. This problem is used in [Zhang and Norato, 2018] to test the tunneling method in Chapter 5. It consists of a rectangular domain with a central force applied in the center of the top boundary and two constraints in the bottom corners in both horizontal and vertical directions. Here we use this problem too to test the tunneling method. The size of the domain is 150×50. As in the previous case, the traction in the subset Γ_2 of the boundary is $h(x) = 0$.

to work with the heat problem. Additionally, we implemented a Python version of the GPTO code to work with freely available numeric and plotting libraries. This version is available in [Ortegón-Villacorte, 2021].

4.1.4 Comparison of different numerical solutions

To compare two different methods we follow the recommendation in [Sigmund, 2022]. We *force* vectors ρ of the designs to consist only of 0 or 1 values in the components ρ_i by sorting the elements and mapping those elements with a higher density value to 1 until we complete the maximum fraction of material V_f^*. The remaining elements are mapped to 0 (and in turn to ε). We use this method to compare solutions to the original density problem and to the primitives method and between different projection functions.

4.2 Optimization

The relaxation of variables justified under the homogenization method allows for the use of an optimizer and the convergence to a local minimum that may be good enough for the considered application, as it will be seen later. However, depending on the problem, it is difficult to reach the global optimum, see for example [Yan et al., 2018]. Experiments also show that a simple change in initial conditions, move limit in the optimizer, tolerance, and many other simulation parameters is enough to obtain different numerical solutions, that is, different numerically valid local minima.

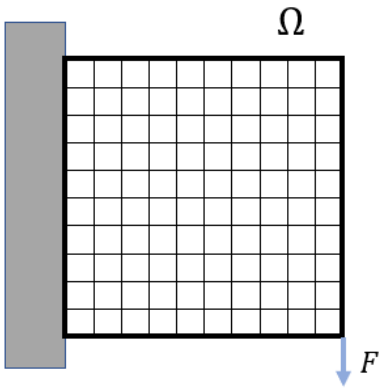

Figure 4-4: Cantilever 2D domain to test continuation paths, based on the domain in [Watada and Oshaki, 2009]. The experiment consists of a beam embedded on the left side with a force of 1.0 N at the lower right end and a fixed mesh of 10×10 elements with a size of 10×10.

It is also possible to experimentally verify that some attraction valleys can be very extensive and that there can be many local minima in small regions of the design domain, see Subsection 4.2.1 and 4.5.2. This situation is common also to the geometry projection method approach and it is more notorious when using the SIMP penalization (provided that the derivative of the compliance respect to an element e is always 0 for $p > 1$, see Subsection 4.2.1). This situation can be circumvented using alternative interpolation schemes or methods that progressively modify the objective function. More about this in Section 4.4 and Section 5.1.

When choosing an optimizer, it is possible to use an optimality criteria (OC) based algorithm or any gradient-based mathematical programming method able to handle large amounts of design variables. One of the most widely used algorithms is the Method of Moving Asymptotes (MMA). See [Bendsøe and Sigmund, 2004].

4.2.1 Gradient computation

To use a gradient-based optimization method, we must have an efficient method for computing derivatives of the objective function and constraint functions in the problem. The expression for the gradient is computed for the compliance problem using the adjoint method, see [Bendsøe and Sigmund, 2004]. The expression is the following

$$\frac{\partial c}{\partial \rho_e} = -u_e^T(\rho)\frac{\partial \boldsymbol{K}}{\partial \rho_e}u_e(\rho)\ . \tag{4-1}$$

Notice that this expression does not include the filter, but a filter like the one explained in

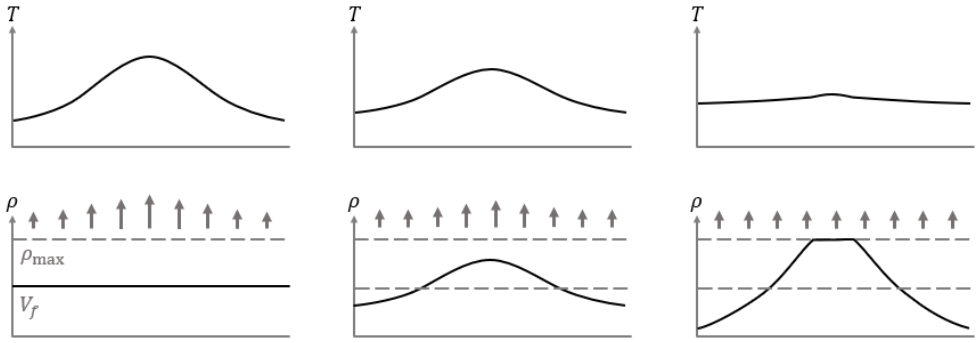

(a) The graphs in pairs represent the temperature T and the density ρ in three different moments of the optimization. Without penalization, the magnitude of the gradient of the compliance in the local density depends on the local temperature.

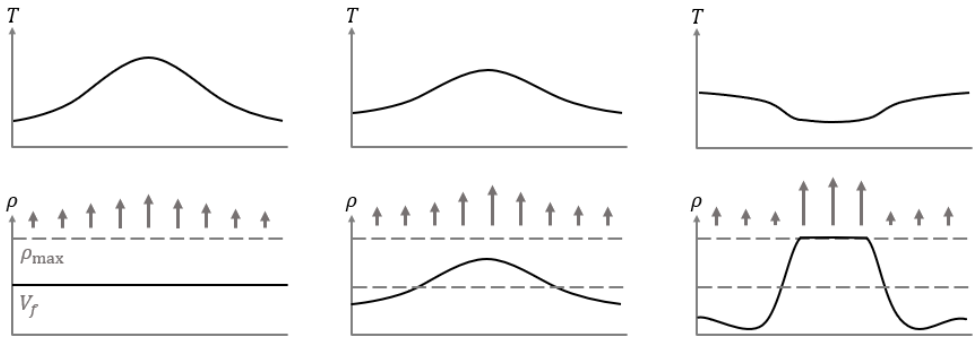

(b) With penalization, the magnitude of the gradient of the compliance in the local density depends on the local temperature and the local density.

Figure 4-5: Representation of the gradient influence (arrows) according to the temperature T and the density ρ with *(a)* and without penalization *(b)*. This representation is a simplification and it can ignore more complex effects in the optimization. Three distributions of material are shown for each case, representing an optimization process.

Chapter 3 is a linear mapping that can be applied directly to the derivative. Using equation (3-12) for the SIMP method we have

$$\frac{\partial c}{\partial \rho_e} = -p\rho^{(p-1)} u_e^T(\rho) \boldsymbol{K} u_e(\rho) \; . \tag{4-2}$$

In the case of three-field methods, where the density variables are dependent on a parameter, we can apply the chain rule. For example, in the case of the GPTO, we continue to differentiate with respect to each function until we differentiate the parameters of the primitives, see (4-3). Each density cell depends on the possible combination of primitives using a softmax function, see (4-4) below. The independent contributions of each primitive depend on the

projection function and the parameter α_b, as in (4-5).

$$\frac{\partial c}{\partial z_b} = \frac{\partial c}{\partial \rho_e}\frac{\partial \rho_e}{\partial z_b}\,, \tag{4-3}$$

$$= \frac{\partial c}{\partial \rho_e}\frac{\partial \rho_e}{\partial \tilde{\rho}_{be}}\frac{\partial \tilde{\rho}_{be}}{\partial z_b} = \frac{\partial c}{\partial \rho_e}\frac{\partial \max(\rho)}{\partial \rho_{be}}\frac{\partial \tilde{\rho}_{be}}{\partial z_b}\,, \tag{4-4}$$

$$= \frac{\partial c}{\partial \rho_e}\frac{\partial\ \mathrm{softmax}(\rho)}{\partial \tilde{\rho}_{be}}\frac{\partial \alpha_b h(z_b)}{\partial z_b} = \frac{\partial c}{\partial \rho_e}\frac{\partial\ \mathrm{softmax}(\rho)}{\partial \tilde{\rho}_{be}}\left(\alpha_b\frac{\partial h(z_b)}{\partial z_b} + h(z_b)\frac{\partial \alpha_b}{\partial z_b}\right)\,. \tag{4-5}$$

From there we get

$$h(z_b)\frac{\partial \alpha_b}{\partial z_b} = h(z_b)$$

and

$$\frac{\partial h(z_b)}{\partial z_b} = h'(z_b)\frac{\partial \phi(z_b)}{\partial z_b}\,.$$

Details on the derivative $\frac{\partial \phi(z_b)}{\partial z_b}$ are found in [Smith and Norato, 2020]. Before using the gradient in an optimization algorithm, we can analyse some properties using the gradient formula. For example, expression (4-1) tells us that the addition of material always decreases the gradient [Bendsøe and Sigmund, 2004] and that regions with higher temperature (or stress) increase the amount of material first. With a constraint on the amount of material, the material must be distributed according to the temperature and regions with higher temperatures will have preference. In subsequent optimization phases, the local addition of material decreases (or increases, depending on the boundary conditions) the local temperature (or stress). Given that the temperature is possibly lower in the area that has accumulated material first than in the rest of the domain, other regions with higher temperatures attract the remaining material. Without penalty, the optimizer finds the global minimum which generally has gray areas with average temperature and black areas (with pseudo-density 1) connected to the gray areas, see Figure **4-5**a.

The local accumulation of material is more pronounced when penalty ($p > 1$) is added, because the gradient is now also proportional to the term $n\rho_e^{(n-1)}$. With uniform initial conditions, this term has no influence since $\rho_e = V_f$ for every element Ω_e, then the gradient of the penalized functional is a multiple of the gradient of the non-penalized functional. However, once the material starts to concentrate in certain zones, a *feedback effect* occurs: zones more dense will attract more material until the local temperature decreases below the average temperature and probably the upper bound of material is reached. Then the remaining material forms new members away from the initial members, where the temperature has not decreased. The higher the material penalty, the more pronounced this effect, see Figure **4-5**b.

4.2.2 Method of moving asymptotes

The method of moving asymptotes (MMA) is a general-purpose gradient-based optimization algorithm presented originally in [Svanberg, 1987]. As described in the original paper, it is a method specially designed to handle structural optimization problems with inequality constraints, where the function evaluations could be expensive, but the gradient computation is available. Equality constraints can be handled by adding upper and lower inequality constraints differing by a small constant. Here we follow the more recent discussion of the method in [Svanberg, 1998] in terms of the design variable $\mathbf{x}$. Consider the general optimization problem stated next.

Problem 5 *Find* $\mathbf{x}^*$ *that solves*

$$\begin{aligned} \min_{\mathbf{x}} \quad & f_0(\mathbf{x})\,, \\ \textit{subject to} \quad & f_i(\mathbf{x}) \leq 0\,, \qquad i = 1, ..., N_c\,, \\ & x_{i-\min} \leq x_i \leq x_{i-\max}\,. \end{aligned} \tag{4-6}$$

Here x_i is the i-th component of vector $\mathbf{x}$, and N_c is the number of nonlinear constraints.

In MMA, local approximations of the objective and constraint functions are done around the point $\mathbf{x}^{(k-1)}$ in the time step k, in order to solve the Problem 6 stated next.

Problem 6 *Find* $\mathbf{x}^{(k)}$ *that solves*

$$\begin{aligned} \min_{\mathbf{x}^{(k)}} \quad & \tilde{f}_0(\mathbf{x}^{(k)})\,, \\ \textit{subject to} \quad & \tilde{f}_1(\mathbf{x}^{(k)}) \leq 0\,, \\ & \alpha_i \leq x_i \leq \beta_i\,. \end{aligned} \tag{4-7}$$

with

$$\tilde{f}_j(\mathbf{x}^{(k)}) = f_j(\mathbf{x}^{(k)}) + \sum_{i=1}^{N} \left(\frac{r_{ij}}{U_i - x_i} + \frac{s_{ij}}{x_i - L_i} \right) - \sum_{i=1}^{N} \left(\frac{r_{ij}}{U_i - x_i^{(k)}} + \frac{s_{ij}}{x_i^{(k)} - L_i} \right), \qquad j = 0, 1\,,$$

$$r_{ij} = (U_i - x_i^{(k)})^2 \left(\left(\frac{\partial}{\partial x_i} f_{ij}(\mathbf{x}^{(k)}) \right)^+ - k_{ij}^{(k)} \right), \qquad j = 0, 1\,,$$

$$s_{ij} = (x_i^{(k)} - L_i)^2 \left(\left(\frac{\partial}{\partial x_i} f_{ij}(\mathbf{x}^{(k)}) \right)^- - k_{ij}^{(k)} \right), \qquad j = 0, 1\,.$$

Here r_{ij} and s_{ij} activate the asymptotes L_i and U_i, which control the range of the approximation. The symbols $(z)^+$ and $(z)^-$ in the exponent of the derivatives indicate the positive and negative part of z, respectively, and we have

$$\begin{aligned} L_i &= x_i^{(k)} - \gamma_i^{(k)} (x_i^{(k-1)} - L_i^{(k-1)})\,, \\ U_i &= x_i^{(k)} + \gamma_i^{(k)} (U_i^{(k-1)} - x_i^{(k-1)})\,. \end{aligned}$$

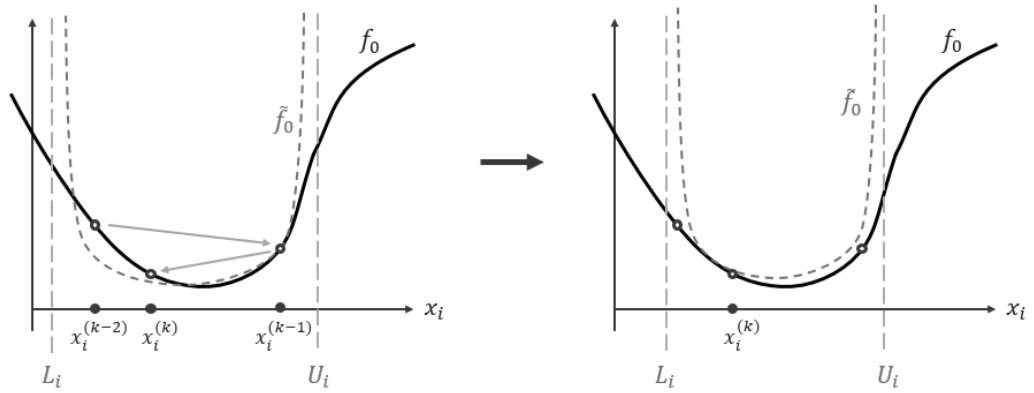

(a) The component of the step in direction x_i is too big and the variable returns between values. In the next step the distance between asymptotes is decreased.

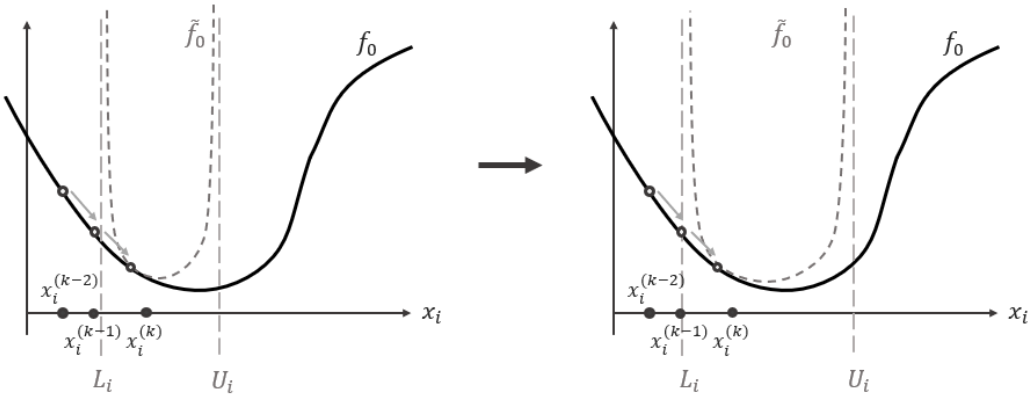

(b) The local approximation is too conservative in direction x_i and the optimizer makes small steps in the same direction. Then the distance between asymptotes is increased.

Figure 4-6: Influence of factor γ_i in the optimization. Illustration of the first two cases of equation (4-8) done by us.

In the local approximation to the problem, an asymptote is introduced for each component of the vector $\mathbf{x}$ in the objective function and the constraint functions. The asymptote is updated based on the distance to the previous point and the factor

$$\gamma_i^{(k)} = \begin{cases} 0.7 & , \quad (x_i^{(k)} - x_i^{(k-1)})(x_i^{(k-1)} - x_i^{(k-2)}) < 0\,, \\ 1.2 & , \quad (x_i^{(k)} - x_i^{(k-1)})(x_i^{(k-1)} - x_i^{(k-2)}) > 0\,, \\ 1 & , \quad (x_i^{(k)} - x_i^{(k-1)})(x_i^{(k-1)} - x_i^{(k-2)}) = 0\,. \end{cases} \tag{4-8}$$

The factor decreases for a negative angle in the last two iterations (this means that in the component the function describes a zig-zag), Figure **4-6**a. Similarly, the factor grows when the step of the previous two iterations has the same direction, meaning that the distance between asymptotes grows **4-6**b. When there is no change in the component x_i in one of the

previous two steps, then the factor γ_i stays the same. In the optimization step, the limits of the variable used are the following

$$\alpha_i = \max\left\{x_{\min},\, 0.9L_i + 0.1x_i^{(k)}\right\},$$
$$\beta_i = \min\left\{x_{\max},\, 0.9U_i + 0.1x_i^{(k)}\right\}.$$

Based on the approximation, we follow these steps, see [Svanberg, 1998]:

- **Direction**: The optimization problem is expressed in terms of Lagrange multipliers. The active constraints are represented by a partial derivative equal to zero. This constraint is relaxed by equaling the partial derivative to a small negative parameter ε. Then a Newton direction is found by solving a system of linear equations, [Svanberg, 1998].
- **Updating**: Then the vector is updated to the new values.
- **Parameter updating**: The parameter ε can be also updated, reducing its absolute value until some tolerance is satisfied.

The method is efficient and needs only the gradient of the function and nowadays it is one of the preferred optimization algorithms for TO. See [Bendsøe and Sigmund, 2004]. A line search and other small modifications are added after the Direction search in the globally convergent version of the MMA (GCMMA), see [Svanberg, 1998]. This method is also suitable to treat the GPTO method and will be used in the simulations.

4.3 Numerical experiments

In this section, we present basic numerical results for Problem 4, of the heat problem and the elasticity problem with the original method of densities and the GPTO. We use the experiments to compare the results with and without penalization and perform small modifications to the conditions to point out phenomena we consider relevant for the discussion.

4.3.1 Area-to-point problem

Let us consider the benchmark heat diffusion problem presented in Section 4.1. The solution to the non-penalized problem and for the penalized problem with a small radius in the filter is shown in Figures **4-7**a and **4-7**b. The initial conditions are described as *uniform*, which means the starting density for every element is the maximum volume proportion $\rho_i = V_f^*$.
In the non-penalized solution, we can see a smooth distribution of material that diminishes away from the heat sink, see Figure **4-7**a. Close to the sink, a bulk of full-density material connects with the grey region. It is possible to see that tracing rays from the sink to the

(a) Area-to-point problem without penalization, $p = 1$.
Compliance $c/c_0 = 1.000$

(b) Area-to-point problem with penalization, , $p = 3$ and without continuation.
Compliance $c/c_0 = 1.161$

Figure 4-7: Basic solutions to the area-to-point problem with and without penalization in a Q_0 representation. Simulation parameters in Table **4-1**.

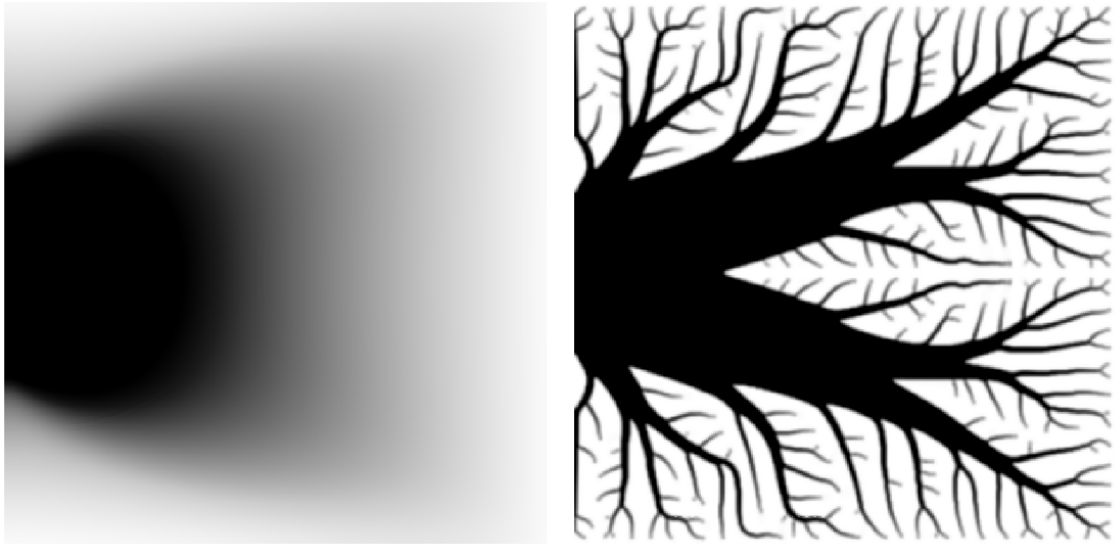

(a) Solution without penalization, $p = 1$.
Compliance $c/c_0 = 1.000$

(b) Penalization $p = 3$ and no continuation.
Compliance $c/c_0 = 1.186$

Figure 4-8: Solutions of the area-to-point problem with and without penalization for the DQ1 space representation of densities. Simulation parameters in Table **4-1**.

Problem	Heat	**Mesh size**	300x300
Opt. algorithm	MMA	**Move limit**	0.2
Initial point	Uniform	**Stop criterium**	Rel. Ch. 10^{-5}
Interpolation	SIMP	**Penal. factor**	$p = 1, 3$
Filtering	Densities	**Filter Radius**	2
Linear solver	Default	**Volume fraction**	0.45
E_{min}/E_0	10^{-3}		

Table 4-1: Simulation parameters for the area-to-point experiments in Figures **4-7** and **4-19**. We use these parameters from now on to compare modifications of the method through Chapters 4 and 5.

boundary, the longer rays are where a higher density of material accumulates, particularly in the directions of the corner of the domain. In the penalized solution with filtering, the mentioned rays accumulate material forming big branches pointing towards the opposite corners, as predicted from the gradient expression (4-2). From bigger branches, smaller ones detach seemingly random, filling close regions to cover almost uniformly the entire domain. The value of the compliance is normalized based on the compliance of the global solution without penalization c_0, since we know this is the minimum attainable value for compliance for a given volume proportion. Additional simulations were performed with the alternative representation space DQ1. There are no significant differences in the non-penalized solution for the Q_0 representation. The penalized solution has a similar disposition of material to the original Q_0 representation, but due to numerical differences of the problem, even with the same simulation parameters, the solutions converge to different distributions of material. The results for the method of densities and the method of primitives suggest that a method that can keep a local amount of material similar to the non-penalized solution and in the case of the GPTO methods, if all members align towards the sink could have improved compliance, see [Yan et al., 2018]. Based on this we follow the discussion in Section 4.5.

Problem	Heat	**Mesh size**	300x300
Opt. algorithm	MMA	**Move limit**	0.1
Initial point	Uniform	**Stopping criteria**	Variable change 10^{-3}. Max. 200 Iterations.
Interpolation	RAMP	**Penalization factor**	p = 3
Linear solver	Default	**Volume fraction**	0.40
Bar radius	Fixed	**Projection**	Arccos function
E_{min}/E_0	10^{-2}		

Table 4-2: Simulation parameters for the area-to-point heat problem with the GPTO method in experiments presented in Figures **4-9** and **4-19**.

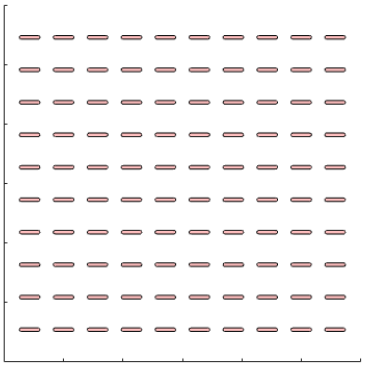

(a) Initial conditions. Bar radius $r = 1.5$.

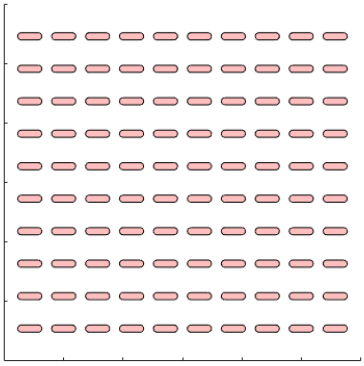

(b) Initial conditions. Bar radius $r = 3.0$

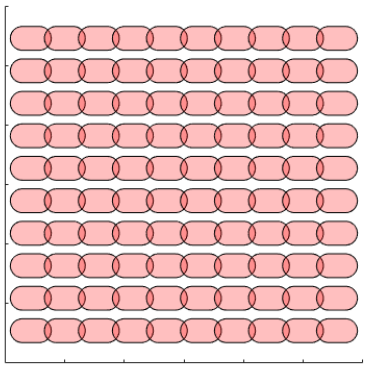

(c) Initial conditions. Bar radius $r = 10.0$.

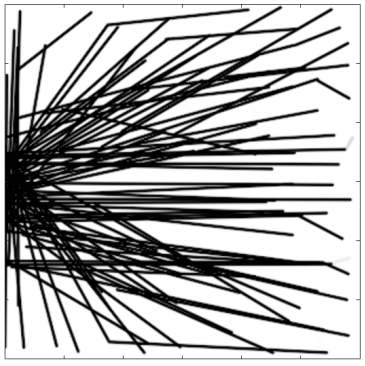

(d) Final result (200 iterations). Compliance $c/c_0 = 1.276$ (1.226)

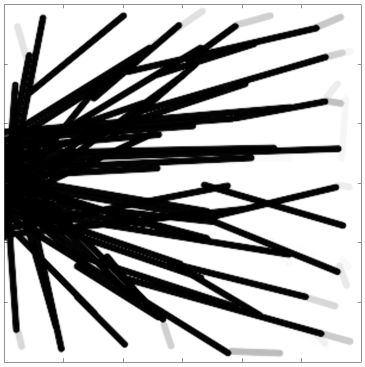

(e) Final result (200 iterations). Compliance $c/c_0 = 1.426$ (1.122)

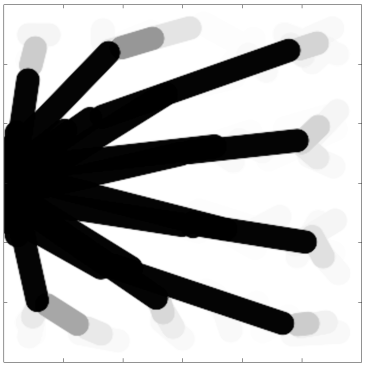

(f) Final result (200 iterations). Compliance $c/c_0 = 2.521$ (1.158)

Figure 4-9: Solutions to the area-to-point problem with GPTO. Simulation parameters in Table **4-2**. Two values of compliance are presented, the 0-1 design value and between parenthesis the value of the compliance with gray elements.

Solutions with a modified implementation of the code of the method of primitives from [Smith and Norato, 2020] for the heat problem is shown in Figure **4-9**. In the figure, we can see 3 simulations with different fixed bar radii, 1.5, 3.0, and 10.0, in a 300×300 mesh. The initial condition is chosen as a uniform distribution of 100 bars in the domain with a size of 0.5 for each bar. The 1.5 radius was chosen to represent a similar minimum length scale to the 2.0 radius filter in the density method. It is possible to see that most of the bars align towards the sink, but several bars cross other bars and in general, the amount of material near the sink is deficient. This last situation does not happen with a bigger radius, but crossed bars are still present and intermediate size (density) bars appear in the regions far from the sink. as the members' width can not be satisfied by the bar radius.

4.3.2 Half-MBB problem

(a) No penalization $p = 1$. Compliance $c_0/c_0 = 1.000$.

(b) With penalization $p = 3$. Compliance $c/c_0 = 1.106$.

Figure 4-10: Optimization of the half-MBB beam. Simulation parameters in Table **4-3**.

Problem	Elasticity	**Mesh size**	200×50
Opt. algorithm	MMA	**Move limit**	0.20
Initial point	Uniform	**Stopping criteria**	Variable change 10^{-3}. Max. 200 Iterations.
Interpolation	SIMP	**Penalization factor**	-
Filtering	Densities	**Filter radius**	2
Linear solver	Default	**Volume fraction**	0.45
E_{min}/E_0	10^{-9}	ν	0.3

Table 4-3: Simulation parameters for half-MBB beam experiments presented in Figures **4-10** and **4-17**.

(a) Initial conditions.

(b) Final result. Compliance $c/c_0 = 1.180$

Figure 4-11: GPTO method applied to the half-MBB beam problem. The problem setting was adjusted from the examples found in [Smith and Norato, 2020]. See Table **4-4** for the simulation parameters.

Next, we will focus our discussion on the Half-MBB beam shown in Figure **4-10**. Regarding this problem, the non-penalized global optimum, presented in Figure **4-10**a, exhibits two zones with a significant amount of black material located at the top and bottom of the domain. In the central part of the domain, there exists an intermediate density zone where new full-density members are expected to appear with penalization, as previously discussed. Additionally, there is a connecting zone of high density on the right side of the domain,

which resembles a curved member but is not entirely dense. Figure **4-10**b presents a solution with the same parameters as the non-penalized solution, but with a penalization factor of $p = 3$. In this penalized solution, the two bulks of material described in Figure **4-10**a remain present, and internal members have formed to replace the gray zone as expected, similar to the heat problem. One major difference here is that, in the elasticity problem, straight members are preferred (this makes physical sense, as mentioned in [Sigmund, 2022]). Figure **4-11** illustrates the solution for a fixed bar radius of the same problem in the GPTO method. The bulks of material described earlier are formed by overlapping members, and a random disposition of members in the center is reminiscent of the solution obtained using the method of densities. The overall performance of the design is hampered by a reduced number of degrees of freedom in the optimization process. However, the design features members with similar width, which may be preferred by the designer depending on the application. Figure **4-11**b depicts the last design, where partially sized elements in gray are located on the right side instead of the expected curved boundary. This is due to the limitations of the GPTO method with bar primitives to represent complex geometries. This is attributed to the limitations of the GPTO method with bar primitives in representing complex geometries.

4.4 Methods with progressive change in the cost functional

The objective function can present non-convex directions and is possible to fall in an attraction valley leading to a non-satisfactory distribution of material, see [Yan et al., 2018]. There are several strategies to improve solutions to TO problems. In this section, we present particularly the continuation method in TO and another possible method based on the modification of the filters, we discuss ideas from [Bendsøe and Sigmund, 2004].

Problem	Elasticity	**Mesh size**	200×50 Max. 200 Iterations.
Opt. algorithm	MMA	**Move limit**	0.1
Initial point	In **4-11**a	**Stopping criteria**	Variable change 10^{-3}.
Interpolation	SIMP	**Penalization factor**	p = 3
Bar radius	2.0 fixed	**Linear solver**	Default
Volume fraction	0.45	**Projection**	Arccos function
E_{min}/E_0	10^{-3}	ν	0.3

Table 4-4: Simulation parameters for the Half-MBB beam problem with the GPTO method in the experiment presented in Figure **4-11**.

4.4.1 Continuation

In the continuation strategy the parameter of the interpolation scheme changes in a progressive way starting from some initial value p_0 (for example, no penalization). Then, the parameter moves towards p_f usually in a linear manner. For instance, in Problem 4 starting from iteration $k = 0$, the problem on each subsequent iteration has a different form described by

$$\sum_{i=1}^{N} \rho_i^{p(k)} \boldsymbol{K}_i \boldsymbol{u} = \boldsymbol{f} \,, \tag{4-9}$$

$$p(i) = p_0 + (p_f - p_0)\frac{k}{I} \,. \tag{4-10}$$

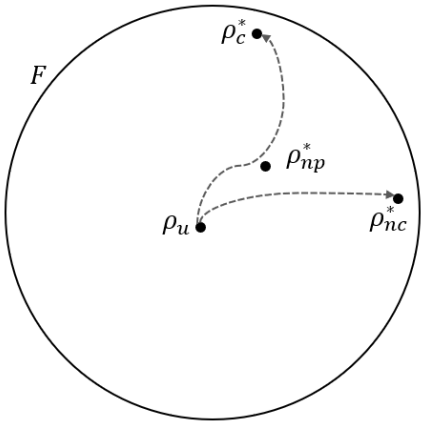

Figure 4-12: Schematic of the effect of the continuation in the trajectory of the optimization. In a feasible set F the optimization has initial conditions ρ_u and converges without continuation to the optimal point ρ_{nc}^*, describing the trajectory represented by the curved arrow. If continuation is used, the optimization converges to the point ρ_c^*, passing *closer* to the non-penalized solution ρ_{np}^* than the trajectory without continuation.

Here I is the maximum number of iterations where the continuation parameter is allowed to change, for example, $I = 100$. Once the maximum parameter value p_f is reached, the optimization can continue as described in Problem 4. The same modification in the exponent in (4-9) can be used to modify the parameter of interpolation schemes like RAMP in (3-18). In such cases (4-10) is not modified. The continuation approach can avoid strong local minima that accumulate material in the first steps of the optimization process, see [Yan et al., 2018]. This modification is highly effective for improving the quality of the numerical solution, for instance, in the area-to-point problem as shown in Figures **4-13**a and **4-13**b, although sometimes a global optimum cannot be reached through the continuation trajectory, see [Stolpe and Svanberg, 2001] and Subsection 4.5.2. Adding a continuation

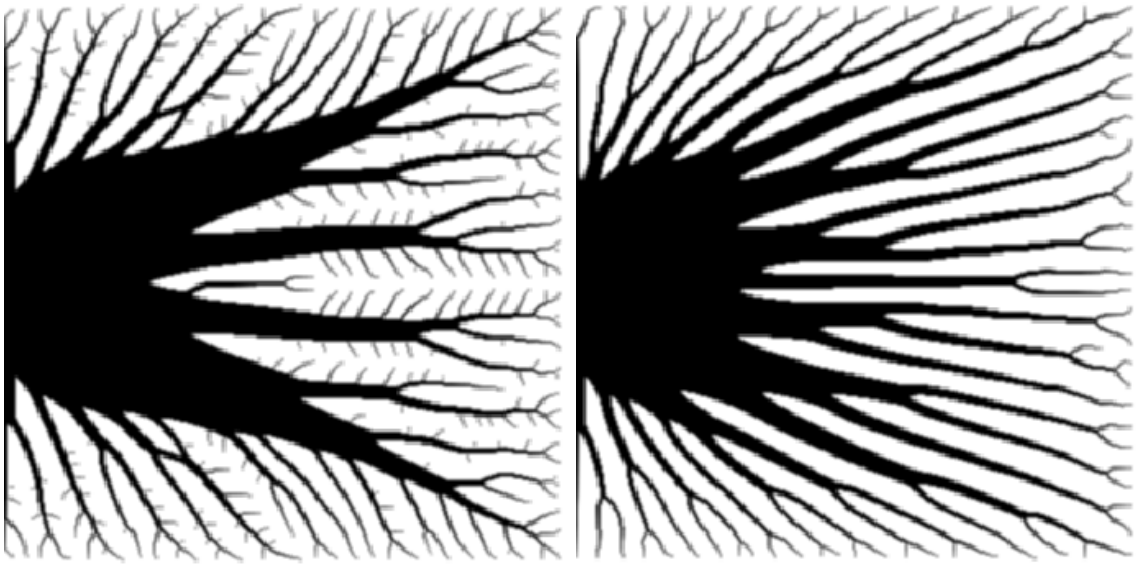

(a) Continuation step 0.02. Compliance $c/c_0 = 1.137$

(b) Continuation step 0.002. Compliance $c/c_0 = 1.106$

Figure 4-13: Area-to-point heat problem with continuation, simulation parameters in **4-1**. The progressive penalization improves the distribution of material and the overall compliance of the structure.

strategy in the optimization constrains the optimizer the stay close to the optimum in the non-penalized solution during the first steps of the optimization, see Figure **4-12**. This effect leads the optimizer to local minima with local distributions of material more similar to the non-penalized solution; more on this in Chapter 5. In Figure **4-13**b, we can see that random branches departing from bigger ones have mostly disappeared with this strategy. In [Yan et al., 2018] the authors prove that without an imposed minimum scale, the optimal theoretical solution corresponds to infinitesimally small needles mimicking the material distribution of non-penalized functional of the compliance problem (problem 2) pointing towards the sink of the domain. A minimum length scale is imposed due to mesh size or the use of a filter, then we can expect that as we refine the mesh a higher number of members appear close to optimal solutions. In Figure **4-14** we observe the effect of the continuation strategy with the DQ_1 representation. We observe that there is a clear improvement in performance with the continuation method but not as good as in the Q_0 representation. Large members that accumulate material are still dominant for this representation.

We can apply also the method of continuation to the elasticity problems, for instance, the half-MBB beam in Figure **4-15**. At the beginning of the optimization, the distribution of material mimics the distribution of the non-penalized solution, Figure **4-10**a, with thin and numerous members, similar to the situation of the area-to-point problem in Figure **4-13**. However, due to linear filtering, which produces boundaries with gray transitions, thin

(a) Penalization $p = 3$. Continuation step 0.02. Compliance $c/c_0 = 1.166$.

(b) Penalization $p = 3$. Continuation step 0.002. Compliance $c/c_0 = 1.138$.

(c) Penalization $p = 3$. Continuation step 0.001. Compliance $c/c_0 = 1.130$.

Figure 4-14: Continuation solutions to the area-to-point problem with DQ1 representation. Compared to the Q_0 representation the performance is worse with and without continuation.

(a) Step 50 of the optimization process

(b) Final result. Compliance $c/c_0 = 1.111$.

Figure 4-15: Half-MBB beam optimization with continuation, step of (0.02) applied as in formula (4-9). Simulation parameters are kept as in Table **4-3**. Here is one design in the first steps of the optimization (a) and then the final result (b).

members are expensive and disappear progressively with the increasing penalization. The final result is similar to designs without continuation, as in Figure **4-10**b, and sometimes there is no gain in performance of the design. Notice that the members in intermediate steps of the optimization process resemble the analytical solution with infinitesimally thin members for the elasticity problem presented in [Rozvany, 1998].

4.4.2 Filtering

Experiments show that the representation of members of the structure in a mesh can generate local minima, depending also in the penalization strategy, see [van Dijk et al., 2010, Wein et al., 2020]. Filtering can modify this local minimum in such a way that is possible to find the best position for the members with a wider filter. However, these strongly filtered designs are not useful as they consist mostly of grey regions of material. Combining these two

(a) Result of the first phase with $r = 5$. Compliance $c/c_0 = 1.140$

(b) Final result with radius $r = 2$. Compliance $c/c_0 = 1.114$.

Figure 4-16: A single optimization with two phases, first an optimization with a radius $r = 5$ is performed. Then a second optimization with the local minima as the initial condition is performed with a smaller radius $r = 2$. The use of a wider radius imposes a larger minimum scale. Other simulation parameters are kept as in Table **4-3**.

observations, it is possible to propose a strategy where we start a minimization with a wide filter and then diminish the radius to obtain an improved design, as presented in Figure **4-16**. This method would impose a larger minimum scale on the design, then we expect wider members and a smaller number of them. A strategy similar to the one implemented in Figure **4-16** is proposed in [Bendsøe and Sigmund, 2004]. We do not implement this strategy with the area-to-point problem because this strategy directly affects the minimum length scale and we are trying to improve the layout of thin members in that problem, in other words, we expect big members with the strategy and that opposes our objective with the problem.

In the MBB beam problem, we can see that the final compliance value for the two-phase filtering strategy is slightly worse than the values of compliance of simple experiments like the initial half-MBB in Figure **4-10**. We think that this difference is due to the higher number of degrees of freedom of the smaller length scale in the 1-step filtering experiments. However we must point out that the values of compliance with a higher number of members are not better when the design is not forced to be 0-1, but computed only with a linear filter. In such cases, a higher number of members means a longer blurry boundary (higher number of gray elements) and a lower stiffness in general due to the penalization of intermediate densities.

4.5 Local minima

Most of the time, an optimization procedure is able to deliver a reasonable design in a sub-optimal point, see [Bendsøe and Sigmund, 2004] and the example in Figure **4-22**. In some problems, using modified and computationally intensive approaches, it is possible to obtain a solution even closer to a possible global optimum. However, due to the high number of local optima, these solutions may not represent significant improvements with respect to the

solutions obtained in a reasonable time. For this reason, it is common to use sub-optimal solutions. In this section, we explore factors that affect the local minima in elasticity and heat problems and their dependence on simulation parameters.

4.5.1 Effect of the initial conditions

We test the effect of the initial conditions in the half-MBB problem with a simple experiment: we use slightly perturbed uniform initial conditions in the optimization process as shown in Figure **4-17**a but with the same parameters of experiment **4-10**b, and we do not use continuation. The small square of full material (affected by the filter) is located where gray zones are usually found. Note that the variables corresponding to the small square are included in the optimization. This means the optimizer can eliminate these cells of the material if it is convenient. The final result shows that the chunk of black material remains in the final design inside a connecting member, and this affects the overall distribution of the material in the domain.

(a) Initial conditions.

(b) Final result. Compliance $c/c_0 = 1.104$

Figure 4-17: A simulation with a small perturbation in the initial conditions (a) renders a completely different design (b), from the final result in Figure **4-10**b. The initial conditions were adjusted to satisfy the volume fraction constraint. Simulation parameters in Table **4-3**.

Problem	Heat	**Mesh size**	300x300
Opt. algorithm	MMA	**Move limit**	0.01
Initial point	Figure **4-19**a	**Stopping criteria**	Variable change 10^{-3}. Max. 200 Iterations.
Interpolation	RAMP	**Penalization factor**	p = 3
Linear solver	Default	**Volume fraction**	0.40
Bar radius	1.5 fixed	**Projection**	Arccos function
E_{min}/E_0	10^{-2}		

Table 4-5: Simulation parameters for the area-to-point heat problem with the GPTO method in experiments presented in Figure **4-19**.

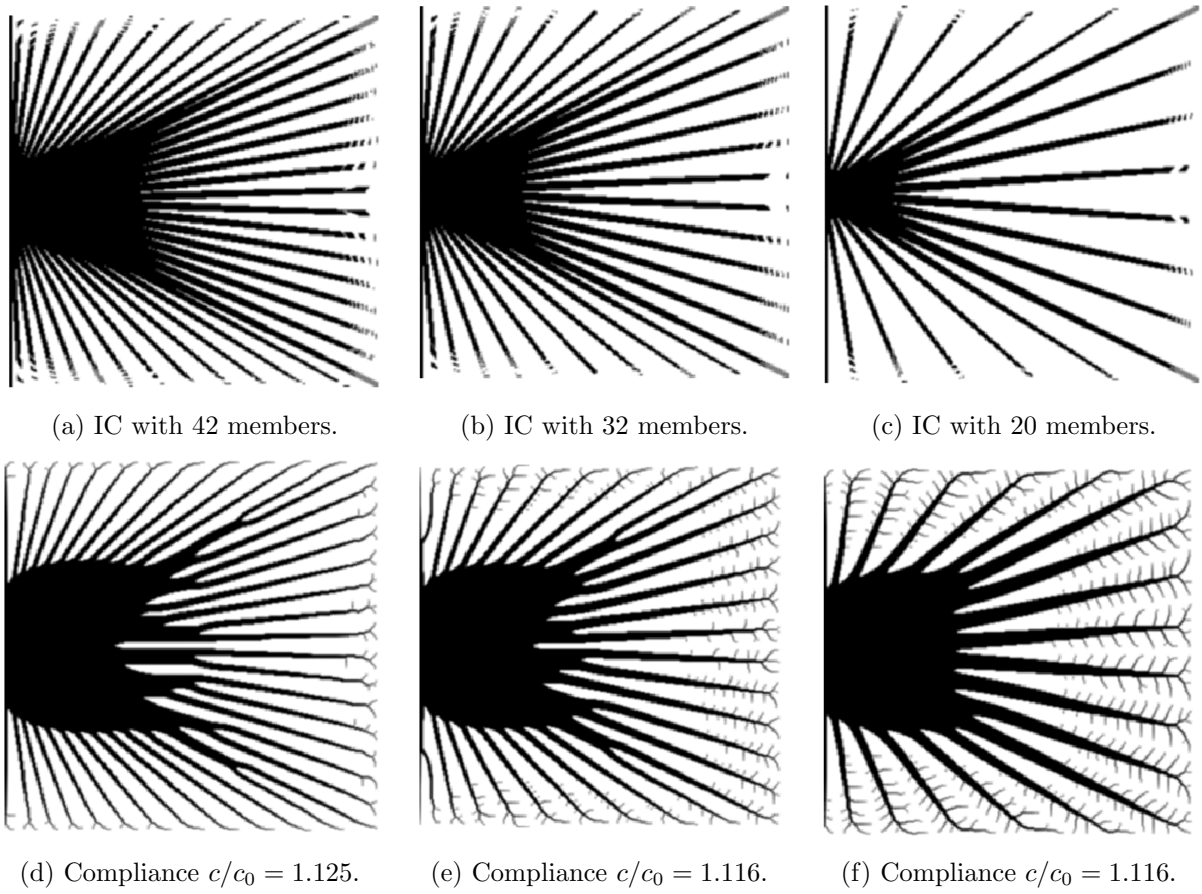

(a) IC with 42 members. (b) IC with 32 members. (c) IC with 20 members.

(d) Compliance $c/c_0 = 1.125$. (e) Compliance $c/c_0 = 1.116$. (f) Compliance $c/c_0 = 1.116$.

Figure 4-18: Area-to-point problem with manufactured initial conditions. The initial conditions were chosen as members pointing towards the center of the sink. Due to the penalization and the strong attraction valleys, the final solutions maintain the members of the initial conditions but fill vacant spaces with small branches of material. The simulation parameters are the same in Table **4-1**, except for the initial conditions.

The result of the modification of the initial conditions in the previous experiment matches the observations about the gradient in Subsection 4.2.1. This effect could be used, for example, to manufacture solutions for the area-to-point problem. Knowing that the final design should resemble needles pointing in the direction of the sink, one could insert nails as initial conditions to the optimizer and then let the problem run without continuation as in Figure **4-18**. This strategy is used in [Yan et al., 2018] to study the optimal points of the heat problem. Different amounts of nails can deliver different thermal compliance values but the number and position of members are almost not modified in the optimization process. Similarly, this can be used to place the initial positions of the bars for the GPTO method to obtain a design with bars pointing towards the sink, see Figure **4-19**. The final result shows that orientation towards the sink is indeed the preferred direction, and only the opposite

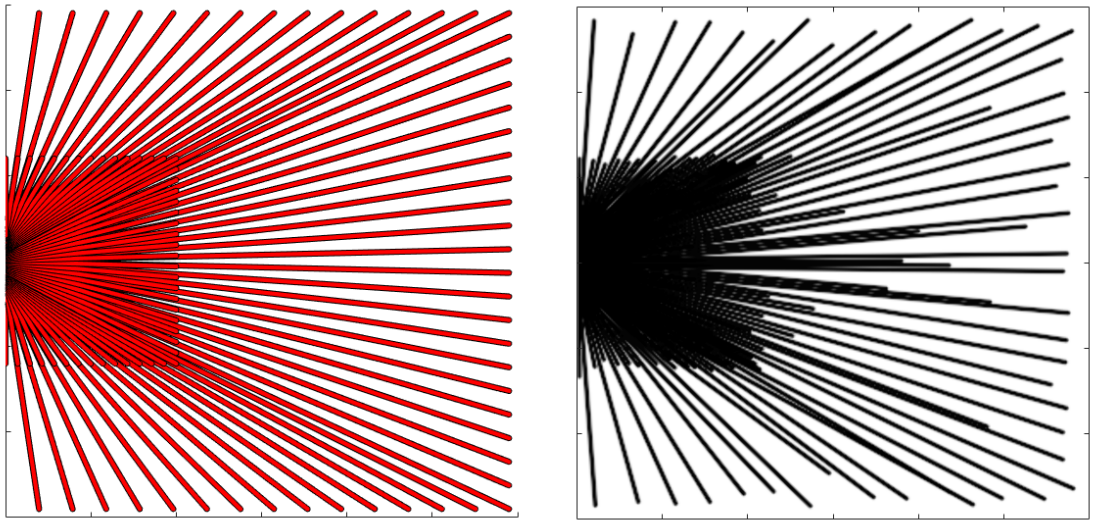

(a) Initial conditions. (b) Final result. Compliance $c/c_0 = 1.211(1.130)$

Figure 4-19: Area-to-point problem optimization with the GPTO method for fixed radius bars of 1.5 with initial conditions adjusted with bars pointing towards the sink in two groups: one composed of short bars and one of long bars. Simulation parameters in Table **4-5**.

endpoint changes, adjusting according to the proportion of material in this zone. Almost no overlapping far from the sink occurs and most of the bars of short length keep their position filling the gaps between long bars as the last ones increase their distance away from the sink, see Figure **4-19**b. Finally, we use the mapped densities in this design with bars as initial conditions for the optimization with the method of densities, using the parameters of Table **4-1**, whose results are presented in Figure **4-20**. We observe that some bars have merged close to the sink, the bulk of material close to the sink has acquired a rounded appearance and some small branches detach from the endpoints of the bars. The final compliance value is better than all the other experiments with special initial conditions and from the value with a simple continuation; however, it does not have a better value than the slow continuation approach.

4.5.2 Solutions with continuation

We mentioned previously that the non-penalized problem is convex and it has a global minimum. Once penalization is applied, it is possible to find a great number of local minima with similar details of material or similar objective function values. It makes sense to think that in continuation the minima appear progressively as penalization is increased. In [Watada and Oshaki, 2009] the authors study a simple linear elasticity problem in a 10×10 mesh, shown in Figure **4-4**. In their work, they demonstrate that some locally optimal solutions

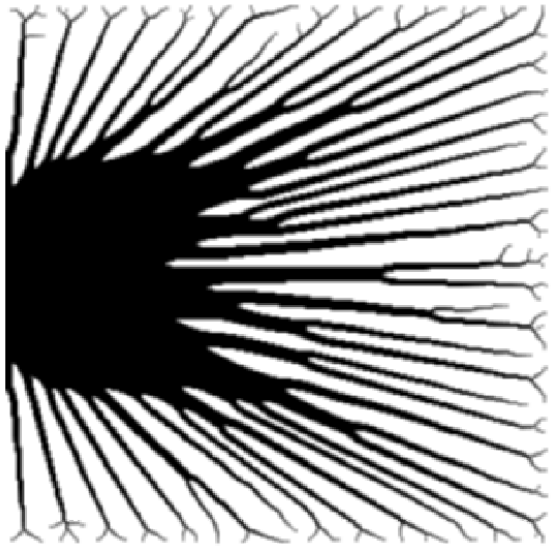

Figure 4-20: Final result of an optimization with the method of densities using as initial conditions the final result of optimization in Figure **4-19**. Compliance $c/c_0 = 1.111$

follow a path *in a continuation sense*; we explain this next. Recall Problem 4, but now as a variational problem in terms of the vector function $\rho(p)$ and p as a variable. We consider then the following problem.

Problem 7 *Find a function*

$$\begin{aligned} \boldsymbol{\rho}(p) : [p_0, p_f] &\to Q_0 \\ p &\mapsto \boldsymbol{\rho}(p) \end{aligned}$$

Here $\boldsymbol{\rho}$ represents an optimal distribution of material for the parameter p, and p_0 and p_f correspond to the parameters in (4-9) *and* (4-10)*. Function $\boldsymbol{\rho}$ solves a minimization problem for each p with the vector of temperature (or displacement) $\boldsymbol{u}$ and the load vector $\boldsymbol{f}$.*

$$\begin{aligned} \min_{\boldsymbol{\rho}(p)} \quad & \boldsymbol{u}^T(\boldsymbol{\rho}(p))\boldsymbol{f}\,, \\ \textit{subject to} \quad & \frac{1}{N}\sum_{i=1}^{N}\rho_i \le V_f^*\,, \\ & 0 < \rho_{min} \le \rho_i \le 1\,. \end{aligned} \tag{4-11}$$

Here V_f^* is a maximum fraction of material in the domain. Vectors $\boldsymbol{u}$ and $\boldsymbol{f}$ must satisfy the additional restriction

$$\boldsymbol{K}(\rho)\boldsymbol{u} = \sum_{e=1}^{N} E_p\left(\rho_e^p\right)\boldsymbol{K}_{0,e}\boldsymbol{u} = \boldsymbol{f}\,. \tag{4-12}$$

Here $E_p(\rho^p)$ is chosen as in (3-13)*.*

The question that the authors in [Watada and Oshaki, 2009] studied experimentally and partially with some theoretical results, is whether such functions $\boldsymbol{\rho}(p)$, which can be understood as paths, exist in optimization problems when the continuation formula (4-9) is applied. They found that sometimes these paths exist from the starting value p_0 to p_f, including the case when p_0 corresponds to a value for a non-penalized functional. There were additional observations in [Watada and Oshaki, 2009], for example, that paths can bifurcate at some point, indicating a singularity of the Jacobian of the functional and the existence of paths to multiple local minima. Additionally, not every path is connected to the starting point p_0 and some appear from a non-connected point at some problem-specific point in the continuation. The theoretical solution of Problem 7 is beyond the scope of this work.

Problem	Elasticity	**Mesh size**	10×10
Opt. algorithm	MMA	**Move limit**	0.20
Initial point	Random	**Stopping criteria**	Relative change 10^{-7}. Max. 200 Iterations.
Interpolation	SIMP	**Penalization factor**	$\{1, 3\}$
Filtering	Densities	**Filter radius**	1.25
Linear solver	Default	**Volume fraction**	0.40
E_{min}/E_0	10^{-9}	ν	0.3

Table 4-6: Simulation parameters for the cantilever experiments presented in Figures **4-21** and **4-23**.

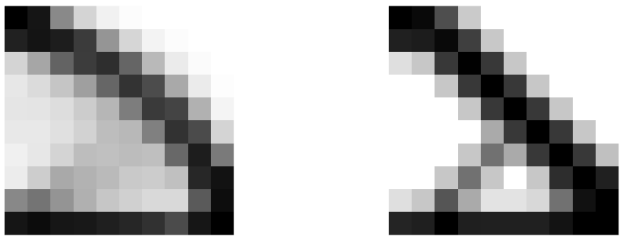

(a) No penalization $p = 1.0$ (b) Penalization$p = 3$

Figure 4-21: Basic solutions of the 2D-cantilever problem in a 10×10 mesh. Solution (b) was obtained with continuation.

We replicated the experiment in [Watada and Oshaki, 2009] in order to study the local minima for the 2D-cantilever problem in a mesh of size 10×10, see Figure **4-4**. The conditions mentioned in [Watada and Oshaki, 2009] are not exactly the same as those used in this document, considering that in this document a linear filter is used. Nevertheless, simulation parameters were used to give a similar qualitative result, see Table **4-6**. The

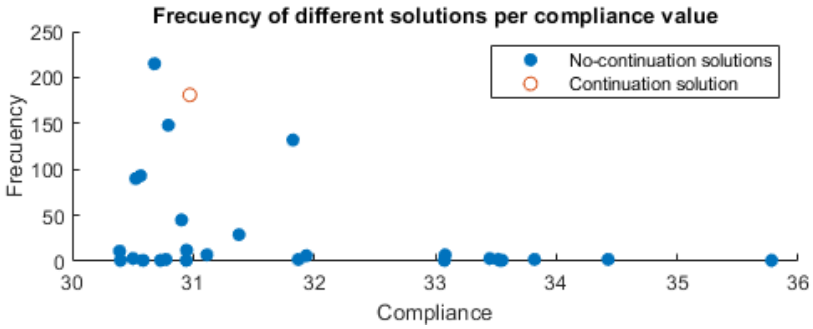

Figure 4-22: Frequency of each different solution vs compliance of the solution in a 1000 randomly started optimization processes for the 2D-cantilever, discriminating different solutions by criterion (4-13). The continuation solution delivers a comparatively good design, but other random solutions attain better values with higher frequency.

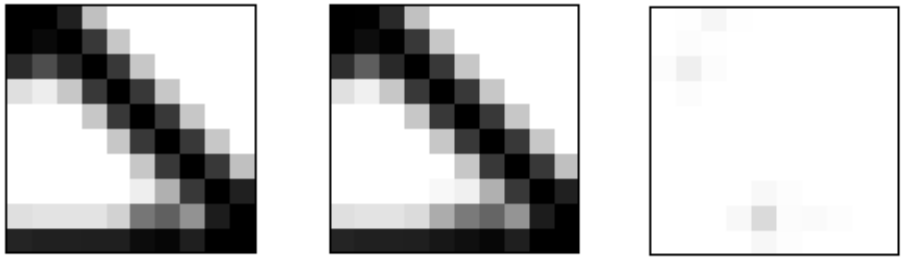

(a) Optimum ρ_1^* (b) Optimum ρ_2^* (c) $|\rho_1^* - \rho_2^*|$

Figure 4-23: Two best local minima ρ_1^* and ρ_2^* in the 2D-cantilever elasticity problem. Visually both solutions are almost identical. Their absolute difference is shown in (c). These two solutions are not connected by a gradient descending path.

solutions without penalization and penalization with continuation of 100 steps are shown in Figure **4-21**. We can see in Figure **4-21**b that the continuation minimum is similar to the solution without penalty. Then, we generated 100 different initial conditions, using the values of a uniform probability distribution as starting density value for each cell in each experiment. With continuation, all initial conditions deliver the same minimum; without continuation, 12 distinct local minima were found using the same criterion as in [Watada and Oshaki, 2009], i.e., two local minima ρ_i^* and ρ_j^* are considered to be equivalent if

$$\|\rho_i^* - \rho_j^*\|_\infty < 0.1 \,, \qquad i \neq j \,. \tag{4-13}$$

With this criterion, in [Watada and Oshaki, 2009] about 38 local minima are found. We attribute the difference to the difference in the procedures for filtering in the experiments. We generated then 1000 different initial conditions and found 28 different local minima. Figure **4-22** presents the frequency of different solutions vs the compliance value of each solution.

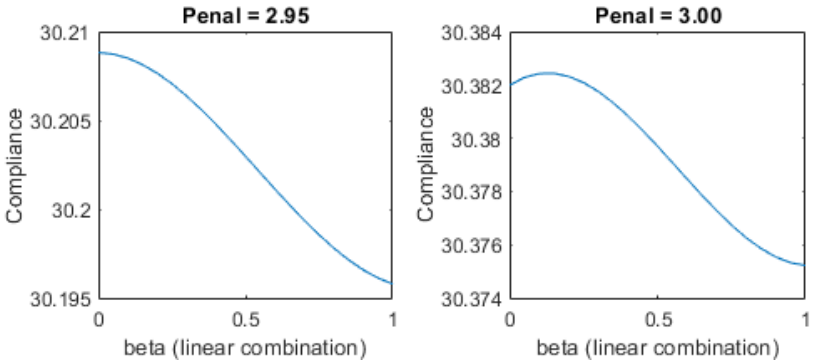

Figure 4-24: Graphs of the functional obtained by applying a convex combination of the two best optimal points ρ_1^* and ρ_2^* for the 2D-cantilever problem. We use two different values for the penalization parameter of the SIMP scheme in the construction of the two graphs. With a lower penalization $p = 2.95$ the two points are connected by a gradient descending direction, but with $p = 3.00$ the two points are disconnected. It is possible to see that the disconnection by a gradient path occurs close to $p = 3$.

Notice that we did not force the designs to have only 0-1 values. Figure **4-22** shows that numerical solutions with compliance similar to the global optimum are found with high frequency. In Figure **4-23** the best two local minima are shown with the *absolute difference* between the solutions on the right. This difference is small, $\max(|\rho_1^* - \rho_2^*|) = 0.150$. A natural question is whether these two minima are the same but due to the numerical tolerance of the convergence criterion they seem different, or one of the minima has converged to a saddle point. For the analysis we consider the *convex combination* between the two points ρ_1 and ρ_2 is defined as

$$\rho_i = (1 - \beta)\rho_1 + \beta\rho_2$$

Here $\beta \in [0, 1]$ is the parameter of the convex combination. We varied the parameter in the *convex path* in its domain between the two optimal solutions, and present the results in Figure **4-24**. There we see that the compliance in the convex path increases and then diminishes before reaching the second solution. We conclude that both solutions are not connected by a *gradient-descend path*. By applying a slightly smaller penalty $p = 2.95$ we observe that locally with a continuation strategy the process would most likely converge to optimum ρ_2^* and the minimum ρ_1^* seems to appear due to the $p = 3.00$ penalty. This observation coincides with conclusions in [Watada and Oshaki, 2009], where the authors proved that certain local minima appear without being connected in a continuation sense to other optima. We make the following observations about this problem:

- The frequencies for the two best local minima are $f_{1000}(\rho_1^*) = 2$ and $f_{1000}(\rho_2^*) = 9$. These values and the graph in Figure **4-24** suggest that the valley of attraction of the minimum ρ_2^* is larger. Hence, the local minimum with a larger valley of attraction was

obtained a greater number of times from random initial conditions. This points out that solutions with larger valleys of attraction will appear a greater number of times in an optimization process with random initial conditions.

- The probability of obtaining the lowest minimum ρ_2^* with random initial conditions is low. The relative frequency for the 2D cantilever experiment in this section is 9/1000 or 0.9%. This further suggests that random initiation is not a good strategy for obtaining better local minima, but it might be a good strategy to find significantly different layouts of members in the design.

- 15 of the 28 minima were found with an added relative frequency of 22/1000. This is, more than half of the minima appeared with a very low probability. We suppose there might be a greater amount of minima that appear with similar small probability starting from random initial conditions.

- Close to half of the solutions, 13/28, have a lower compliance than the continuation solution and add a relative frequency of 527/1000 or 52.7%. This is, for this problem a random start can deliver a numerically better solution than the continuation strategy.

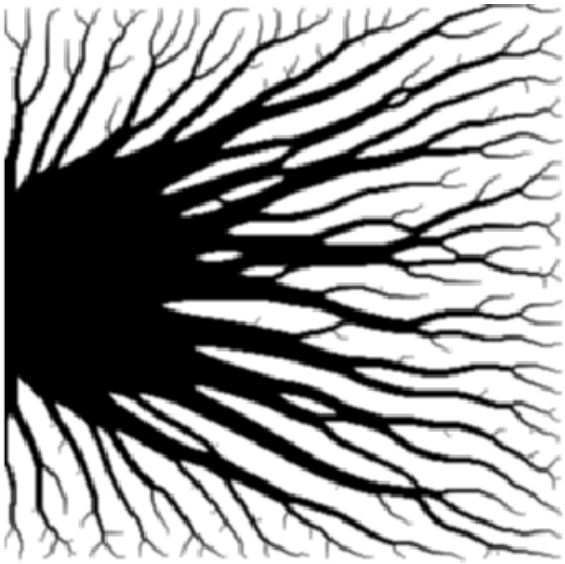

Figure 4-25: Method of densities area-to-point optimization with the same parameters in Table **4-1** and random initial conditions. Compliance $c/c_0 = 1.119$

These observations are specific to the settings of this problem and we cannot generalize them to all elasticity problems or to the heat sink problem. Nevertheless, we can use the knowledge gained in this problem to conclude that repeated random starting can be a strategy to explore the set of optimal points, but might not be a good strategy to make improvements in topology optimization problems. Provided that topology optimization problems are highly dependent

on the initial conditions, we conclude that a problem like the heat area-to-point problem, which presents organized members, should not be randomly started. We exemplify this in Figure **4-25**, where we use as the initial point a random vector generated with uniform distribution scaled to satisfy the volume fraction constraint. Non-straight branches appear in the design and some zones of enclosed void that, as we know, are suboptimal details of this problem. This last conclusion has implications in the analysis in Chapter 5.

5 Regularization techniques

In the previous chapters, we explored local minima and factors that influence the convergence to different designs. Randomly restarting the optimization or making small adjustments can significantly alter the final design, as discussed in Chapter 4. In this chapter, we aim to search for local minima in a different way—for example, by exploring a method that searches for different local minima after finding a specific one. Motivated by this proposal the tunneling method was studied from [Gómez and Levy, 1970, Barrón-Romero and Gómez, 1991]. This method modifies the objective function based on past iterations of the optimization. Additionally, we investigated the benefits of introducing a regularization term to enhance the final values of the minimized functional.

5.1 The shape of the functional

The number of design variables in topology optimization makes difficult the visualization of the functional of the problem. This issue is more pronounced in the method of densities than in the GPTO. We have seen in Chapter 4 how along the segment joining local minima there are well-defined convex directions that allow the rapid convergence of the optimization to some local minimum, but also the presence of concave directions, for example, between minima. In this section, we explore a strategy to understand the functional of the compliance problem in topology optimization and possibly establish some regularization techniques to improve solutions.

5.1.1 The functional in GPTO

During the optimization process in GPTO, it is common to see one or both endpoints of some geometric primitive *bounce* in a small region of the domain, see Figure **5-1**. This effect is due to the discretization of the density field, where the primitives are projected and can prolong the optimization more iterations than necessary to find an acceptable solution to the problem. For this reason, it is advisable to stop the optimization after a certain number of iterations. We used this fact as motivation to design an experiment that could give us some idea of the graph of the functional in GPTO.

Consider the experiment in Figure **5-2**a, similar to the area-to-point experiment in Chapter 4. In a squared domain with a 20×20 mesh, we place 3 geometric primitives of fixed ra-

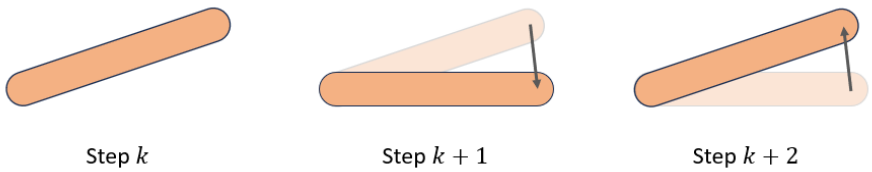

Figure 5-1: Representation of the bouncing effect of the primitives in some domain during the optimization process. In step $k+2$ the primitive endpoint returns to a point similar to the point in step k.

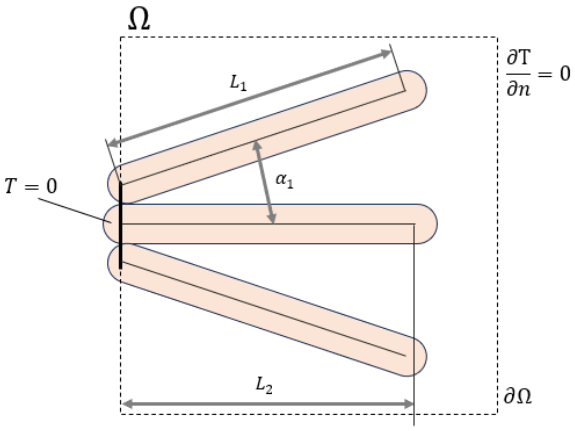

(a) Domain of the problem with 3 primitives in the GPTO method.

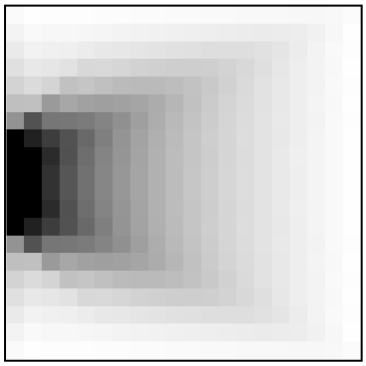

(b) Non-penalized solution in the method of densities.

Figure 5-2: GTPO experiment similar to the area-to-point presented in the previous chapter. Three bars of fixed radius 1.0 and fixed size 1.0 are placed in a domain to evacuate the heat. The disposition is kept symmetrical and the left endpoints are fixed. $V_f^* = 0.2$. The solution to the non-penalized problem for the density method is shown on the right.

dius $r_b = 1.0$ to evacuate the heat produced homogeneously in the domain, with maximum volume fraction $V_f^* = 0.2$. There is a sink of temperature $T = 0$ and adiabatic conditions in the rest of the boundary, see Figure **5-2**a. We fixed the left endpoint of the bars at points $(0, 8)$, $(0, 10)$ and $(0, 12)$ and every bar has a size $a = 1.0$, that is, they project to maximum pseudo-density in a completely covered element. The right-hand side endpoints of the primitives have also a special setting. The central bar has the y coordinate fixed at the same height of the left endpoint, but the x coordinate (or the length of the bar L_2) is free. Top and bottom bars are symmetric with respect to the central bar, and we move freely the right endpoint of the bars with the condition that $V_f = V_f^*$, that is, we satisfy the volume constraint. We parameterize the position of the endpoint of the top and bottom bars in terms of the angle between the central line of the top and central bars α_1, and adjust the

length L_1 to satisfy the volume constraint. This setup is a higher-dimensional variation of the problem presented in [Wein et al., 2020] to discuss local minima in feature-mapping methods.

The solution with the density method and without penalization is presented in Figure **5-2**b. We first notice that the local minima found with these degrees of freedom in the described problem may not correspond to local minima in the problem if every possible degree of freedom is considered as a design variable since the solutions of the problem could contain partial-size elements and we restricted the bar size in the problem to 1.0.

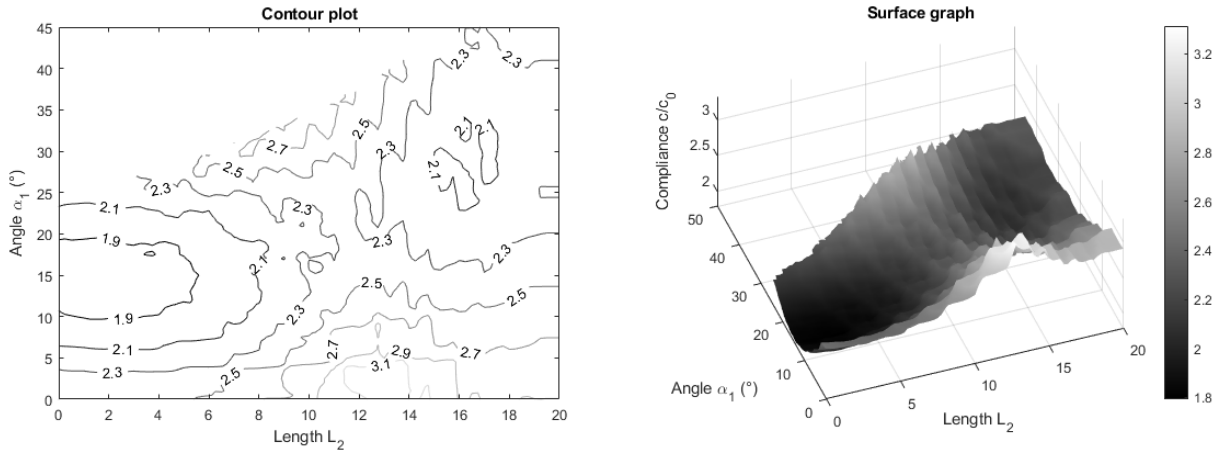

Figure 5-3: Graph and contour plot of the compliance value c/c_0 for the GPTO problem in Figure **5-2**a. We can observe that the functional has several local minima and irregular contour curves.

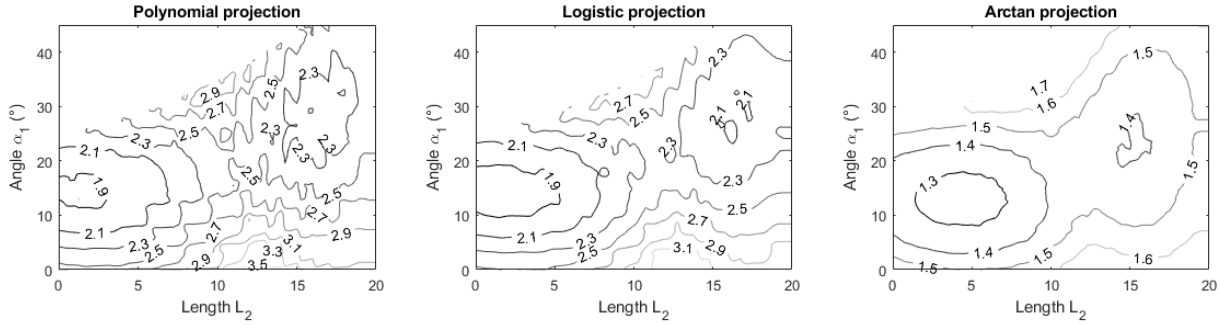

Figure 5-4: Contour plots for the compliance value c/c_0 for the alternative projection functions in problem of Figure **5-2**a.

The value of the compliance c/c_0 (with the value in the non-penalized density method solution as c_0) using the arccos projection function is presented in Figure **5-3**. In general, there are two large attraction basins, but these regions are not convex. Inside the regions,

we can see there are multiple local minima and many saddle points. We have used a small number of levels in the contour plot to visualize the functional to keep clarity, however, if we increase the levels we can see a greater number of irregularities. Alternative projection contour plots are presented in Figure **5-4**, see Subsection 3.4.3, There we can see that the polynomial mapping does not contribute to the smoothness of the functional, but presents even more pronounced irregularities. On the other hand, the non-compact support logistic and arctan functions increase the smoothness and diminish the number of local minima and saddle points. Lower values of compliance in the arctan projection are due to the fact that partial-size elements are a better solution to this problem even with RAMP interpolation.

We can see that for the GPTO method, the valleys of attraction are well defined, even though traversing them with the original arccos-based mapping can take a large number of steps before convergence. We have not considered other issues that could arise—for example, a poorly-conditioned Hessian or additional effects due to the superposition of the primitives. Nevertheless, if we consider that the form of the functional of more general problems with more dimensions resembles what we have presented here, there is great potential in methods designed to find different local minima in further steps.

5.2 Using the global optimum of the non-penalized problem

The minimum value obtained using linear interpolation in heat problems provides valuable information when searching for binary solutions. In the limit case, where the minimum length scale approaches zero, the two solutions become equivalent, [Yan et al., 2018]. We can interpret this last statement the other way around: if we look for 0-1 designs with a certain minimum scale and we observe such designs with a coarser lens, the coarse versions of the non-penalized and the penalized numerical solutions are similar. Consider for example the solutions for the area-to-point problem without penalization and with penalization with different strategies of continuation presented in Chapter 4, but now *projecting* the solutions to a Q_0 space in a 10×10 mesh, see Figure **5-5**. Recalling the discussion about continuation, we know that the slower the continuation, the better the final designs we might get, see Subsection 4.4.1. Here we can see that the slow continuation solution is the most similar solution to the non-penalized solution in the coarser mesh. We referred to this in Chapter 4, where we discussed how *locally* both designs have similar amounts of material. To give a better measure of how close the two designs are, we consider the following experiment: we select several coarser meshes than the 300×300 solutions and compute the following score

$$\frac{\|\rho^{(1)} - \rho^{(2)}\|_2}{N}\,. \tag{5-1}$$

Here N is the number of elements in the coarse representation and $\rho^{(1)}$, $\rho^{(2)}$ the projected

density vectors we want to compare. We compare then every solution to the penalized problem to the non-penalized solution in Table **5-1**.

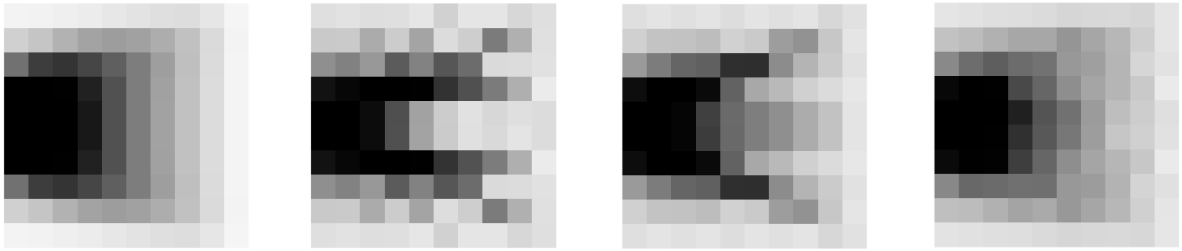

(a) No penalization. (b) No continuation. (c) Continuation. (d) Slow continuation.

Figure 5-5: $\mathcal{L}_2$-projection of the solutions to the area-to-point problem in a coarser representation of 10×10 squared elements in Q_0. Notice the similitude between projected designs for the non-penalized and the slow continuation solutions and Table **5-1** for numerical values.

Mesh size	**No continuation**	**Continuation**	**Slow Continuation**
60×60	0.3016	0.2748	0.2675
30×30	0.2569	0.2228	0.1730
20×20	0.2218	0.1890	0.1115
15×15	0.1939	0.1696	0.0983
12×12	0.1667	0.1263	0.0811
10×10	0.1622	0.1047	0.0673

Table 5-1: Comparison scores for the area-to-point projected solutions with different continuation strategies in other mesh sizes. For all the coarser meshes the projected slow continuation design has a higher similitude to the non-penalized solution.

This observation leads us to test if it is possible to improve the heat problem material distributions in an efficient way. The strategy adopted in [Yan et al., 2018] to improve solutions or the slow continuation tested in this document becomes too expensive for a general problem. The ideal modification of the method would require less iterations with little overhead. Local constraints of material were tested in [Yan et al., 2018] to try to improve the designs, but this did not produce satisfactory results in the optimization. We also tested simple constraints in the solution trying to improve the performance of the resulting design.

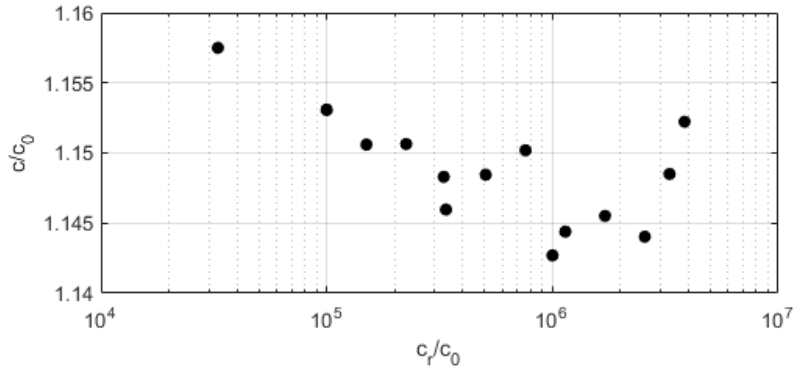

Figure 5-6: Final scaled compliance values of optimization with regularization and no continuation. Parameters equal to Table **4-1**. With a simple strategy we can see some improvement in a range of regularization values around $c_r/c_0 = 10^6$. Other variability can be attributed to the randomness of final solutions mentioned in Chapter 4.

The $\mathcal{L}_2$ explicit regularization

We also tested the idea of including in the functional the following regularization term

$$c_r \int_\Omega (\rho(k) - \rho^*_{np})^2 = c_r \frac{\|\rho^{(k)} - \rho^*_{np}\|_2^2}{N^2} \,. \tag{5-2}$$

Here $\rho^{(k)}$ is the design at step k, ρ^*_{np} the global non-penalized optimum, N the number of elements, and c_r a constant to be chosen. Notice that if the regularization term penalizes the distance to the non-penalized solution, then it favors designs with gray zones depending on the strength of the penalty parameter c_r. For this reason, it would make sense to have a c_r dependent on the iteration. It could be an abrupt change from c_r to 0 after some iterations, or it could be progressive (similar to the continuation method). We define the regularized problem in the way presented in Problem 8.

Problem 8 *Find an optimal distribution of material $\rho \in Q_0$, such that the following functional in terms of the vector of temperature (or displacement) $\boldsymbol{u}$ and the load vector $\boldsymbol{f}$ is minimized,*

$$\begin{aligned} \min_{\rho} \quad & \boldsymbol{u}^T(\rho)\boldsymbol{f} + c_r(k)\frac{\|\rho - \rho^*_{np}\|_2^2}{N^2} \,, \\ \textit{subject to} \quad & \frac{1}{N_e}\sum_{i=1}^{N_e} \rho_i \leq V_f^* \,, \\ & 0 < \rho_{min} \leq \rho_i \leq 1 \,. \end{aligned} \tag{5-3}$$

Here V_f^* is a maximum fraction of material in the domain. The regularization constant has

(a) No regularization ($c_r = 0$). (b) Regularization $c_r = c_0 \cdot 10^6$. (c) Regularization $c_r = 3.3c_0 \cdot 10^6$.

Figure 5-7: Three examples of the optimization with regularization from Figure **5-6**.

a dependence on the iteration k. Vectors $\boldsymbol{u}$ *and* $\boldsymbol{f}$ *must satisfy the additional restriction*

$$\boldsymbol{K}(\rho)\boldsymbol{u} = \sum_{e=1}^{N} E_p\left(H_e(\rho)\right)\boldsymbol{K}_{0,e}\boldsymbol{u} = \boldsymbol{f}\ . \tag{5-4}$$

The constant p is chosen in $[1, \infty)$ *and* $E_p(\rho)$ *as in* (3-13) *and* H_e *represents the filter map resulting in the final density of element e.*

We test the first approach in an experiment: we assume that an optimization with no penalization where we find the global optimum in 50 iterations has already been performed, then we have information available about a design close to the global minimum. We start a new optimization with penalization SIMP and $p = 3$, with the optimization parameters of Table **4-1** using the non-penalized design as the initial condition, no continuation and the regularization term (5-2). We use several values for the constant c_r, multiplying internally also by c_0 as a means to attain a dimensionless parameter for regularization.

The scatter plot in Figure **5-6** shows the final scaled compliance value with 0-1 forced values, as presented in Chapter 4. Around $c_r/c_0 = 1e6$, there is a set of values that suggest a positive effect of the regularization term. Examples of the obtained designs are presented in Figure **5-10**a. We see that there is a clear formation of well-organized members without detaching branches, but some of them do not align with the sink, in contrast to the optimization without the regularization term (notice that this a different experiment to **4-7**b due to the initial conditions). There are several questions we can address with this method. We start by comparing the results of different strategies of regularization with and without continuation. In Figure **5-8**, we propose four different strategies used to modify the regularization constant in the optimization, including *progressive* strategies. Strategy 3 coincides with the initial experiment of regularization in Figure **5-6**, but this time we also consider the case with continuation in the right. Results of this experiment are presented in Figure **5-9**.

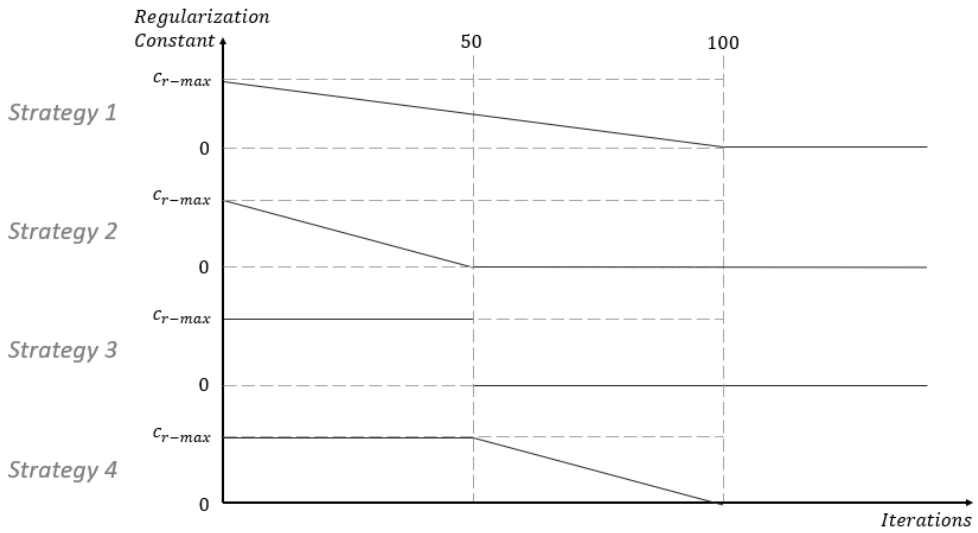

Figure 5-8: Different strategies to set the regularization constant c_r according to the iteration.

We observe that the regularization alone cannot outperform the continuation with any of the regularization strategies and constants tested. Combining the regularization with continuation can improve the final compliance value but the regularization constant shifts to a lower value (to the left in the scatter graph) than the optimal values for the no-continuation regularization, suggesting a partial antagonistic effect between them. Both continuation and regularization promote the formation of branch-less straight members in the domain and together they keep the local distribution of material close to ρ^*_{np}. However, they also compete and interfere with each other because the regularization members do not form with an orientation toward the sink of the domain but apparently with the orientation of the mesh (we ignore if there may be additional differences). With a small but significant influence of the regularization term, the optimizer favors the orientation given by the continuation strategy but avoids strong changes in material distribution thanks to the regularization term, and it eliminates detaching branches from members.
We repeat the experiment but using the following regularization strategy, intended to determine if with a longer number of iterations the combined effect also works, say,

$$c_r(x) = \max\left(0, c_{r-max}(1 - I/1000)\right). \tag{5-5}$$

Here I is the iteration and c_{r-max} is the starting value of the regularization constant. In the final designs in Figure **5-10**, we can see that the progressive change of the regularization parameter helps the members of the design acquire a better disposition without branches. The final value of compliance also improves.
We offer a hypothesis to explain why the regularization might work in our problem setting: for the studied designs, we have been using a filtered non-projected solution; that is, the

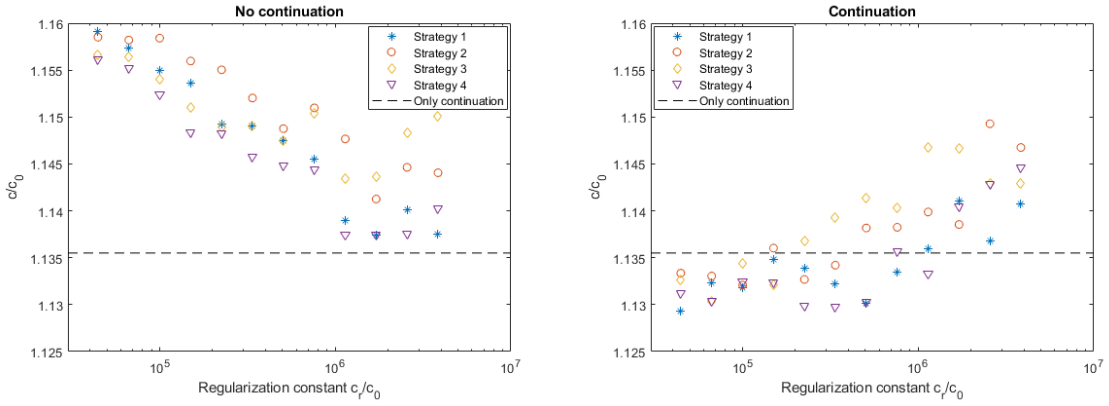

Figure 5-9: Final scaled compliance values of optimization with different regularization strategies. Strategies are compared with and without continuation. Parameters equal to Table **4-1**.

designs have gray boundaries between full and void material zones. We know additionally that a good design with only 0-1 cells could have the same distance to ρ^*_{np} that a bad design has, and then the same regularization value. With these two pieces of information, we argue that the observed improvement must occur because of the similitude between ρ^*_{np} and the blurred boundaries in a penalized optimum ρ^*. This similitude is higher if the members of ρ^* can describe a progression of material in their boundaries similar to the smooth progression seen in ρ^*_{np}. Members that do not orient in the same direction of the edges of the finite elements have more pronounced transitions of material, see for example the projection of a straight GPTO member in **3-10**d. In conclusion, the regularization favors members with a similar orientation to the edges of the elements in the mesh because they have smoother descriptions of material resembling those of a non-penalized design.

Finally, we also repeat the experiments for the regularization strategies with the DQ1 representation. As we saw in Chapter 4, with this representation the main large branches characteristic of non-continuation designs appeared even with a very slow continuation — that is, we obtained worse designs with this description than with the Q_0. By applying regularization, we can see a notorious improvement of the designs in a wide range, see Figure **5-11**. Even the regularized designs without continuation are able to outperform the continuation designs. This can be explained because the regularization forces the two thick branches to disappear in favor of more distributed members. The useful region without continuation is rather small, in comparison with the region of good results with continuation. We also observe that the shifting in improving lower maximum c_r constant values is not as pronounced as in the Q_0 case. We can see in Figure **5-12** that the best continuation regularized design accumulates more material in members than the best non-continuation design.

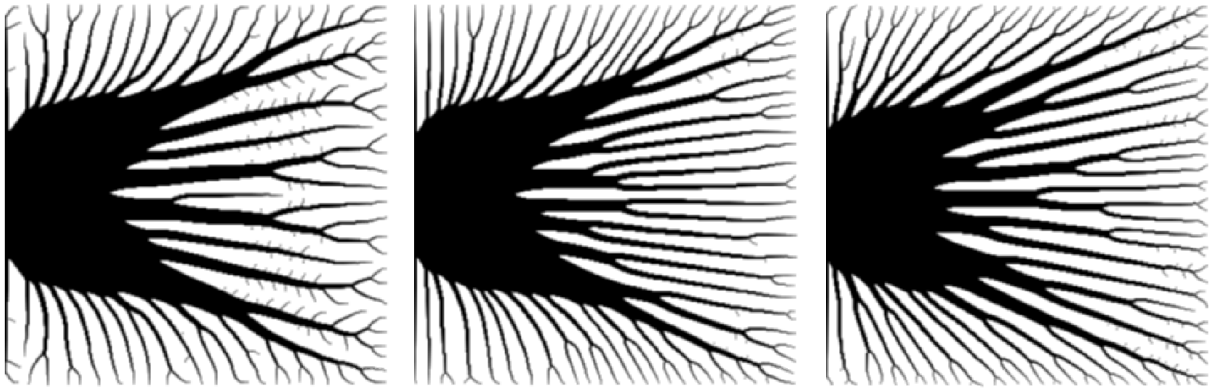

(a) No continuation. $c_{r-max} = c_0 \cdot 10^6$ $c/c_0 = 1.130$.

(b) Continuation, step $2 \cdot 10^{-3}$. $c_{r-max} = c_0 \cdot 10^6$ $c/c_0 = 1.123$

(c) Continuation, step $2 \cdot 10^{-3}$. $c_{r-max} = c_0 \cdot 10^4$ $c/c_0 = 1.109$

Figure 5-10: Optimization with regularization using the parameter in (5-5). The slow change in the regularization value helps the formation of branch-less members, compare with **5-7**b. The mixture of the slow continuation improves the final value, but it is not better than the pure slow continuation strategy.

5.3 The tunneling method

Consider the following situation: we are in a local minimum ρ_1^* that we found with some optimization parameters, and we would like to find another local minimum, probably better than the one we found initially. We could use the fact that small variations in the optimization parameters or the initial conditions can affect unpredictably the final outcome of the optimization process, or we could find a way to look for other minima from taking as starting point ρ_1^* but avoiding to fall in this minimum again. The *tunneling method* searches for new local minima in an ordered fashion, transforming the objective function based on previous iterations of the algorithm. We base the discussion in this section mainly on [Barrón-Romero and Gómez, 1991] and [Zhang and Norato, 2018].

5.3.1 Main idea of the method

We now explain the method in terms of a general x. We base this explanation on the work of [Barrón-Romero and Gómez, 1991]. Broadly speaking, the tunneling method is composed of two phases:

- **Minimization phase:** In this phase any minimization algorithm is used to find a point x_i^* satisfying the optimality conditions or some convergence criterion.
- **Tunneling phase:** The original function value is exploded around the previous local minimum using a pole or a singularity, this is called a *tunneling function* $T(x, x_i^*)$. We

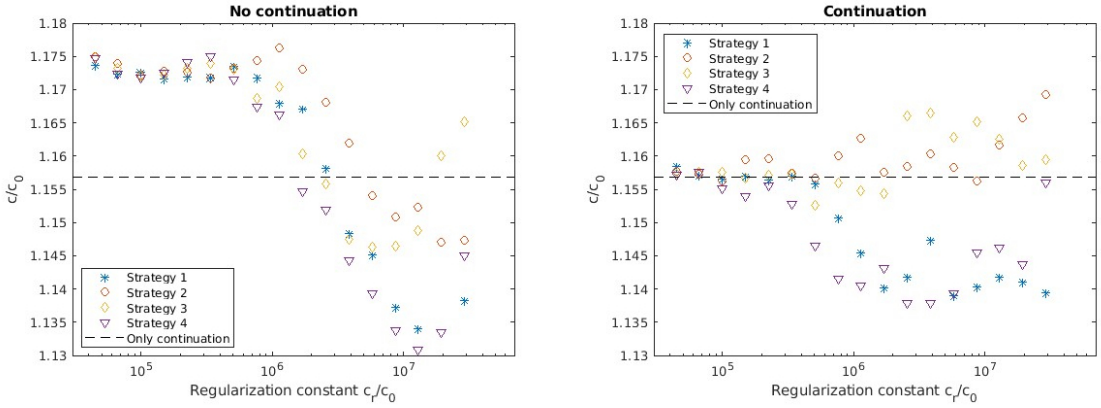

Figure 5-11: Final scaled compliance values of optimization with regularization strategies for DQ1. Parameters equal to Table **4-1**.

look for a zero of this tunneling function starting from some point x_1^0 and if we find such zero, then we start a new minimization phase from it.

The general form of the tunneling function is

$$T(x, x_i^*, \lambda) = (f(x) - f(x_i^*))\ g\left(\|x - x_i^*\|^2, \lambda\right) . \tag{5-6}$$

Here the function $g\left(\|x - x_i^*\|^2, \lambda\right)$ represents the pole or singularity, and λ adjusts the strength of the function. The core of the method lies in the tunneling phase: by using a pole or a singularity at the previous minimum (or minima) we guarantee that the search for a zero of $T(x, x_i^*, \lambda)$ will lead us far from those previous minima. This whole process depends on λ. The tunneling function $T(x, x_i^*, \lambda)$ becomes 0 if $f(x) - f(x_i^*) = 0$ and/or if $g\left(\|x - x_i^*\|^2, \lambda\right) = 0$. If we choose $g(\cdot) > 0$, then the zeros of the tunneling function are located at $f(x) = f(x_i^*)$. The original version of the method uses a pole and is called the *classical* tunneling method, see [Gómez and Levy, 1970]. Equation (5-9) becomes

$$T(x, x_i^*, \lambda) = \frac{f(x) - f(x_i^*)}{\|x - x_i^*\|^{2\lambda}} . \tag{5-7}$$

The pole of the tunneling has a flattening effect on the function f, see Figure **5-13**. From the point of view of the tunneling method, the function is now decreasing away from the pole and only reaches zero at a point with the value of the previous minimum. Parameter λ is adjusted from a small value to a greater one, depending on if the method ends trapped in a worse minimum. This method has some drawbacks, discussed in [Barrón-Romero and Gómez, 1991], and for this reason, a new variant of the method called the *exponential* tunneling method was proposed. The new tunneling function was defined as follows.

$$T(x, x_i^*) = (f(x) - f(x_i^*)) \exp\left(\frac{\lambda}{||x - x_i^*||^2}\right) . \tag{5-8}$$

(a) Continuation, step $2 \cdot 10^{-2}$. No regularization. $c/c_0 = 1.157$

(b) No continuation. $c_{r-max} = c_0 \cdot 1.30 \cdot 10^7$ $c/c_0 = 1.131$

(c) Continuation, step $2 \cdot 10^{-2}$. $c_{r-max} = c_0 \cdot 3.84 \cdot 10^6$ $c/c_0 = 1.138$

Figure 5-12: Final design examples of the best regularization results for the DQ1 representation and no-regularization with continuation result for comparison. The regularization strategy 4 improves significantly the distribution of material.

Compared to the classical tunneling method, this version has a stronger effect on the original objective function. When we use the tunneling function to find a zero of T, starting a new optimization phase from this zero we can find points at least as good as the previous minimum. The name of the method comes from the fact that while we are just looking for a zero in the tunneling function, in the original function we could be actually passing below an interval of points greater than our minimum, see [Gómez and Levy, 1970].

The method has several modifications to help it converge to other local minima. For example, in the case of a function that has several local minima at the same level, it is useful to keep track of every local minima and accumulate the effect in the following way:

$$T(x, x_i^*, \lambda) = (f(x) - f(x_i^*))\ g\left(\prod_j \|x - x_i^*\|^2, \lambda\right) . \tag{5-9}$$

Here the index j is over every previously found local minimum of the same value.

In addition, it is important to distinguish between local minima in the interior of the feasible region and local minima on the boundary. We explain each case next

- **Interior local minima**: A pole is added in the optimal point x_i^* and a new random direction is chosen to start the optimization. If the optimization is stalled, then the parameter λ is increased. There is no modification to the definition given initially.
- **Boundary local minima**: In addition to the pole in the minimum, a pole in the

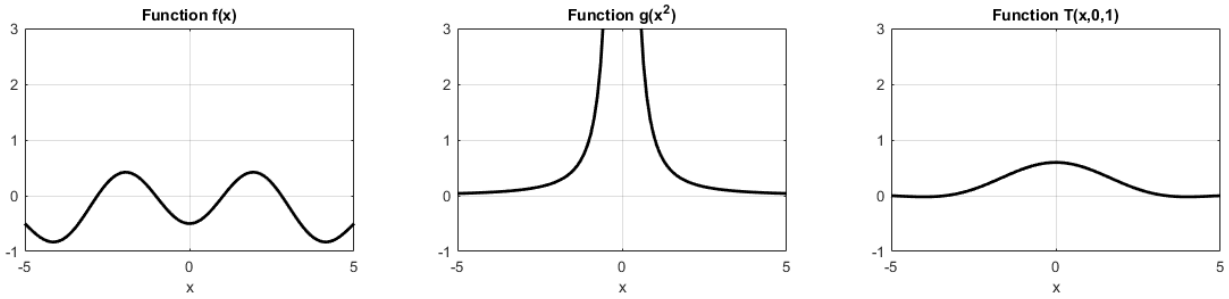

Figure 5-13: Classical tunneling method example. A function $f(x) = -0.02x^2 - 0.5\cos(\pi x)$ is multiplied by a pole $g(x^2) = 1/x^2$, to obtain the tunneling function $T(x, 0, 1)$. This tunneling function flattens the function in such a way that we might be able to find a zero of the function T close to the minimum in $x = 4$.

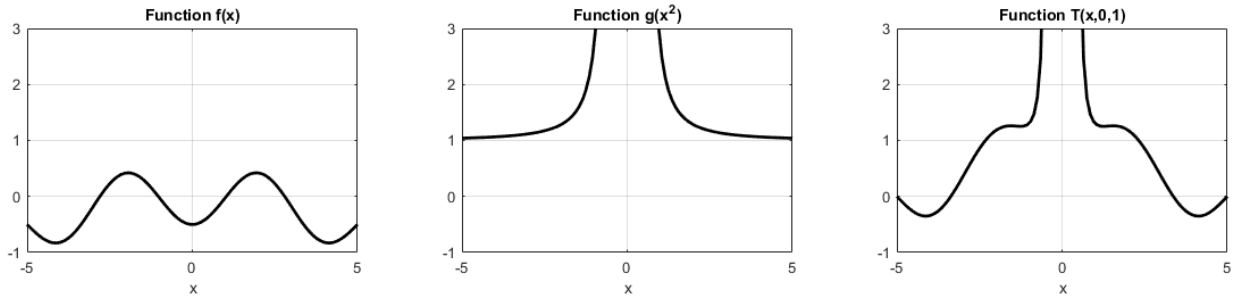

Figure 5-14: Exponential tunneling method example. A function $f(x) = -0.02x^2 - 0.5\cos(\pi x)$ is multiplied by a singularity $g(x^2) = \exp(1/x^2)$, to obtain the tunneling function $T(x, 0, 1)$. This tunneling function flattens the function in such a way that we might be able to find a zero of the function T close to the minimum in $x = 4$.

medium point between the current point x and the optimum x_i^* is added. Similarly, we can increase the strength with a factor λ_c.

For a problem such as the problem of densities, where we search for local minima always on the boundary of the domain, the second case applies. For the GPTO, given that generally, most of the points of the primitives are inside the domain, the first case should apply more frequently, however, as we know that the volume fraction constraint is active, then the boundary local minima is applied too. In any case, the tunneling method can be implemented to decide depending on the position of the local minimum.

Recent works with similar approaches can be found in [Papadopoulos et al., 2021], where authors explore multiple solutions of Navier-Stokes and elasticity TO problems with a *deflated barrier method* proposed in the same work. Also in [Tarek and Huang, 2022], where the authors use a *deflation* operator to converge to different solutions from the same initial

conditions, this operator has the form of a pole and is multiplied to the objective function. Multiple solutions can be added or multiplied to always guarantee different solutions. The methods present important similitude and the results in that work and [Zhang and Norato, 2018] are comparable.

5.3.2 The tunneling function of the compliance functional

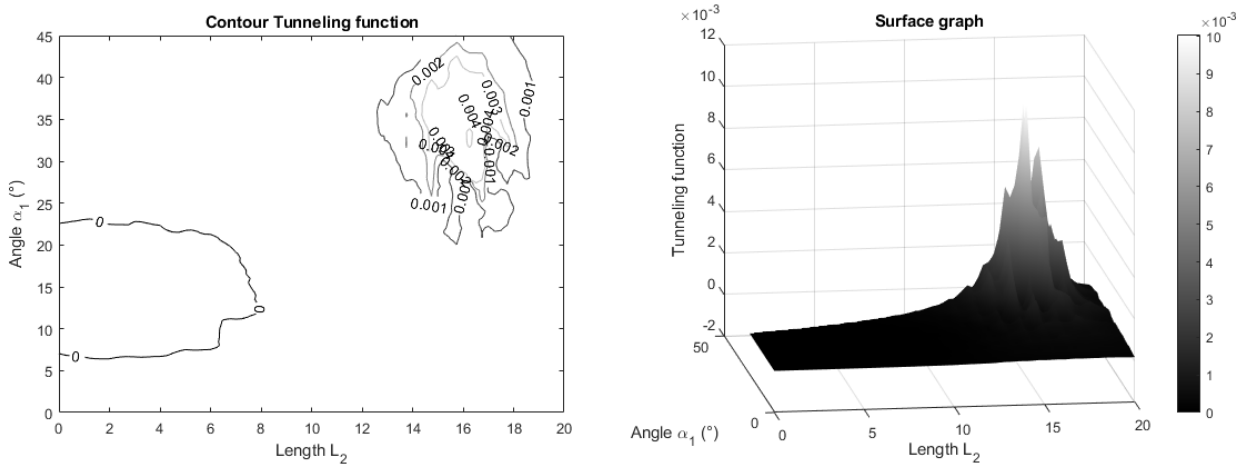

Figure 5-15: Classical tunneling function of the functional in Figure **5-3**. The pole is applied to the sub-optimal local minimum $(17.2, 32)$. The functional flattens with the pole but presents a lot of irregularities. The second valley marked by the 0 contour will stop the zero-finding algorithm and start a new minimization phase.

Consider the example of Section 5.1, where we restricted a GPTO heat problem with three bars to three design variables and a volume restriction to visualize the functional in Figure **5-3**. We can multiply the following pole to obtain a tunneling function

$$g\left(\|\rho_1^* - \rho\|^2, 2\right) = \frac{1}{\|\rho_1^* - \rho\|^4} \tag{5-10}$$

We choose the minimum at $(17.3, 32)$ to start the tunneling phase, being this minimum considerably higher than the minimum in $(3.0, 12)$. The resulting tunneling functions are presented in Figure **5-15**. There we can see that the tunneling function facilitates the descend from the previous minimum. We can also note that there is a loss of precision in the tunneling function (this could hinder the work of the zero-finding algorithm due to limited numerical precision) and that not every local minimum has disappeared. The last problem can be solved by increasing the strength of the pole, but this could cause also more loss of numerical precision in the search.

5.3.3 Elasticity problem

Figure 5-16: Tunneling method applied to the Michell bridge. The point ρ_1^* is found after the first optimization, and a tunneling phase is applied. Depending on the parameters of this phase, we can find other minima close or far from the initial point.

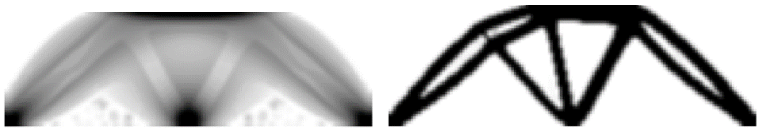

(a) First steps of the tunneling. (b) Design found.

Figure 5-17: If the strength of the pole or singularity is too large, then the density cells of the previous design are avoided and the search converges to a sub-optimal design with empty zones in the members. This can make the tunneling search fail and it must be restarted.

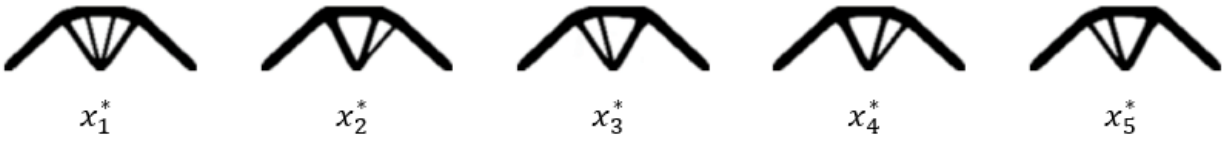

Figure 5-18: After the first tunneling phase the method gets trapped between two solutions.

We apply the tunneling method to the Michell bridge problem, see Figure **5-16**. The point ρ_1^* is the point we found after the first optimization phase, and the possible points ρ_2^* the optima found after a tunneling and a second minimization phase, depending on the strength of the pole we place and the perturbation we apply to start the tunneling phase. A small λ keeps the method close to the design ρ_1^*, in this case, a small detail in the left-central member. The second and third possible designs represent cases where the pole generates a bigger repulsion. For a symmetrical problem like this one, a random perturbation, as suggested in [Barrón-Romero and Gómez, 1991], can deliver random members with unusual designs due to the attracting effect that cells with higher densities present, as discussed in Chapter

4. Notice also that asymmetrical designs with strong attraction valleys can be sub-optimal and trap the tunneling phase in a region without zeros, forcing the tunneling to restart from another point. A pathological case occurs when the repulsion is too strong, that is, the force of the pole or singularity drives the optimization away to the optimization and the initial phases of the optimization repel most of the elements of the previous optimization, see Figure**5-17**a. If eventually, the optimizer is able to find a path close to the local minima this effect of the initial phases can be avoided. However, it can also happen that the optimizer cannot find a path that eliminates this repulsion of the elements and the appearance remains as shown in Figure **5-17**b.

Adequate selection of the parameter λ is critical for the good performance of the method, however, function evaluations are expensive. If the method starts with a small λ and increases it when it fails to find a minimum, due to the great number of attraction valleys the method can end up evaluating the function as many times as other methods, like a very slow continuation. We can modify the method by choosing a different starting point for the tunneling function; for example, instead of adding a perturbation, we can always select a uniform starting point, this way all elements start with a similar preference and we avoid random members. This modification can give good results in the following phase of the optimization, but it can also suffer a new problem as shown in Figure **5-18**. Here we can see how the solutions iterate between a few solutions. Minima like ρ_2^* and ρ_4^* or ρ_3^* and ρ_5^* are not exactly the same and we can obtain in a number of iterations each time a slightly smaller value, as the algorithm runs longer looking for the solution. However, we do not obtain diversity in the new solutions to the problem. We could then add a pole for each previous solution and don't take it away every time a solution is found even if they have considerably different compliance. Adding several poles—one for any local minimum found—can be initially a sound choice, as it will always guarantee to obtain a different design each time. But it also widens the repulsion zone until eventually the algorithm no longer converges, leaving us always with designs like **5-17**a. Remarks in [Tarek and Huang, 2022] mention similar convergence problems: if the algorithm is able to find a new optimal point, it will be different from the previous one. However, as we saw in the tunneling method, convergence is not guaranteed.

6 Conclusions and final remarks

In this study, we have explored topology optimization techniques, which, while established, still offer numerous opportunities for improvement. Our investigation has studied how the representation of the material distribution directly impacts final results, and how slight modifications to initial conditions can significantly alter the distribution of material, see Section 4.3. We have observed that methods introducing gradual changes to the objective function can lead to improvements at the cost of increased computational time or altering the appearance of final designs, see Section 4.4. Additionally, we have discovered that local minima can pose a significant challenge. Despite this, there may be opportunities to overcome this challenge provided by the shared characteristics between optimal 0-1 solutions and the global minima of linear-interpolation solutions. However, further research is needed to understand why alternative representation schemes often yield different (and worse) results than the traditional Q_0 representation, see Section 4.5.

One crucial aspect we focused on was the implementation of the geometry projection method in the heat problem. While our exploration revealed promising results, it is evident that further study and refinement are necessary to achieve optimal solutions for general-type problems, see Section 4.4. The superposition of primitives emerged as a notable challenge, and we hypothesize that this superposition may underlie certain phenomena observed during the optimization process. Throughout our investigation, we also experimented with various alternative projection functions. These functions significantly influenced the shape of the functional and, in turn, the convergence of the optimizer towards a solution. The question remains whether progressive changes in the function to map primitives could lead to further enhancements in final designs. Understanding the interplay between different projection functions and their effects on the optimization will be crucial for developing efficient and effective approaches, see Section 5.1.

A finding in our study was the divergent performance of alternative representation schemes compared to the traditional Q_0 representation. Understanding the reasons behind this discrepancy can be crucial for guiding future improvements in topology optimization methodologies, see Section 4.3. Identifying the strengths and weaknesses of different representation schemes will aid researchers in developing more robust and effective approaches. Our study has shed light on the potential of regularization methods to improve design outcomes, see Section 5.2. However, the exact mechanisms through which this occurs require further

elucidation. We recognize the need to clarify the underlying hypotheses that guided our regularization experiments. The use of the tunneling function in the classical density method yielded various outcomes, indicating a great potential for methods with geometric representations, such as the GPTO, see Section 5.3.

In summary, our study has demonstrated that topology optimization remains a vibrant field with ample room for advancement. Through the refinement of geometry projection, investigation of alternative projection functions, and a deeper understanding of regularization mechanisms, we can pave the way for more effective and efficient topology optimization approaches. By addressing the challenges posed by the superposition of primitives and exploring representation schemes, we may unlock the full potential of topology optimization in solving complex engineering design problems. With continued research and collaborative efforts, we are optimistic about the future prospects of this fascinating field.

Bibliography

[Andreassen et al., 2010] Andreassen, E., Clausen, A., Schevenels, M., Lazarov, B. S., and Sigmund, O. (2010). Efficient topology optimization in matlab using 88 lines of code. *Structural and Multidisciplinary Optimization*, 43:1–16.

[Barrón-Romero and Gómez, 1991] Barrón-Romero, C. and Gómez, S. (1991). The exponential tunneling method. *Reporte de Investigación IIMAS*, 1:1–23.

[Beghini et al., 2014] Beghini, L. L., Beghini, A., Katz, N., Baker, W. F., and Paulino, G. H. (2014). Connecting architecture and engineering through structural topology optimization. *Engineering Structures*, 59:716–726.

[Bell et al., 2012] Bell, B., Norato, J., and Tortorelli, D. (2012). *A Geometry Projection Method for Continuum-Based Topology Optimization of Structures*.

[Bendsøe and Sigmund, 1999] Bendsøe, M. and Sigmund, O. (1999). Material interpolation schemes in topology optimization. *Archive of Applied Mechanics*, 69:635–654.

[Bendsøe and Sigmund, 2004] Bendsøe, M. and Sigmund, O. (2004). *Topology Optimization*, chapter 1, pages 1–68. Springer, first edition.

[Cavazzuti et al., 2011] Cavazzuti, M., Baldini, A., Bertocchi, E., Costi, D., Torricelli, E., and Moruzzi, P. (2011). High performance automotive chassis design: A topology optimization based approach. *Structural and Multidisciplinary Optimization*, 44:45–56.

[Deaton and Grandhi, 2014] Deaton, J. D. and Grandhi, R. V. (2014). A survey of structural and multidisciplinary continuum topology optimization: post 2000. *Structural and Multidisciplinary Optimization*, 49:1615–1488.

[Donofrio, 2016] Donofrio, M. (2016). Topology optimization and advanced manufacturing as a means for the design of sustainable building components. *Procedia Engineering*, 145:638–645.

[Gelfand and Fomin, 2012] Gelfand, I. and Fomin, S. (2012). *Calculus of Variations*. Dover Books on Mathematics. Dover Publications.

[Gockenbach, 2006] Gockenbach, M. (2006). *Understanding and Implementing the Finite Element Method*. Other Titles in Applied Mathematics. Society for Industrial and Applied Mathematics (SIAM, 3600 Market Street, Floor 6, Philadelphia, PA 19104).

[Gómez and Levy, 1970] Gómez, S. and Levy, A. (1970). *The tunnelling method for solving the constrained global optimization problem with several non-connected feasible regions*, volume 909, pages 34–47.

[Johnson, 2012] Johnson, C. (2012). *Numerical Solution of Partial Differential Equations by the Finite Element Method*. Dover Books on Mathematics Series. Dover Publications, Incorporated.

[Kreyszig, 2007] Kreyszig, E. (2007). *Introductory Functional Analysis with Applications*. Wiley classics library. Wiley India Pvt. Limited.

[Marheineke, 2020] Marheineke, N. (2020). Lecture notes: Numerics for differential equations. Trier University.

[Matsimbi et al., 2021] Matsimbi, M., Nziu, P., Masu, L. M., and Maringa, M. (2021). Topology optimization of automotive body structures: A review.

[Norato et al., 2015] Norato, J., Bell, B., and Tortorelli, D. (2015). A geometry projection method for continuum-based topology optimization with discrete elements. *Computer Methods in Applied Mechanics and Engineering*, 293:306–327.

[Orme et al., 2017] Orme, M., Gschweitl, M., Ferrari, M., Madera, I., and Mouriaux, F. (2017). Designing for additive manufacturing: Lightweighting through topology optimization enables lunar spacecraft. *Journal of Mechanical Design*, 139.

[Ortegón-Villacorte, 2021] Ortegón-Villacorte, A. (2021). Pygpto.

[Ortegón-Villacorte, 2023] Ortegón-Villacorte, A. (2023). Topopt experiments.

[Papadopoulos et al., 2021] Papadopoulos, I. P. A., Farrell, P. E., and Surowiec, T. M. (2021). Computing multiple solutions of topology optimization problems. *SIAM Journal on Scientific Computing*, 43(3):A1555–A1582.

[Paulino and Le, 2009] Paulino, G. H. and Le, C. H. (2009). A modified q4/q4 element for topology optimization. *Structural and Multidisciplinary Optimization*, 37:255–264.

[Rahmatalla and Swan, 2004] Rahmatalla, S. and Swan, C. (2004). A q4/q4 continuum structural optimization implementation. *Structural and Multidisciplinary Optimization*, 27:130–135.

[Rozvany, 2009] Rozvany, G. (2009). Rozvany, g.i.n.: A critical review of established methods of structural topology optimization. structural and multidisciplinary optimization 37, 217-237. *Structural and Multidisciplinary Optimization*, 37:217–237.

[Rozvany, 1998] Rozvany, G. I. N. (1998). Exact analytical solutions for some popular benchmark problems in topology optimization. *Structural optimization*, 15(1):42–48.

[Sigmund, 2022] Sigmund, O. (2022). On benchmarking and good scientific practise in topology optimization. *Structural and Multidisciplinary Optimization*, 65.

[Sigmund and Maute, 2013] Sigmund, O. and Maute, K. (2013). Topology optimization approaches. *Structural and Multidisciplinary Optimization*, 48:1031 –1055.

[Sigmund and Petersson, 1998] Sigmund, O. and Petersson, J. (1998). Numerical instabilities in topology optimization: A survey on procedures dealing with checkerboards, mesh-dependencies and local minima. *Structural Optimization*, 16:68–75.

[Smith and Norato, 2020] Smith, H. and Norato, J. (2020). A matlab code for topology optimization using the geometry projection method. *Structural and Multidisciplinary Optimization*, pages 1162 –1166.

[Smith and Norato, 2022] Smith, H. and Norato, J. (2022). Topology optimization of structures made of fiber-reinforced plates. *Structural and Multidisciplinary Optimization*, 65:58.

[Stolpe and Svanberg, 2001] Stolpe, M. and Svanberg, K. (2001). On the trajectories of penalization methods for topology optimization. *Structural and Multidisciplinary Optimization*, 21:128–139.

[Svanberg, 1987] Svanberg, K. (1987). The method of moving asymptotes—a new method for structural optimization. *International Journal for Numerical Methods in Engineering*, 24(2):359–373.

[Svanberg, 1998] Svanberg, K. (1998). The method of moving asymptotes - modelling aspects and solution scheme.

[Tarek and Huang, 2022] Tarek, M. and Huang, Y. (2022). Simplifying deflation for non-convex optimization with applications in bayesian inference and topology optimization.

[van Dijk et al., 2010] van Dijk, N. P., Langelaar, M., and van Keulen, F. (2010). Critical study of design parameterization in topology optimization ; the influence of design parameterization on local minima.

[Watada and Oshaki, 2009] Watada, R. and Oshaki, M. (2009). Continuation approach for investigation of the non-uniqueness of optimal topology for minimum compliance. *8th World Congress of Structural and Multidisciplinary Optimization*.

[Wein et al., 2020] Wein, F., Dunning, P. D., and Norato, J. A. (2020). A review on feature-mapping methods for structural optimization. *Structural and Multidisciplinary Optimization*, 62:1597–1638.

[Wein and Stingl, 2018] Wein, F. and Stingl, M. (2018). A combined parametric shape optimization and ersatz material approach. *Structural and Multidisciplinary Optimization*, 57.

[Yan et al., 2018] Yan, S., Wang, F., and Sigmund, O. (2018). On the non-optimality of tree structures for heat conduction. *International Journal of Heat and Mass Transfer*, 122:660–680.

[Zhang and Norato, 2018] Zhang, S. and Norato, J. (2018). Finding better local optima in topology optimization via tunneling. page V02BT03A014.

[Zhu et al., 2016] Zhu, J.-H., Zhang, W.-H., and Xia, L. (2016). Topology optimization in aircraft and aerospace structures design. *Archives of Computational Methods in Engineering*, 23:595–622.